Uniwersytet im. Adama Mickiewicza w Poznaniu

Nieliniowe Efekty Magnetotransportowe w Izolatorach Topologicznych

[Nonlinear Magnetotransport Phenomena in Topological Insulators]

Kateryna Boboshko

Rozprawa doktorska

Promotor: prof. UAM dr hab. Anna Dyrdał

Zakład Fizyki Mezoskopowej
Instytut Spintroniki i Informacji Kwantowej
Wydział Fizyki i Astronomii
Uniwersytet im. Adama Mickiewicza w Poznaniu

Poznań 2024

Streszczenie

Niniejsza rozprawa opisuje obecnie kluczowe dla spintroniki zjawiska transportowe, koncentrując się na biliniowym magnetooporze i planarnym efekcie Halla w izolatorach topologicznych. Na początku rozprawy wprowadzono podstawowe koncepcje dotyczące izolatorów topologicznych, w tym charakter ich stanów powierzchniowych, efekt przyszpilenia spin-pęd (ang. *'spin-momentum locking'*) oraz efekt Rashby, który jest związany z spinowo-zależnym rozszczepieniem pasm, w wyniku złamania symetrii inwersji przestrzennej. Następnie opisana została indukowana prądem polaryzacja spinowa, znana również jako efekt Edelsteina, oraz indukowane sprzężeniem spin-orbita efekty Halla.

W kolejnych rozdziałach wprowadzono magnetoopór i planarny efekt Halla. Rozdział 3 omawia różne typy magnetooporu i wprowadza do tematyki biliniowego magnetooporu, a więc efektu w którym magnetoopór skaluje się liniowo z polem magnetycznym i z gęstością prądu elektrycznego. W rozdziale 4 omówiony jest planarny efekt Halla, który obserwujemy w obecności pola magnetycznego zorientowanego w płaszczyźnie układu, w przeciwieństwie do zwykłego efektu Halla, w którym napięcie poprzeczne jest generowane w obecności pola magnetycznego zorientowanego prostopadle do powierzchni układu. Omówione zostały pochodzenie i mechanizmy tego zjawiska. W rozprawie omówiono także kluczowe wyniki eksperymentalne oraz przedstawiono szczegółową teoretyczną analizę nieliniowego planarnego efektu Halla, wskazując jak ten efekt można wykorzystać w przyszłych aplikacjach spintronicznych.

Następnie, stosując zaawansowane techniki teoretyczne, takie jak metoda funkcji Greena i diagramowy rachunek zaburzeń, wyjaśniono podstawowy fizyczny mechanizm biliniowego magnetooporu i nieliniowego planarnego efektu Halla dla stanów powierzchnionych w trójwymiarowych izolatorach topologicznych. Rozprawa opiera się na sformułowaniu opisu teoretycznego prowadzącego zarówno do biliniowego magnetooporu jak i nieliniowego planarnego efektu Halla w przypadku, gdy w układzie znajdują się domieszki, defekty, które z natury zawierają sprzężenie spin-orbita. Zbadano zależność tych zjawisk od parametrów charakteryzujących materiał. W ramach tej teorii wyprowadzone zostały analityczne formuły dla przewodności podłużnej i poprzecznej, współczynniki magnetooporowe (biliniowy i kwadratowy magnetoopór) oraz symetryczny i antysymetryczny kąt w planarnym efekcie Halla. Otrzymane wyniki anality-

czne i numeryczne biliniowego magnetooporu i nieliniowego planarnego efektu Halla wskazują na możliwość wyznaczenia z danych pomiarowych pewnych parametrów charakteryzujących badany układ, takich jak wektor Fermiego (energia Fermiego) i parametr sprzężenia spin-orbita.

Abstract

This thesis is focused on transport phenomena that are currently important for spintronics. It focuses on the bilinear magnetoresistance and nonlinear planar Hall effect in topological insulators. In the beginning, the fundamental concepts of topological insulators are introduced, including their unique properties like surface states, spin-momentum locking, spin-orbit coupling, and the Rashba effect that refers to the spin splitting of electronic bands due to structural inversion asymmetry. Next, the current-induced spin polarization (also known as the Edelstein effect) and spin-orbit-driven Hall effects are introduced.

The magnetoresistance and planar Hall effect are discussed in the next two chapters. Chapter 3 describes the general theory of magnetoresistance and reviews various types of magnetoresistance. Here, the bilinear magnetoresistance, i.e., the magnetoresistance effect that scales linearly with both external magnetic field and charge current density, is introduced. Chapter 4 discusses the planar Hall effect arising due to an in-plane magnetic field, unlike the ordinary Hall effect that arises in the presence of a magnetic field perpendicular to the plane of the system. The origins and mechanisms of this phenomenon, as well as key experimental findings, are provided. Chapter 4 also presents a detailed theoretical analysis of the nonlinear planar Hall effect, providing some insights into how this effect can be applied to future spintronic devices.

Then, by employing advanced theoretical techniques based on Green's functions and diagrammatic perturbation theory, the bilinear magnetoresistance and nonlinear planar Hall effect in the surface states of three-dimensional topological insulators are described. The thesis also describes a new mechanism that leads to these phenomena and is related to scattering on spin-orbital impurities. The derivation of analytical results for magnetoresistance and planar Hall effect allows for a deeper understanding of these phenomena and their dependence on material parameters. The analytical and numerical results obtained for the bilinear magnetoresistance and nonlinear planar Hall effect indicate the possibility of determining material constants, such as the Fermi wave vector and spin-orbit coupling parameter, by simple magnetotransport measurements.

Acknowledgments

I want to express my sincere thanks to my PhD supervisor, prof. UAM dr hab. Anna Dyrdał, for her support, motivation and advices during my PhD journey. Having the opportunity to work under her mentorship has been an extraordinary experience, that helped me navigate the challenges of this research.

I also appreciate the possibility to work with my colleagues from the Faculty of Physics and Astronomy, and particularly the members of the Department of Mesoscopic Physics. Their collaboration and thoughtful discussions have expanded both my understanding of physics and my overall view of life.

I would like to express my profound gratitude to my Mom. Her unconditional love and unwavering belief in me have been my foundation throughout this entire process. Without her support and understanding, this achievement would not have been possible.

Last but not least, I wanna thank me, for believing in me, for doing all this hard work, for just being me at all this time.

And now, my time has come, you must continue your journey without me...

This work has been supported by the National Science Centre in Poland (NCN) under the project Sonata-14 No. 2018/31/D/ST3/02351.

Contents

Chapter 1

Introduction

In recent years, spintronics has become one of the most promising areas of condensed matter physics, representing a transformational shift in how information is processed, stored, and transmitted in electronic devices. Spintronics goes beyond the traditional reliance on an electron's charge by incorporating its own angular momentum – spin [1]. This new approach opens up a new dimension of possibilities for improving the functionality, efficiency and power consumption of electronic devices. Spintronics is ready to revolutionize areas such as data storage, memory technology, and quantum computing, offering new opportunities for the development of devices with higher speed, greater storage capacity, and reduced power consumption.

One of the most significant class of materials in future spintronics seem to be topological insulators. Topological insulators are unique materials because they behave as insulators in their bulk, but support conductive surface states that are protected by topological invariants. Surface states in topological insulators exhibit a unique phenomenon called spin-momentum locking. This means that the direction of an electron's spin is closely connected with its momentum [2–4]. These feature makes these materials very attractive for spintronic applications, as they provide reliable and stable channels for spin transport, even if impurities or defects are present. While early researches have mainly investigated two-dimensional topological insulators, recent breakthroughs have shifted attention to three-dimensional topological insulators, revealing even more promising applications. In these three-dimensional materials, surface states display a Dirac-like energy spectrum. This allows for precise control of spin currents, paving the way for advanced spintronic devices with outstanding capabilities.

This thesis delves into magnetoresistance, a phenomenon when the electrical resistance of a material changes when exposed to a magnetic field. Magnetoresistance is fundamental to advanced technologies such as magnetic sensors, memory storage and spintronic devices. There are different types of magnetoresistance, each driven by unique mechanisms and suitable for specific applications. A particular focus of this research is bilinear magnetoresistance – a new and intriguing effect found in materials with strong spin-orbit coupling, such as topological insulators [5–8]. Bilinear magnetoresistance is described by a second-order nonlinear response to the applied electric and magnetic fields. This behavior gives new understanding of the interactions between spin and charge, offering exciting opportunities for spintronics, which can enable more efficient control of spin currents and drive innovations in next-generation spin technologies.

Another key phenomenon explored in this thesis is the planar Hall effect. Unlike the ordinary Hall effect, which generates a transverse voltage when a magnetic filed is applied perpendicular to a material, the planar Hall effect occurs when the magnetic filed is in the plane of the material. The planar Hall effect is especially intriguing in systems with strong spin-orbit coupling, such as topological insulators, making it a center of research interest due to its unique and remarkable characteristics [9–11]. Understanding the mechanisms behind this phenomenon could have profound implications for future spintronic technologies, where control over both linear and nonlinear transport properties could enhance device performance and functionality.

The main purpose of this PhD thesis is to conduct a detailed theoretical research of bilinear magnetoresistance and nonlinear planar Hall effect in three-dimensional topological insulators. At the beginning, the basic effects that can be associated with the manifestation of bilinear magnetoresistance and nonlinear planar Hall effect were studied. Next, the origin and mechanisms of recently discovered effects, namely various magnetoresistance effects and Hall effects were introduced. Attention was also paid to the investigation of the nature and properties of topological insulators. The main aim of the thesis was understanding the origin and microscopic mechanisms that are involved in bilinear magnetoresistance and planar Hall effect in topological insulators revealing isotropic Fermi contours. As a result, using Green's function formalism and diagrammatic methods, analytical expressions were obtained. This theoretical work aims to lay the foundation for future experimental research and applications in spintronics, helping to move the field forward into new territory.

Chapter 2

Theoretical Outline

This chapter examines the fundamental principles underlying topological insulators (TIs) and their unique properties. The detailed discussion provides understanding of the formation of topologically protected surface states in TIs and appearing of the spin-momentum locking in them. In addition, here is explored the effect of the spin-orbit coupling (SOC), delving into the origins and key mechanisms of the Rashba effect, a specific type of SOC, and its role in TIs.

Also, in this chapter, we will consider the origins and mechanisms underlying phenomena that arise from the interaction between the charge, spin and their transport properties. Among these phenomena, the most prominent are current-induced spin polarization (CISP), also called the Edelstein effect (EE), and the various Hall effects induced by SOC. By studying the interactions between spin, charge transport and SOC, we shed the light on their potential applications in the advancement of spintronic technologies.

2.1 Topological Insulators

Topological insulators (TIs) are a fascinating class of materials that have revolutionized the field of condensed matter physics and hold great promise for future technological applications. The state of the TI was theoretically predicted in 2005 by Kane and Mele in graphene [3, 12] and two-dimensional (2D) semiconductor system with a uniform strain [3, 13]. In three-dimensional (3D) systems, it was discovered by few groups independently in 2006 [3, 14, 15]. The first experimental confirmation came in 2007 when these states were observed in HgCdTe quantum well structures. [16] Also, then, was proposed the term "topological insulator" to describe this electronic phase [15].

A typical normal insulator consists of the two bands. A valence band is fully packed with electrons, while a conduction band remains completely empty. These two bands are divided by a band gap. In this insulator, the conduction of electrons becomes possible only through the surface states, as illustrated in Fig. 2.1(a). On the other hand, TI, also falling under the category of insulators, shares the feature of electron conduction being limited to its surface states, acting

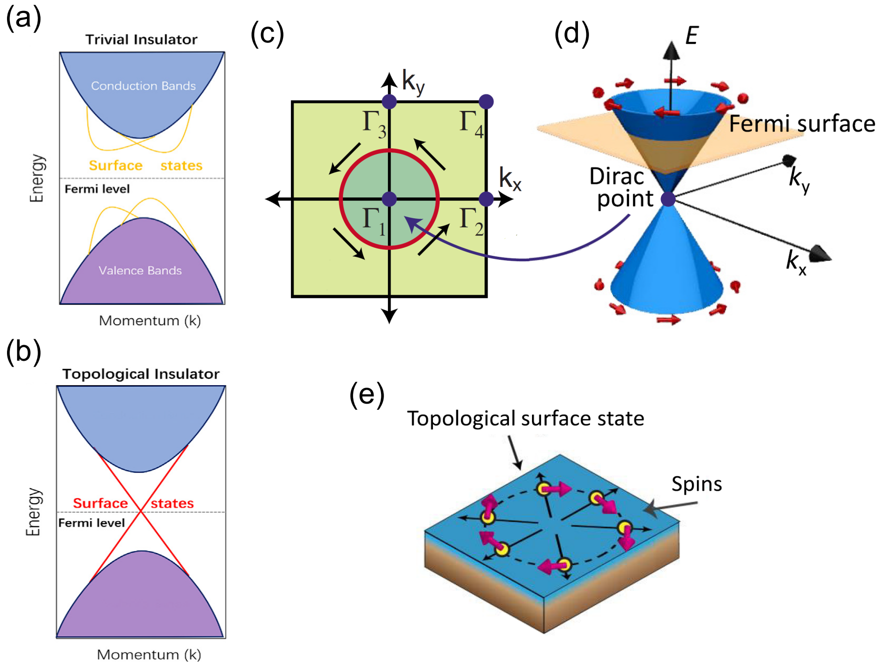

Figure 2.1: (a) Schematic of a trivial (normal) insulator [2]. (b) Schematic of a topological insulator (TI) [2]. (c) Fermi circle in the surface Brillouin zone for a strong TI [3]. (d) A Dirac cone of the TSS with the one Dirac point, Fermi level and spin-momentum locking in momentum space [17]. (e) Electrons spins on the surface of a TI in real space are polarized and orthogonal to the charge currents flow on the TSS [17].

like a normal insulator. Despite these similarities, a crucial distinction arises in a fact, that the conductive surface or edge states in a TI are topologically protected by time-reversal symmetry (TRS) [4], leading to the emergence of distinct surface bands that link the bulk conduction and valence bands, as depicted in Fig. 2.1(b). These unique connections ensure that the surface states of the TI remain conductive all the time, consistently crossing the Fermi level. In contrast, within a normal insulator, conductive surface states can often be eliminated by adequate surface modifications, thereby suppressing the conductivity of electrons in such materials [2, 4]. Such TIs are known as 2D TIs or a quantum spin Hall insulator. Their edge states are robust against magnetic and disorder perturbations, a property that results from the nontrivial topological order of the material and is often described using the Chern number, also called the TKNN (Thouless, Kohmoto, Nightingale, and den Nijs) invariant, and the Z_2 topological invariant [3, 4, 18].

Later was shown, that it is possible to extend such classification of materials to 3D systems. 3D TIs are characterized by four Z_2 topological invariants. These materials, for example as Bi_2Te_3, Bi_2Se_3, and Sb_2Te_3, can be predicted and identified by angle resolved photoemission spectroscopy (ARPES) experiments [19]. Topological surface states (TSSs) of 3D TIs due to

TRS protection are characterized by perpendicular locking of the electron's spin to its momentum, known as spin-momentum locking. While these states are present in the surface Brillouin zone and degenerated, TRS invariant creates four points $\Gamma_{1,2,3,4}$, as shown in Fig. 2.1(c). Far from these points, the spin-orbit interaction will lift degeneracy. Then these TRS invariant points make a 2D Dirac point in the surface band structure, as presented in Fig. 2.1(d), which can be described by the Dirac Hamiltonian [3, 4, 20]

$$H_{\mathbf{k}} = v_{\mathrm{F}} \left(\hat{\mathbf{z}} \times \boldsymbol{\sigma}\right) \cdot \mathbf{k}, \tag{2.1}$$

where v_{F} denotes the Fermi velocity, $\hat{\mathbf{z}}$ is a unit vector perpendicular to the TI and $\mathbf{k}$ is an electron momentum. This Hamiltonian shows a strong correlation between the electron momentum and the spin polarization directions on the TSSs, which is illustrated in Fig. 2.1(d). Furthermore, as shown in Fig. 2.1(e), because of the topological protection, in a real space all electron spins become completely polarized in a direction orthogonal to the electron's motion while charge currents flow on the TSSs. In other words, spin-polarized currents appear in the material [3,4,17].

The unique properties of TIs, arising from topological invariants, offer exciting possibilities for both fundamental research and practical applications. The spin-momentum locking and robustness of TSSs make TIs ideal for spintronic devices, quantum computing, etc. Due to their ability to support spin-polarized currents and respond to magnetic fields, TIs can be used for development of highly sensitive magnetic sensors and low-power electronic components [3, 18, 20].

2.2 Spin-Orbit Coupling in Solids

Spin-orbit coupling (SOC) is a fundamental interaction in solids that plays a crucial role in various physical phenomena and has significant implications for modern technology, particularly in the field of spintronics.

SOC has its roots in relativistic quantum mechanics and is explained through the Dirac equation. It occurs when electron spins move through an electric field, producing an effective magnetic field that depends on the momentum and affects the spin. This interaction links spin angular momentum with orbital motion of electrons, creating a coupling effect, and can be expressed in the form [21]

$$H_{\mathrm{SO}} = -\frac{\hbar}{4m^2c^2} \left(\nabla V_0\right) \cdot \left(\boldsymbol{\sigma} \times \mathbf{p}\right), \tag{2.2}$$

where $\hbar$ is a Planck constant, m indicates the electron's mass, c is the light velocity, $\mathbf{p}$ denotes the momentum operator, $\boldsymbol{\sigma} = (\sigma_x, \sigma_y, \sigma_z)$ – the vector of Pauli spin matrices, V_0 represents the potential that creates the electric field, that the electron experiences, which typically comes from atomic nuclei. When considering angular motion in the potential V_0, the interaction can be described as the relationship between the electron's orbital angular momentum $\mathbf{L}$ and its spin angular momentum $\mathbf{S} = \hbar/2\boldsymbol{\sigma}$. Because the microscopic origin of SOC comes from the

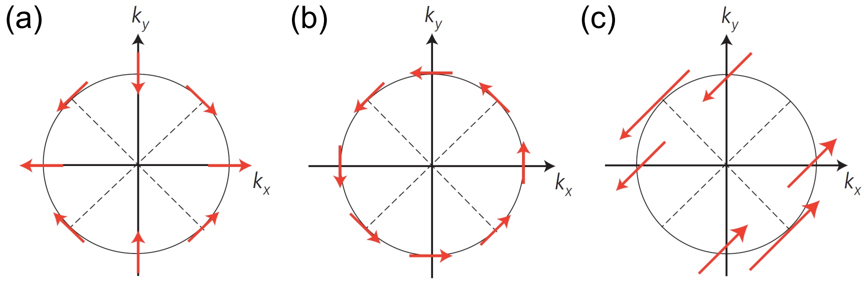

Figure 2.2: (a) Spin texture at the Fermi surface due to the Dresselhaus effect. (b) Spin texture at the Fermi surface due to the Rashbas effect. (c) When both effect are present with equal magnitude [5]. Reproduced with permission from Springer Nature.

potential of the atomic nucleus, the strength of this interaction depends on the atomic number of the elements in the material. Heavier elements with higher atomic numbers have stronger SOC [21].

The spin orientation pattern, determined by the wave vector, plays a crucial role in defining the spin texture of the material, which serves as a unique feature that distinguishes different SOC mechanisms. The spin texture is influenced by both space inversion symmetry and time inversion symmetry. When space inversion symmetry is broken, it causes the twofold spin degeneracy to lift, in other words, spins split. This manifests itself as bulk inversion asymmetry (BIA), that is the origin for Dresselhaus effect, shown in Fig. 2.2(a). In addition, it can shows up as structural inversion asymmetry (SIA), which leads to the Rashba effect, shown in Fig. 2.2(b) [21, 22].

Dresselhaus Effect

The concept of the Dresselhaus effect was introduced by Dresselhaus in his work about electronic properties of zinc-blende crystals [23]. The Dresselhaus SOC arises in materials, in which the inversion symmetry does not have a center, such as GaAs and InSb, and results in a spin splitting that is influenced by the crystallographic direction (see Fig. 2.2(a)). Mathematically, this effect can be described as an additional term in the system Hamiltonian [24]

$$H_{\mathrm{D}} = \gamma \left[\sigma_x k_x \left(k_y^2 - k_z^2\right) + \sigma_y k_y \left(k_z^2 - k_x^2 + \sigma_z k_z \left(k_x^2 - k_y^2\right)\right)\right]. \tag{2.3}$$

Here γ indicates a bulk Dresselhaus SOC coefficient which is a material constant, k_x, k_y, k_z are electron wavenumbers [5, 24]. In a zinc-blende semiconductor quantum well in the case of strain in (001) crystallographic direction, one can pass from the cubic Dresselhaus effect, represented by Eq. (2.3), to the linear Dresselhaus SOC [24]

$$H_{\mathrm{D1}} = \beta_1 \left(k_x \sigma_x - k_y \sigma_y\right), \tag{2.4}$$

where was used the fact that the wave vector component is quantized ($k_z = 0$, $k_z^2 \rightarrow \langle k_z^2 \rangle \rightarrow$ const) and $\beta_1 = -\gamma \langle k_z^2 \rangle$ represents a linear Dresselhaus coefficient. The coefficient of the cubic Dresselhaus SOC γ is difficult to control, but it can be possible for the case of the linear

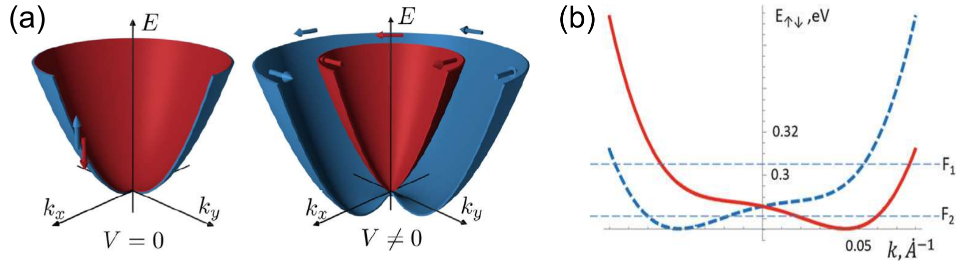

Figure 2.3: (a) Energy levels of 2DEG has a spin degeneracy in the presence of inversion symmetry (left). An external electrostatic potential V breaks the inversion symmetry that results into the Rashba splitting of levels (right) [28]. (b) Rashba spin splitting in TI quantum well. $F_{1,2}$ indicates the position of the Fermi level, the gap parameter $M_0 = 0.28$eV, the gate voltage $V_g = 0.3$eV [29].

Dresselhaus SOC through its coefficient β_1 by the thickness of the quantum well. Also, the strength of the spin splitting due to the Dresselhaus effect can be regulated by the density of carriers.

Rashba Effect

The idea of Rashba SOC was proposed by Sheka and Rashba [25] (after whom it was later named) in 1959 for 3D systems and then was discovered by Vas'ko [26], Bychkov and Rashba [27] for 2D systems (Fig. 2.2(b)).

The Rashba effect arises when an electric filed, perpendicular to the plane of the material interacts with the electron's spin, leading to a linear spin splitting in momentum space, as shown in Fig. 2.3(a) [5]. In other words, the carrier's spin angular momentum $\boldsymbol{\sigma}$ and its linear momentum $\mathbf{k}$ become linearly coupled. This interaction can be written as [30]

$$H_{\mathrm{R}} = \alpha_{\mathrm{R}} \boldsymbol{\sigma} \cdot (\mathbf{k} \times \hat{\mathbf{z}}) \,, \tag{2.5}$$

where $\hat{\mathbf{z}}$ is a normal to the interface, α_{R} indicates the Rashba constant including all parameters characterizing the material. There is also another name of this model – Bychkov-Rashba model. This model clearly demonstrates that materials that have heavy elements, like Pt, Bi, Pb, Au, shows greater spin splitting owing to their significant atomic spin-orbit connection.

The Rashba effect follows from the coexistence of the inversion symmetry breaking (ISB) and atomic SOC. In addition to this, ISB induces the orbital angular momentum, which becomes momentum-dependent that results in the Rashba spin-momentum locking. For the maximization of the Rashba effect, it is needed to find the compromise between atomic SOC and ISB crystal field [30].

A variety of materials and systems can exhibit Rashba SOC. It was observed in semiconductor heterostructures, such as GaAs/AlGaAs, InGaAs/InAlAs, and similar combinations that are classic examples of the prominent Rashba effect. Also, transition metal dichalcogenides (TMDs), such as MoS_2 and WSe_2, ferromagnetic materials, cold-atom systems and graphene demonstrate significant Rashba effects [5, 24, 30–32].

Topological insulators (TIs) and Rashba systems share a lot of similarities, such as their behavior in response to magnetic fields oriented differently, direct and inverse Edelstein effects, charge-to-spin conversion, as well as the anomalous Hall effect, the spin Hall effect, the quantum spin Hall effect, the quantum anomalous Hall effect. Nevertheless, in comparison to Rashba systems, surface states of TIs have the advantage of topological protection for their electronic states [30]. The underlying physics at the surface/interfaces of TIs can be elucidated by employing a Rashba-like Hamiltonian, where the parameter α_{R} is replaced by the electron's velocity v within the Dirac cone [20, 30]

$$H_0 = v\left(k_x\sigma_y - k_y\sigma_x\right). \tag{2.6}$$

Consequently, the phenomenon of spin-momentum locking within the surface states of the Dirac cone reflects that of the Rashba surface states, leading to numerous shared physical characteristics between these two classes of states. Certain TIs with protected time-reversal symmetry (TRS) exhibit even complex behavior of their topological surface states (TSSs). As an example of the Rashba spin splitting in TIs, it can be mentioned the spin-resolved spectrum, shown in Fig. 2.3(b), where band inversion and the momentum dependent Rashba coefficient affects the symmetry in momentum space in the TI quantum well [29]. The magnitude of this spin separation is consistent with what is observed experimentally in TI Bi_2Se_3 [33].

The unique properties of SOC have led to various applications in modern technologies, especially in the field of spintronics. SOC allows manipulation of electrons spins by electric fields, leading the development of spin transistors, spin valves and other spin-based devices. Materials with strong SOC, such as TIs, offer reliable quantum computing. SOC-induced phenomena can be used in next generation magnetic memories and logic devices [5, 24, 30].

2.3 Current-Induced Spin Polarization

The ability to control the spin orientation with an electric current offers possibilities for the development of efficient spin-based technologies. Because of this, the effect of current-induced spin polarization (CISP) attracted significant attention in the fields of spintronics and condensed matter physics. As a consequence of the large number of studies of this effect, CISP has several names that are used in the literature: the (direct) Edelstein effect (DEE), current-induced spin accumulation, charge-to-spin current conversion, inverse spin-galvanic effect, magneto-electric effect, etc [36].

The concept of CISP was first theoretically proposed in 1990 by Edelstein, after whom this effect has also another name – the Edelstein effect [37]. In addition, it was predicted by Aronov and others that this effect can appear in systems with Rashba SOC [38]. Also, in that time a close relationship between DEE and spin Hall effect (SHE) was demonstrated by D'yakonov

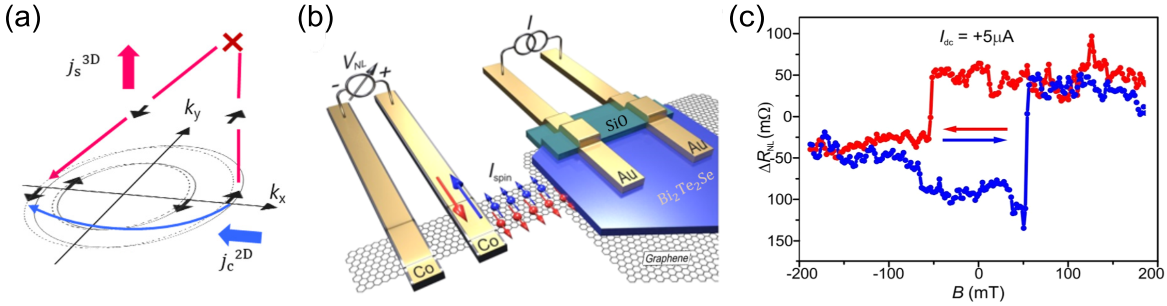

Figure 2.4: (a) Fermi contour with DEE. A momentum scattering at the interface is denoted by blue arrows, while magenta arrows show the spin transmission across the interface and red cross indicates spin flip [34]. (b) Spintronic device with the generated in TI (Bi_2Te_2Se) spin current which is injected into graphene. Au electrodes make the polarity of the applied bias current, while Co electrodes are used for detecting the spin current [35]. (c) Nonlocal electrical resistance change when the magnetization direction of the magnetic detector electrode is reversed relative to the incoming spin current. The measurement is taken at a bias current of $I_{\mathrm{dc}} = +5\mu\mathrm{A}$ when the maximum signal was observed [35].

and Perel' [39].

CISP is the effect where an external electric field generates a net polarization via SOC in a non-magnetic system in which inversion symmetry is broken, as shown in Fig. 2.4(a). In this system, both bulk and interface states are involved. The DEE effect converts the 2D charge current $j_{\mathrm{c}}^{\mathrm{2D}}$, that applied along the x-direction, into a 3D spin current $j_{\mathrm{s}}^{\mathrm{3D}}$ in the bulk, with spins polarized perpendicular to the charge current in the y-direction. This also leads to the spin accumulation at the interface. In addition, this spin accumulation is influenced by two processes that do not depend on each other – momentum scattering in the interface state and spin leakage from the interface to the bulk state, as illustrated in Fig. 2.4(a). To characterize CISP, a coefficient is used, which is defined as $q_{\mathrm{DEE}} = j_{\mathrm{s}}^{\mathrm{3D}}/j_{\mathrm{c}}^{\mathrm{2D}}$ [30, 34].

CISP can be observed across a variety of materials and systems, typically those with strong SOC and without inversion symmetry. These are the systems that ranging from Rashba systems, such as non-centrosymmetric semiconductors and systems with two-dimensional electron gas (2DEG) to metallic heterostructures, ferromagnetic materials [40, 41]. It is also found in topological insulators (TIs) and Weyl semimetals [42–44]. In TIs, CISP is particularly effective due to spin-momentum locking [35, 45, 46]. This makes TIs more efficient for CISP than other materials. When TIs are combined with materials like graphene – known for its hexagonal lattice structure and weak SOC – spin manipulation can be significantly improved. An example device is shown in Fig. 2.4(b), consisting of two main components: a spin injector and a spin generator. Graphene, with its weak SOC, serves as ideal spin injector, while TIs, with their ability to generate spin currents due to spin-momentum locking of surface states, are excellent as spin generator. Due to the injection of spin-polarized current from the Bi_2Te_2Se surface states

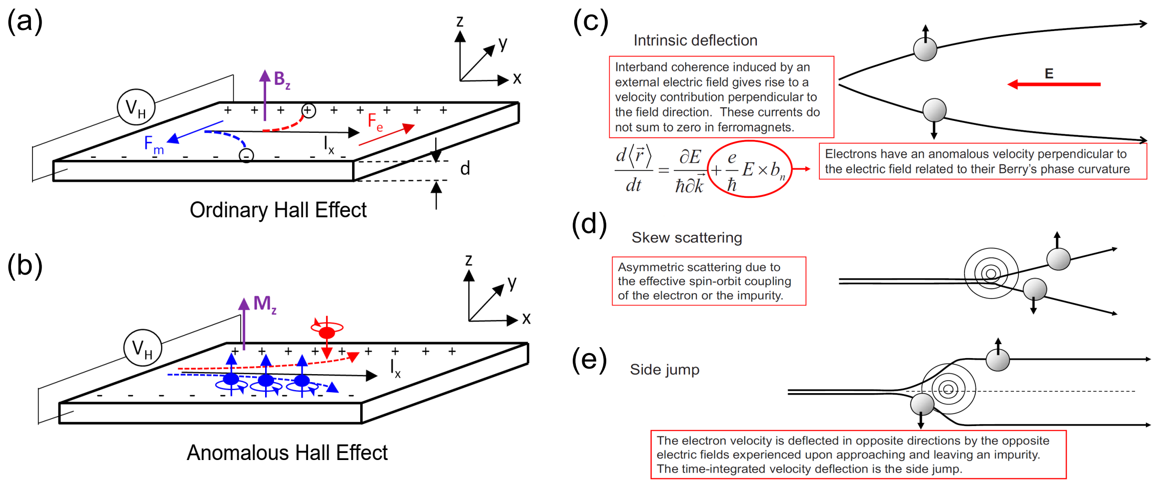

Figure 2.5: (a) Schematic of the ordinary Hall effect [49]. (b) Schematic of AHE [49]. (c) Illustration of the three main mechanisms that lead to AHE [50].

into the graphene, it can be observed in Fig. 2.4(c) the nonlocal resistance change in accordance with change of direction of magnetic detector electrode magnetization relative to the incoming spin current [35, 47].

CISP has opened new avenues in the field of spintronics, providing a path to advanced devices, such as magnetic sensors and spin-torque oscillators. This effect also offers advantages over traditional charge-based electronics as spin-based transistors, memory devices with higher efficiency and faster processing speeds [35, 48].

2.4 Hall Effects Induced by Spin-Orbit Coupling

The Hall effect, sometimes called the ordinary, original or conventional Hall effect, is a key concept in condensed matter physics. It describes as the generation of a voltage difference (known as the Hall voltage) in a conductor or semiconductor. This takes place when a magnetic filed is applied perpendicular to the direction of the electric current flow in the material, as shown in Fig. 2.5(a). This phenomenon was first discovered by Edwin Hall in 1879 [51, 52]. Over time, several variations of the Hall effect have been discovered, each of which provides a unique insight into how electrons behave in materials [9, 49]. These discoveries have found applications ranging from precise measurements in metrology to advanced technologies in spintronics. The Hall effect remains bright and significant area of research in both condensed matter physics and materials science.

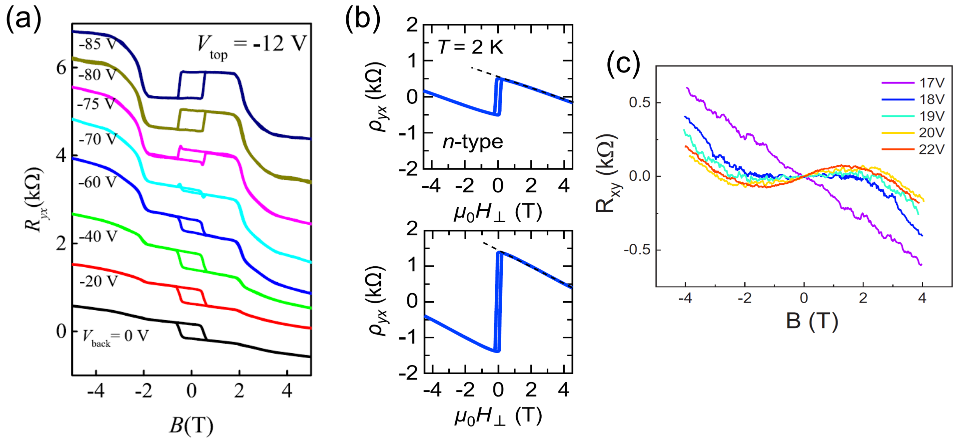

Figure 2.6: (a) AHE in magnetic TIs $MnBi_2Te_4$ at different the back gate V_{back} when the top gate $V_{\text{top}} = -12$ V and $T = 2$ K, offset by 0.8 kΩ [54]. (b) The anomalous Hall resistivity (ρ_{yx}) at 2 K in TIs with ferromagnetic insulators [55]. (c) AHE of the graphene/magnetic semiconductor [56].
(a) Reprinted with permission from S. Zhang, R. Wang, X. Wang, B. Wei, B. Chen et al.: Nano Lett. **20**, 709 (2020). Copyright (2020) American Chemical Society. (b) Reprinted with permission from M. Mogi, T. Nakajima, V. Ukleev, A. Tsukazaki, R. Yoshimi, M. Kawamura, K. S. Takahashi, T. Hanashima, K. Kakurai, T.-h. Arima, M. Kawasaki, Y. Tokura: Phys. Rev. Lett. **123**, 016804 (2019). Copyright (2019) by the American Physical Society. (c) Reprinted with permission from H.-D. Song, P.-F. Zhu, J. Fang, Z. Zhou, H. Yang, K. Wang, J. Li, D. Yu, Z. Wei, Z.-M. Liao: Phys. Rev. B **103**, 125304 (2021). Copyright (2021) by the American Physical Society.

2.4.1 Anomalous Hall Effect

To create the anomalous Hall effect (AHE), one needs materials with magnetic characteristics. Also, the necessary components of this effect are strong SOC and an electric current that will flow through the material. This phenomenon does not require the application of an external magnetic field. It results in a transverse Hall voltage that depends on the material's magnetization, which is oriented out of the material's plane, as shown in Fig. 2.5(b), in contrast to the ordinary Hall voltage which is proportional to the applied magnetic field [49, 53].

AHE was first observed by Edwin Hall in the 1880s, soon after his discovery of the ordinary Hall effect. While studying ferromagnetic materials, Hall noticed an additional contribution to the Hall voltage that was not accounted for by the Lorentz force alone. For a long time, AHE posed a difficult problem for explanation due to its complex relationship with the principles of topology and geometry, which were developed only in recent years. Only after the adoption of Berry's phase approach, a significant breakthrough was achieved in establishing a correlation between the topological characteristics of Hall currents and AHE [50].

The origin of AHE is fundamentally different from the ordinary Hall effect. As the ordinary Hall effect is the result of the Lorentz force, AHE is caused by spin-orbit interaction in the material. The key mechanisms leading to AHE include intrinsic mechanism $\sigma_{xy}^{\text{AH-}int}$, skew scattering $\sigma_{xy}^{\text{AH-}skew}$ and side-jump mechanism $\sigma_{xy}^{\text{AH-}sj}$ (Figs. 2.5(c)-(e)) that can be provided by the equation [50]

$$\sigma_{xy}^{\text{AH}} = \sigma_{xy}^{\text{AH-}int} + \sigma_{xy}^{\text{AH-}skew} + \sigma_{xy}^{\text{AH-}sj}. \tag{2.7}$$

The intrinsic mechanism is related to the topological properties of the Bloch states which arises from the electronic structure with SOC [57]. The contribution of this mechanism depends only on the band structure of the material, hence it is called "intrinsic" (Fig. 2.5(c)). Microscopically, the intrinsic contribution can be defined as the dc limit to the interband conductivity and can be connected with semiclassical theory through a momentum-space Berry-phase related contribution to the anomalous velocity [50]. In the result, the intrinsic contribution to the conductivity can be calculated from the Kubo formula for the Hall conductivity for an ideal lattice [50]

$$\sigma_{xy}^{\text{AH-}int} = -\varepsilon_{ijl}\frac{e^2}{\hbar}\sum_n \int \frac{d\mathbf{k}}{(2\pi)^d} f\left(\varepsilon_n\left(\mathbf{k}\right)\right) b_n^l\left(\mathbf{k}\right), \tag{2.8}$$

where ε_{ijl} is the antisymmetric tensor, $\boldsymbol{a}_n\left(\mathbf{k}\right) = i\langle n, \mathbf{k}|\nabla_k|n, \mathbf{k}\rangle$ is the Berry phase connection, $\boldsymbol{b}_n\left(\mathbf{k}\right) = \nabla_k \times \boldsymbol{a}_n\left(\mathbf{k}\right)$ is the Berry-phase curvature, corresponding to the states $\{|n, \mathbf{k}\rangle\}$ [50,58].

The skew-scattering mechanism of AHE (Fig. 2.5(d)) can be revealed when impurities in the material scatters asymmetrically the conduction electrons [59]. To define this contribution, it can be used the traditional Boltzmann transport theory with a negligence of interband coherence effects. In the result, the contribution of this mechanism will be proportional to the Bloch state transport lifetime τ [50,58].

The side-jump mechanism appears because of a side-step scattering when impurities are present in the material (Fig. 2.5(e)). For defining the contribution of this mechanism, the traditional Boltzmann transport theory does not suit because there are no microscopic details of the scattering process [60]. It is difficult to separate contributions from intrinsic and side-jump mechanisms during dc measurements, because both are independent of τ, but they can be separated experimentally (and also theoretically) if, firstly, to define the intrinsic contribution $\sigma_{xy}^{\text{AH-}int}$ during the extrapolation of the ac interband conductivity. After this, it can be used the specific definition for the contribution of the side-jump mechanism in a form of $\sigma_{xy}^{\text{AH-}sj} = \sigma_{xy}^{\text{AH}} - \sigma_{xy}^{\text{AH-}skew} - \sigma_{xy}^{\text{AH-}int}$ [50].

AHE can be observed in a wide range of materials, particularly those with strong ferromagnetism or significant SOC, including transition metal dichalcogenides (TMDs) [61], ferromagnetic semiconductors [62,63], Heusler alloys [64,65], metallic ferromagnets [66], metallic spin-glass systems [50], topological insulators (TIs) [54,55] (Figs. 2.6(a)-(b)), graphene (in the combination with other materials due to weak SOC) [56] (Fig. 2.6(c)) and many others.

AHE is a fundamental physical phenomenon that has a wide range of applications. It is a powerful tool for studying magnetic effects and material characterization [49,53]. AHE has several important applications in spintronics and magnetic sensing. This effect can improve the energy efficiency and writing speed of magnetoresistive random access memory (MRAM) devices, resulting in low-power and high-performance data storage solutions [50,67]. AHE plays a key role in developing spin-based transistors through the control over spin polarization and charge currents. This paves the way for spintronic logic devices, which can lead to faster and more energy-efficient computing components. Also, AHE can be implemented in devices that

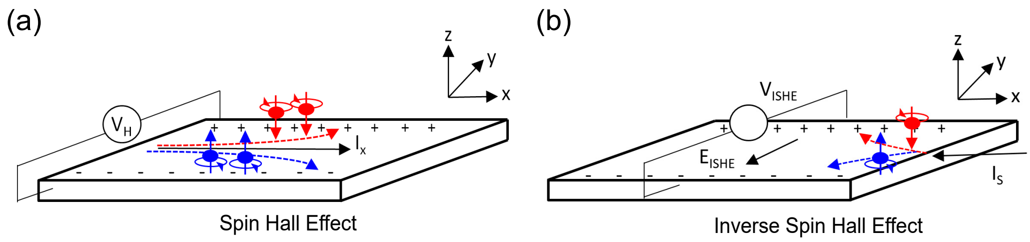

Figure 2.7: (a) SHE scheme. (b) ISHE scheme [49]. (a), (b) An open access the Creative Common CC BY License.

applies in industries aerospace and automotive purposes [49].

2.4.2 Spin Hall Effect

The spin Hall effect (SHE) is a fundamental concept in condensed matter physics. This phenomenon begins its history in 1971 from the work of D'yakonov and Perel' [39, 68, 69]. Experimental confirmation were performed in the early 2000s. The main process of SHE lies in the conversion of a 3D longitudinal charge current into a 3D transverse spin current, as shown in Fig. 2.7(a), in materials without magnetic properties.

As for AHE, spin-orbit interaction is also important for SHE, but it can arise without the magnetic field and magnetization. This means that for SHE the breaking of time-reversal symmetry (TRS) is not necessary [70, 71]. Despite this distinction, SHE and AHE share similar underlying mechanisms. There are two primary types of SHE mechanisms – intrinsic and extrinsic, which in turn lead to an intrinsic SHE and an extrinsic SHE. The intrinsic SHE appears without impurities and scattering from outside the system, and needs only spin-orbit interaction in the material. This type is often studied using the Berry phase formalism. In contrast, scattering processes, such as skew scattering and side-jump, can produce the extrinsic SHE due to distortions in the system [71, 72].

Materials with strong spin-orbit interaction, such as heavy metals [73] and TIs [74, 75] can exhibit SHE. However, it has also been explored in graphene [72, 76, 77], semiconductors [78], TMDs, oxides, alloys and many others [42, 71].

SHE is utilized in many areas, in particular quantum computing, biomolecular and magnetic sensing, and metrology of materials physical parameters. Due to the fact that SHE does not need ferromagnetic materials, SHE is a valuable tool for advancing spintronic devices, magnetic memory technologies and spin-based transistors [49, 75].

Inverse Spin Hall Effect

The first discovery of the inverse spin Hall effect (ISHE) was in 1984 by Bakun et al. They provide the investigation of photocurrents that caused by spin-orbit interaction in semiconductor [79, 80]. This phenomenon involves the conversion of an injected spin current into a transverse charge current or voltage in materials with strong SOC, as shown in Fig. 2.7(b). ISHE can be observed

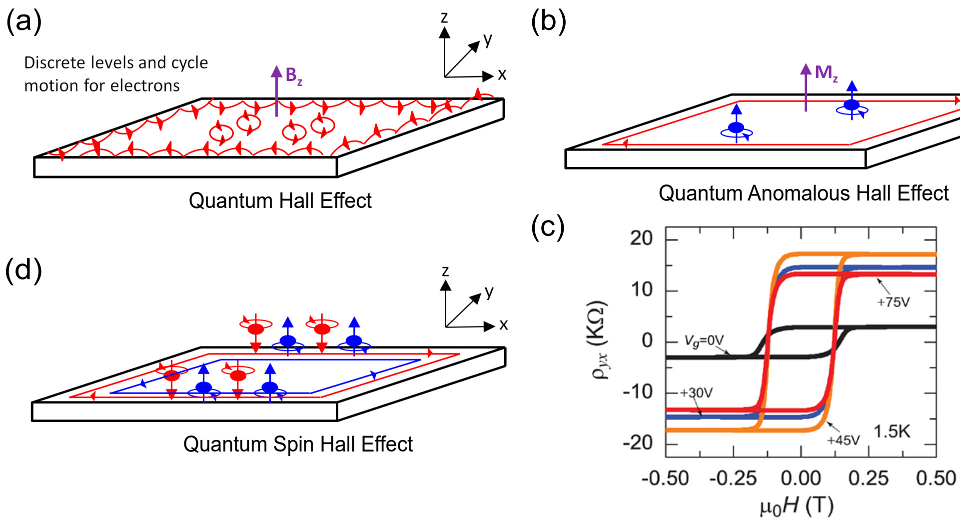

Figure 2.8: (a) QHE scheme [49]. (b) QAHE scheme [49]. (c) Experimentally measured the Hall resistance ρ_{yx} during QAHE as a function of magnetic field $\mu_0 H$ in Cr-doped $(\mathrm{Bi}_{0.1}, \mathrm{Sb}_{0.9})_{1.85}\mathrm{Te}_3$ films at $T = 1.5$ K for various bottom gate biases V_g. [81] (d) QSHE scheme [49].

in heavy metals, semiconductors and other materials. Its unique characteristics have opened up a range of applications in spintronics, quantum computing and other technological areas [42, 49].

2.4.3 Quantum Hall Effects

The quantum Hall effect (QHE) was firstly observed by von Klitzing with colleagues in 1980 [82] measuring the Hall resistance of a two-dimensional electron gas (2DEG) created by electrons in the inversion layer of a semiconductor with uncontrolled impurities under the large perpendicular magnetic field at low temperatures. Because of a magnetic field, the electronic states of the system form Landau levels, where electrons move along circular orbits, which become small and closed for large enough magnetic fields. On the other hand, electrons near to the edge of structure has wide, open orbits. The low temperature makes quantum effects important, that leads to a quantization of the area of closed orbits in the bulk, a localization of bulk electrons and a conversion of the bulk into an insulator (Fig. 2.8(a)). In addition, it was found that the Hall resistance is quantized in multiples of a fundamental constant h/e^2, where h is the Planck constant, e is the electron charge [83, 84]. For this discovery, von Klitzing was awarded the Nobel Prize in Physics in 1985.

Quantum Anomalous Hall Effect

The quantum anomalous Hall effect (QAHE) was theoretically proposed in 1988 by Haldane [85], who suggested that certain materials could exhibit QHE without an external magnetic field due to intrinsic magnetic properties, what led to the model for QHE without Landau levels.

Experimentally, this effect was finally observed in 2013 by Xue's team in Cr-doped $(\mathrm{Bi, Sb})_2\mathrm{Te}_3$ thin films [86].

QAHE, similar to QHE, requires a breaking of TRS, but unlike QHE, it does not need an external magnetic field for this. QAHE creates chiral edge states by the intrinsic magnetization. In addition to this, the manifestation of QAHE requires insulating bulk properties, strong SOC and Berry curvature. It results in the quantization of the Hall conductance in units of e^2/h (Fig. 2.8(b)) [87].

QAHE has been observed in materials with strong SOC and intrinsic magnetization, such as magnetically doped TIs (e.g., Cr-doped $(\mathrm{Bi, Sb})_2\mathrm{Te}_3$ and V-doped $(\mathrm{Bi, Sb})_2\mathrm{Te}_3$) (Fig. 2.8(c)), intrinsic magnetic TIs (e.g., $\mathrm{MnBi_2Te_4}$), moiré materials formed from graphene, and moiré materials formed from TMDs [81, 87, 88]. The unique properties of QAHE allow applications in low-power electronics, topological quantum computing, highly sensitive magnetic sensors and spintronic devices, offering new opportunities for efficient, stable and reliable technological advances in these fields [49, 87].

Quantum Spin Hall Effect

The quantum spin Hall effect (QSHE) was first theoretically predicted by Kane and Mele in 2005 generalizing the Haldane model for graphene [12]. Experimentally this effect was observed only in 2007 by Molenkamp's group for HgTe/(Hg,Cd)Te quantum wells [16]. QSHE occurs in materials with strong SOC, where electrons with opposite spins move in opposite directions along the edges, leading to spin-polarized edge currents without an external magnetic field (Fig. 2.8(d)). This effect is defined by its dependence on TRS and topologically protected edge states, which makes it different from QHE [84].

QSHE is mainly observed in TIs such as HgTe/CdTe and InAs/GaSb quantum wells, as well as materials such as TMDs and $\mathrm{Bi_2Se_3}$ compounds [89]. The important mechanisms behind QSHE are strong SOC, band inversion and Berry curvature in moment space, which collectively lead to the robust helical edge states characteristic of this effect. These edge states are protected against backscattering from non-magnetic impurities due to TRS, providing stable spin-polarized currents [84].

Applications of QSHE are promising in a variety of fields, including electronics, spintronics and quantum computing. This allows to develop spintronic devices, low-power electronic components and high sensitivity sensors [49, 89].

Chapter 3

Magnetoresistance

This chapter explores the theory behind magnetoresistance (MR) which is one of the most important phenomena in condensed matter physics and material science, characterized by a change in the electrical resistance of a material in response to an external magnetic field. One can distinguish various types of MR, that varies by their origin and underlying mechanisms. In this chapter, we will discuss the principles and material-specific observations of various type of MR [6, 90]. Understanding of the mechanisms leading to MR allows for the wide usage of this effect as a tool in modern electronics.

3.1 Introduction to the Magnetoresistance Effect

Magnetoresistance (MR) is a fascinating phenomenon that has intrigued scientists for many years. It refers to the resistance change of a material that occurs when a magnetic field is applied to a material and can be denoted by [6, 91]

$$\Delta\rho/\rho_0 = \frac{\rho\,(B) - \rho_0}{\rho_0} = \frac{R\,(B) - R_0}{R_0}, \tag{3.1}$$

where $\rho\,(B)$ ($R\,(B)$) and ρ_0 (R_0) are electrical resistivities (resistances) in magnetic fields of a magnitude B and zero, respectively. $\Delta\rho/\rho_0$ depends on the magnetic field B, i.e., its magnitude and direction as well. When the external field aligns with the current (I), MR is referred to as longitudinal MR. Conversely, when the magnetic field (B) is perpendicular to the current, the MR is termed as transverse MR [90].

In the mid-2010s, it was discovered a magnetoresistance family that appears from the generation of spin current in ferromagnet/nonmagnetic heavy metal bilayers, and was called unidirectional magnetoresistance (UMR) [92, 93]. UMR shows an asymmetric response that depends on the direction of the electric current or external magnetic field (see Fig. 3.1(a)). Two main mechanisms have been proposed to explain UMR in such systems. The first one shows UMR as a result of the spin-accumulation mechanism at the ferromagnet/heavy metal interface due to the interfacial spin chemical potential induced by the spin Hall effect (SHE) in the heavy

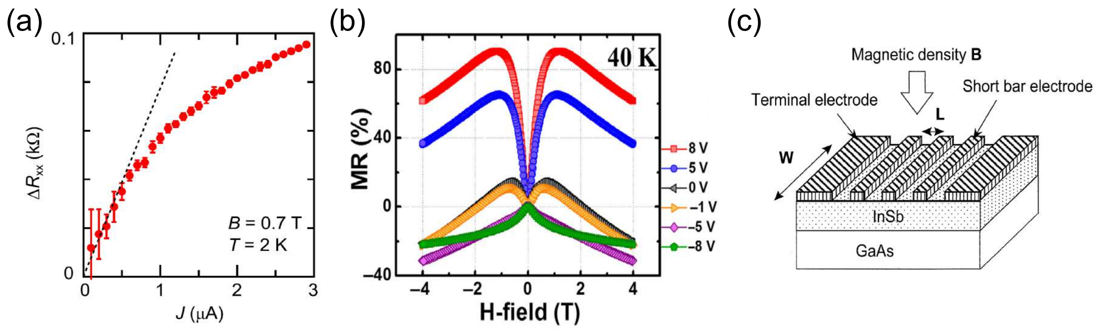

Figure 3.1: (a) Dependence of UMR ΔR_{xx} on the current J at 2 K under $B = 0.7$ T for the normal magnetic/nonmagnetic TIs. The black dotted line shows a linear relationship in a low current region [93]. (b) Electric field-controlled MR measurements at 40 K, clearly showing a transition from a negative to a positive value when the gate voltage changes from a negative to a positive bias [97]. (c) A magnetoresistance element with short bar electrodes [100].

metal layer [94, 95]. In the case of the second one, UMR is linked to electron-magnon scattering in the ferromagnetic layer originating from magnon excitations at high energies in the terahertz frequency range via spin-flip process [93].

The increasing of the electric resistivity of a material under the applied magnetic field refers to positive magnetoresistance, whereas the decreasing indicates negative magnetoresistance (Fig. 3.1(b)) [91, 96]. Positive magnetoresistance can be explained by such phenomena as, for example, the spatial fluctuations of magnetic polarons [97] or the suppression of hopping processes by the magnetic field [98]. Negative magnetoresistance can arise from electron-electron interactions, the spin-dependent scattering by magnetic polarons [97], increase of the carrier density with an application of a magnetic field, spin injection and spin detection [99] etc. A weak localization effect can lead to both positive and negative magnetoresistance [53, 91].

Since the groundbreaking discovery of the MR effect by William Thomson (Lord Kelvin) in 1857 [101], the interest in this phenomenon has experienced a significant surge in popularity owing to its vast array of applications in the magnetic recording system over the course of the last few decades. This increase in interest can be attributed to the profound impact that the MR effect has had on computer memory and storage technology [6]. Also, there was paved the way for MR-based sensor systems for biosensing and biochip systems. For example, for magnetic field sensing, magnetic memory, and magnetic recording can be used a MR element with short bar electrodes, shown in Fig. 3.1(c). It consists of a thin film or layer of a magnetoresistive material. The material is patterned into a narrow strip or bar shape. Electrode contacts, usually made of a conductive material, are placed at the ends of the strip to provide electrical connections [100]. The specific material choice depends on the desired sensitivity, operating conditions, and targeted application.

3.2 Classification

There are various types of magnetoresistance, each with its own distinct mechanisms and characteristics. Ordinary magnetoresistance (OMR), anisotropic magnetoresistance (AMR), giant magnetoresistance (GMR), tunneling magnetoresistance (TMR), colossal magnetoresistance (CMR), spin Hall magnetoresistance (SMR) are some of the prominent classifications that have been extensively studied and utilized in different scientific and technological applications [6]. The materials and mechanisms responsible for these particular types of magnetoresistance exhibit significant distinctions.

3.2.1 Ordinary Magnetoresistance

Ordinary magnetoresistance (OMR), which is generally observed in bulk materials, such as metals or semiconductors, arises from the deflection of electrons away from the direction of the electric field due to the influence of the Lorentz force. This is manifested by the high electrical resistance as the magnetic field becomes stronger [102]. This type of magnetoresistance always has positive values regardless of how the magnetic field is aligned with the electric current. OMR can be represented as [6, 103]

$$\mathrm{MR} \propto H^2 \left(\omega_c \tau \ll 1\right), \tag{3.2}$$

$$\mathrm{MR} \propto const \left(\omega_c \tau \gg 1\right), n \neq p, \tag{3.3}$$

where $\omega_c = eH/2\pi m_e$ denotes the cyclotron frequency, which describes the motion of an electron under a magnetic field H and depends also on the electron charge e and mass m_e, τ is the relaxation time. Eq. (3.2) is for the case of small magnetic fields or for the stoichiometric semiconductors with the equal concentrations of electrons n and holes p. Eq. (3.3) corresponds to nonstoichiometric materials that reach the saturation with strong magnetic fields.

Because of high sensitivity of OMR to magnetic fields and its easy implementation OMR is effective for a wide range of application [6, 104, 105]. This effect is often employed in the area of sensors. For magnetic sensors, it performs the function of detecting and measuring the intensity of magnetic fields. Additionally, OMR finds utility in current sensors designed to accurately gauge electric currents flowing through materials. Also, it can be applied in systems that enable the tracking of position and movement by catching the response to variations in magnetic fields when objects move.

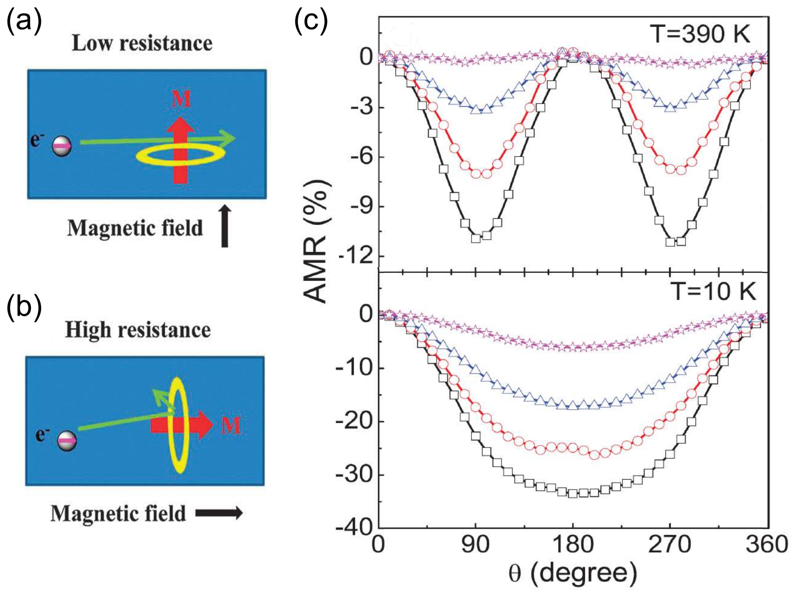

Figure 3.2: The AMR effect scheme. (a) The magnetic field and magnetization are perpendicular to the electrical current [6]. (b) The magnetic field and magnetization are parallel to the electrical current. M denotes a magnetic moment [6]. (c) AMR in multilayer graphene doped on SiO_2 as a function of θ at 390 K (top) and 10 K (bottom) under various magnetic fields [107].

3.2.2 Anisotropic Magnetoresistance

Anisotropic magnetoresistance (AMR) represents an intriguing and complex physical phenomenon that has significant prospects for applications in cutting-edge technological areas such as spintronics and quantum computing. This effect manifests itself as a variation in the electrical resistance which affected by the interplay between the orientation of the current flow axis and the specific direction of magnetization or the applied magnetic field. This can be described by Voigt-Thompson formula [106]

$$\rho_{\mathrm{AMR}}(\varphi) = \frac{1}{2}\left(\rho_{\parallel} + \rho_{\perp}\right) + \frac{1}{2}\left(\rho_{\parallel} - \rho_{\perp}\right)\cos 2\varphi, \tag{3.4}$$

where $\rho_{\parallel}$ is an electrical resistivity measured for parallel configuration between the magnetic filed (or magnetization) and an electrical current, $\rho_{\perp}$ is an electrical resistivity measured during perpendicular configuration, φ indicates the angle between the electric and magnetic fields.

The underlying physical mechanisms that give rise to the AMR effect can be ascribed to phenomenon of spin-orbit coupling (SOC) [108, 109]. The rotational change of the applied magnetic filed or magnetization leads to the deformation of the electron cloud that wraps each atomic nucleus, which in turn affects scattering processes of the conduction electrons during their travel through the material lattice structure. This takes place due to the rotation in the orientation of the closed electron orbits with respect to the direction of the electric current flow in the result of the rotation of the external magnetic field or magnetization (Figs. 3.2(a)-(b)).

When orientations of the magnetic field and magnetization are positioned perpendicular to the trajectory of the current, the electronic orbits tend to align within the plane of the electric field. This diminishes scattering and is characterized by low resistance. Conversely, in the cases where is a parallel alignment between the magnetic filed (magnetization) and the current flow, the orientation of the electronic orbits shifts to the position, perpendicular to the current. These states experience the high resistance.

AMR is observed in a wide range of materials, including ferromagnets [110, 111], Dirac and Weyl semimetals [112–114], etc. Recently, AMR has been observed in graphene, what is remarkable because it has demonstrated the potential of graphene in spintronic application, extending its usefulness beyond its known charge transport capabilities. Due to the low SOC in graphene, AMR can be detected when graphene is interfaced to the proper substrate or using cover layers, gate voltages, electric fields, etc [115]. The graphene structure and specific external conditions can have an influence on AMR in this material. For instance, the absolute value of AMR for graphene doped on SiO_2 at the angle $\theta = 180^\circ$ between the magnetic field and the normal direction of the sample's plane increases with decreasing the temperature and can reach the maximum under the magnetic field $H = 7$ T at 10 K, as presented on bottom of the Fig. 3.2(c) [107]. Also, with increasing of the magnetic field H AMR has a two-fold symmetry for different θ at 390 K, but at 10 K it demonstrates a one-fold symmetry (see Fig. 3.2(c) (top and bottom)). It can be caused by the anisotropic scattering of carriers in the system.

AMR in topological insulators (TIs) is an interesting phenomenon that arises due to the combination of the unique properties of TIs (Section 2.1) and the interaction with an external magnetic field [116–118]. Recent studies have revealed that the emergence of AMR can be attributed to the chiral anomaly and nonvanishing Berry curvatures in TIs, wherein the existence of nontrivial topology leads to the emergence of an interband contribution to conductivity [119–124].

AMR in TIs also can be related to some anisotropic scattering mechanisms [22, 125–127]. For example, in the case of magnetic proximity mechanism, a TI should be placed in contact with a ferromagnetic material. Then the magnetic proximity effect induces an exchange interaction at the interface to the surface states of the TI and opens an energy gap at the conducting surface states giving rise to AMR [116, 128]. In case of the formation of magnetic clusters through exchange interactions between impurities in TI doped with magnetic atoms, AMR appears due to the combination of spin-momentum locking and scattering of the surface electrons in the TI influenced by the magnetic moment direction of the clusters [129]. Also, nonlinear lattice effects, like structural distortions and deformations, can affect AMR in TIs by changing the scattering potentials. Such distortions result in directional differences in electron scattering and thus resistance [130]. In addition to these mechanisms, AMR can be caused by breaking TRS due to the applied magnetic field. In that case, broken TRS results in elimination of backscattering prohibition for surface Dirac fermions whose spins are perpendicular to the applied magnetic field. For the remaining spins, backscattering is still forbidden. This anisotropy in the scattering gives rise to AMR [7, 10, 131, 132]. Besides, AMR can appear due to coupling between surface

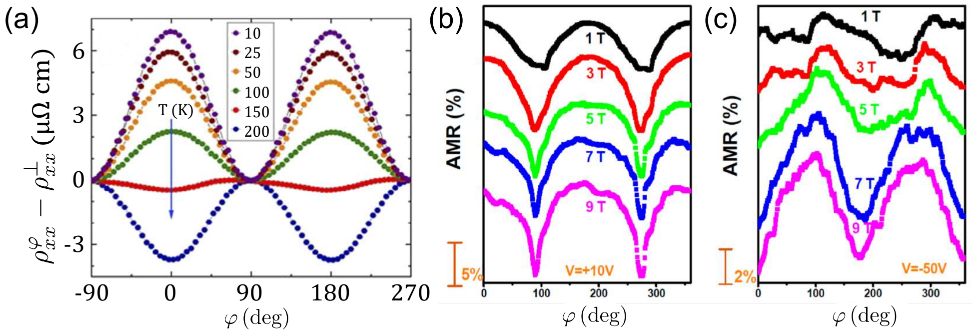

Figure 3.3: (a) AMR $\Delta\rho_{xx}$ of $Bi_{85}Sb_{15}$ TI films as a function of the angle φ between the current and the applied magnetic filed (9 T) for different temperatures from 10 K to 200 K. Here was done the symmetrization of the plus and minus field response [120]. (b) and (c) Angular dependence of the in-plane AMR ratio at temperature 2 K in $BiSbTeSe_2$ flakes for various values of the magnetic field under +10 V (b) and -50 V (c) gate voltages [134].

states in the presence of the magnetic field that shifts the Dirac point in momentum space. During this, spin polarization is generated, which results in the anisotropic spin scattering [131, 133]. In the latter cases, it was found that AMR can change the sign as the temperature increases to the critical resistivity anomaly temperature around 150 K, as shown in Fig. 3.3(a)) [120, 124, 131].

Due to the presence of spin-momentum locking of the surface states in TIs, the electric field can be used to manipulate the AMR [134, 135]. In Figs. 3.3(b)-(c) it is illustrated the dependence of the in-plane AMR ratio on the angle between the magnetic field and the current in $BiSbTeSe_2$ flakes for different values of the magnetic field with +10V and -50V gate voltages. The difference in the sign of the AMR oscillation for these two gate voltages can be determined by the sign of the spin polarization. The net spin polarization is induced by the splitting of topological surface states (TSSs), similar to the Rashba effect, due to the applied in-plane magnetic field and spin-momentum locking. As Dirac electrons and holes in TSSs have opposite spin helicities, the net spin polarization changes the sign when the Fermi level goes across the Dirac point. As a consequence of this reversal, AMR also undergoes a reversal in sign.

The deep-seated understanding of the origins of AMR in TIs and other materials holds immense promise for the development of advanced electronic and spintronic devices. The orientation-dependent nature of AMR in these materials offers opportunities for the creation of highly sensitive magnetic field sensors, information processing technologies, and novel quantum devices. [124] Because AMR is sensitive to various control parameters and easy to measure, it can be used as a probe for different spin phenomena, such as spin-polarized edge states [136], spin injection and pumping [137, 138], spin wave and magnon states [139], spin torque [140], spin tunneling [141], spin Hall effect (SHE) [78, 142, 143], and others.

3.2.3 Magnetoresistance in Multilayer Systems

MR is a leading phenomenon observed in magnetic multilayers. In these multilayers, the orientation of the magnetization of ferromagnetic layers can be manipulated by an external magnetic field, leading to changes in electrical resistivity (or resistance). Specifically, when the magnetizations are aligned parallelly, the electrical resistivity is low, whereas it increases significantly when the magnetization aligns antiparallel. There are two types of MR, which is influenced by the relative alignment of magnetizations rather than the angle between magnetization and current flow. The distinction between them arises from the nature of the non-magnetic layers present within the multilayers, with metallic layers leading to giant magnetoresistance (GMR) and insulating layers giving rise to the tunneling magnetoresistance (TMR) effect. In the case of TMR, the current passes through the insulator using tunneling mechanisms, which leads to the creation of a magnetic tunnel junction (MTJ). In addition, it is important to notice another prominent MR phenomenon that is observed in multilayer systems and is known as colossal magnetoresistance (CMR). A significant difference between CMR and GMR lies in the fact that CMR is preferably observed at low temperatures with the applied external magnetic fields that are still significantly larger than those necessary for practical applications [144, 145].

Giant Magnetoresistance

Giant magnetoresistance (GMR) is a fascinating effect that has a big influence on various areas, including spintronics, magnetic sensors and data storage devices. This effect was first discovered in the late 1980s by Albert Fert and Peter Grünberg [146, 147] (Fig. 3.4(a)), who were awarded the Nobel Prize in Physics in 2007 for their groundbreaking work. This stimulated big research efforts, aimed at comprehending the fundamental physics responsible for GMR, and its technological possibilities. GMR is observed in a wide range of magnetic materials, from nanoparticles to permanent magnets and multilayered structures [148]. These structures are composed of combinations of ferromagnetic and either antiferromagnetic or non-magnetic metals [149–151]. This phenomenon also has been found in granular systems [152, 153], that can contain carbon-based materials like carbon nanotubes and graphene [154, 155]. Furthermore, GMR has been observed in organic materials [156] and spin-valve sandwich structures [157].

The GMR effect refers to the significant change in the electrical resistance observed in metallic layered systems when the magnetizations of the ferromagnetic layers are altered by an external magnetic field. GMR was characterized as the ratio $\frac{\Delta R}{R} = \frac{R_{\mathrm{AP}}-R_{\mathrm{P}}}{R_{\mathrm{P}}}$, where R_{P} and R_{AP} are the resistances of the materials for parallel and antiparallel alignments of two magnetic electrodes, depending on the magnetization state of the materials under an applied magnetic field (Fig. 3.4(b)). In the context of a parallel magnetic configuration (Fig. 3.4(b) (top)), electrons with a specific spin direction can pass all magnetic layers with minimal resistance, which leads to a decreasing of the resistance. Conversely, in the antiparallel configuration (Fig. 3.4(b) (bottom)), electrons within each channel experience deceleration at each subsequent magnetic layer, thereby

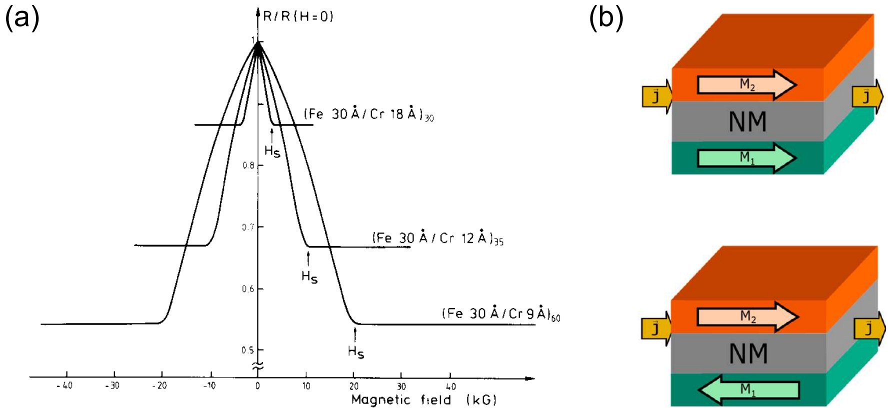

Figure 3.4: The GMR effect. (a) GMR in the multilayers of Fe-Cr superlattices [146]. (b) Schematic of the mechanism of GMR double layer in current in-plane configuration for a parallel alignment of magnetizations M_1 and M_2 (top), and an antiparallel alignment (bottom). NM represents non-magnetic layers [158].

causing increased resistance. This can be explained by the fact that the effect is generated by the spin-dependent transport of electrons in magnetic metals [1, 6, 158].

The discovery of GMR has had a profound impact on various technological advances. GMR has revolutionized the field of magnetic sensors. GMR sensors, based on the principles of GMR, are widely used in applications such as magnetic field detection, compasses, non-destructive testing, medical diagnostics, environmental monitoring, and aerospace technology [159–162]. One of the first significant applications of GMR is in data storage devices, particularly hard disk drives (HDDs) [163–165]. GMR has also paved the way for advancements in the field of spintronics, which explores the manipulation of electron spin for information processing and storage [166, 167].

Tunneling Magnetoresistance

Another type of MR occurs when the nonmagnetic metal is substituted with an insulating barrier, giving rise to the tunneling magnetoresistance (TMR). This particular effect stands as one of the fundamental phenomena in spintronics, showing possibilities for practical implementations in sensing and information technologies.

TMR is a phenomenon observed in a magnetic tunnel junction (MTJ), which consists of two ferromagnetic electrodes separated by a thin insulating layer called the tunnel barrier. The resistance in this structure depends on the alignment of the magnetic configurations of the two electrodes – whether they are parallel or antiparallel. When electrons travel between the ferromagnetic layers, they carry out the tunneling process with preserved spin (Fig. 3.5) [6]. This tunneling is easier when the magnetizations of the layers are parallel, as shown in Fig. 3.5(a). In

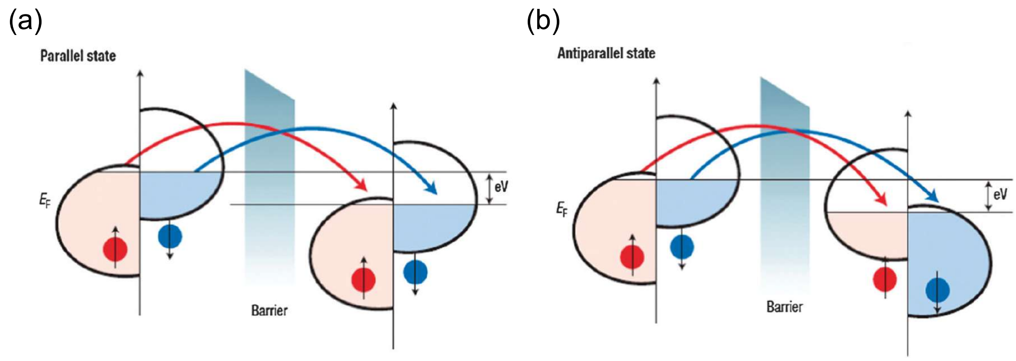

Figure 3.5: Schematic of the parallel magnetization (a) and the antiparallel magnetization (b) in the TMR effect [6]. Used with permission of Z. Guo, from An overview of the magnetoresistance phenomenon in molecular systems, H. Gu, X. Zhang, H. Wei, Y. Huang, S. Wei, Z. Guo: Chem. Soc. Rev. **42**, 5907 (2013); permission conveyed through Copyright Clearance Center, Inc.

contrast, tunneling becomes more difficult when the magnetizations are antiparallel, as illustrated in Fig. 3.5(b), leading to the higher resistance. This happens because there is spin polarization of the electronic states on either side of the barrier. This difference in resistance is a key for TMR and can be described as $\frac{\Delta R}{R} = \frac{R_{\mathrm{AP}}-R_{\mathrm{P}}}{R_{\mathrm{P}}}$, where R_{P} and R_{AP} are the resistances of the materials for parallel and antiparallel alignments, respectively [168].

The discovery of TMR is credited to M. Julliere, who first described it in 1975 [169]. He explored this effect in the ferromagnetic films, specifically in Fe-Ge-Co tunnel junction system, and found that TMR depends on the relative orientation of the magnetizations. Furthermore, TMR was obtained in different tunnel junction systems, such as signal-crystal epitaxial junctions [170, 171], MTJ systems based on carbon nanotubes [172], and MTJ systems with organic semiconductor barriers [173, 174]. Additionally, TMR effect has been investigated in systems incorporating topological insulators [175–177] and graphene [178, 179].

The unique properties of TMR have opened up exciting possibilities for its application in various fields. TMR has revolutionized the area of magnetic data storage, enabling the development of magnetic random access memories (MRAM), which offers non-volatile, high-speed, and low-power data storage [180–182]. TMR is also used in magnetic sensors [183, 184] and read heads in hard disk drives [185]. In the realm of spintronics, TMR paved the way for the development of advanced magnetic logic devices [186, 187]. These use the magnetic state of MTJs to perform logical operations, offering new opportunities for the emergence of next-generation computing systems and information processing technologies.

Colossal Magnetoresistance

After several years from the discovery of GMR, there were opened up the materials, which can demonstrate the change of an electric resistance not by several percent, but by orders of magnitude. A large MR has been called a colossal magnetoresistance (CMR) to distinguish these materials from GMR compounds.

CMR is linked to phase transitions like ferromagnet-paramagnet, antiferromagnet-paramagnet, metal-insulator, etc., that take place at low temperatures and the applied magnetic field. This effect has been reported in manganite perovskite structures, pyrochlores, spinel compounds and others [188–192]. The CMR ratio, defined as $\Delta R/R(H) = (R(0) - R(H))/R(H)$, where $R(0)$ and $R(H)$ represent the resistance in the absence and presence of a magnetic field H, converted to a percentage, can reach up to $127\ 000\%$ near $77K$, demonstrating a substantial change in the electrical resistivity by over 1000 times [193]. In an alternative definition $\Delta R/R(0) = (R(0) - R(H))/R(0)$ the CMR ratio is 99.92%, which is also significant. These remarkable results have prompted experimental and theoretical studies of manganites and the CMR effect by numerous research groups around the world.

The exact mechanism behind CMR differs from GMR and is still not well understood, but several theories have been proposed to explain this phenomenon. They include the double exchange mechanism, a Jahn-Teller effect, the critical scattering mechanism, the percolation model, spatial electronic phase separation and the localization model [96, 192, 194].

The ability of certain materials to exhibit a large change in electrical resistance in the presence of the magnetic field at room temperature opens up a realm of possibilities for technological advancements. From magnetic memory and recording devices [6, 189, 194] to magnetic sensors [195] and spintronics [191], the applications of CMR are huge and promising.

3.2.4 Spin Hall Magnetoresistance

Spin Hall magnetoresistance (SMR) is a cutting-edge topic in spintronics research, with significant potential for advance spin-based electronic devices and systems. The concept of SMR was first introduced during the observation of the changes in resistance in a bilayer composed of a normal metal with strong spin-orbit coupling (SOC) and a ferromagnetic insulator. This discovery revealed that the electrical resistivity of the system can depend directly on the magnetization direction in the insulator [196–198].

The underlying mechanism of SMR involves the interaction between two key effects – the spin Hall effect (SHE) and inverse spin Hall effect (ISHE) [94, 95, 199]. When the electric current is applied in the plane of material with the strong SOC connected with ferromagnet (or magnetic insulator), due to SHE a transverse spin current is generated. This spin current is detected via ISHE and aligns with the magnetization of a ferromagnetic layer (Figs. 3.6(a)-(b)). This affects the electrical resistivity that manifests SMR, which depends on the angle between the spin polarization and the magnetization direction. The last one can be controlled by the applied magnetic field.

SMR was observed in a variety of materials and systems. They include heavy metals with ferromagnetic bilayers, TIs interfaced with magnetic materials (Fig. 3.6(c)), oxide heterostructures combined with ferromagnetic layers, graphene and other 2D materials doped on ferromagnetic layers [42, 94, 200, 201].

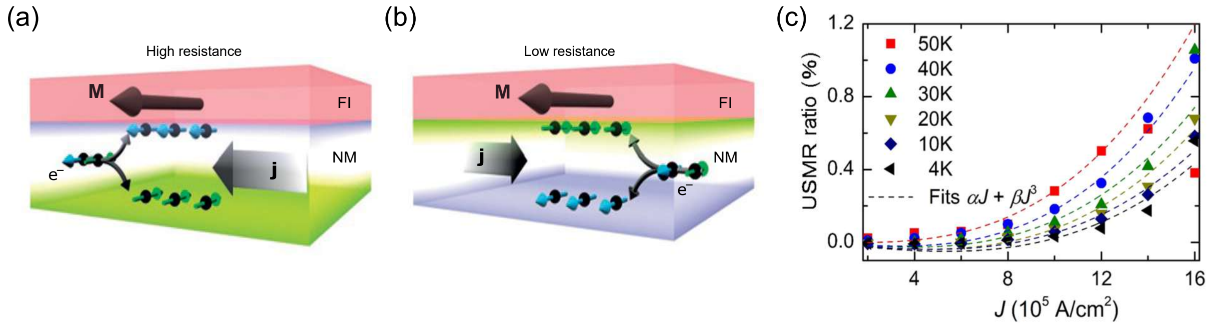

Figure 3.6: Illustration of the SMR effect. (a) Parallel alignment of the magnetization of the ferromagnetic insulator (FI) with the polarization of the spin current increases the electrical resistivity of the bilayer. (b) Antiparallel alignment decreases the electrical resistivity. The arrows in (a), (b) indicate the direction of the spin magnetic moment. NM denotes a normal metal [94]. (c) Unidirectional SMR ratio as a function of the current density J at various base temperatures T_{base} [200].

The versatile nature of SMR provides many applications in spintronics and beyond. From magnetic sensors and memory devices to spin logic and spin-based computing, SMR promises lower power consumption and higher performance. Furthermore, its possibility for the tuning and controlling makes SMR an attractive candidate for exploring new functionalities in novel fields such as quantum information processing [201–203].

3.3 Bilinear Magnetoresistance

Bilinear magnetoresistance (BMR), also known as bilinear magnetoelectric resistance (BMER), was discovered relatively recently in the context of spintronic research. Unlike the SMR effect observed in bilayers consisting of ferromagnetic and nonmagnetic material with strong SOC, this nonlinear magnetoresistance does not require a conductive ferromagnetic layer and shows a linear response with both the applied electric and magnetic fields, hence, it is called bilinear magnetoresistance. Also, the resulting magnitude and orientation of the BMR effect is significantly affected by the alignment of the current with respect to the magnetic field and crystallographic axes [204].

BMR was reported in materials characterized by strong spin-orbit interaction [7, 8]. Unlike other MR phenomena (such as SMR etc.) that were demonstrated in multilayered systems, the BMR manifests itself within a single layer material. This effect has been detected in a 3D polar semiconductor [205], topological insulators (TIs) [8, 11, 206, 207], two-dimensional transition metal dichalcogenides (TMDCs) with spin-polarized states [208, 209] and in materials with surface or interface of two-dimensional electron gas (2DEG) with Rashba interactions [210, 211].

To understand the origins of BMR in TIs two mechanisms were proposed. One of the mechanisms relates BMR to hexagonally deformed topological surface states (TSSs) (Figs. 3.7(d)-

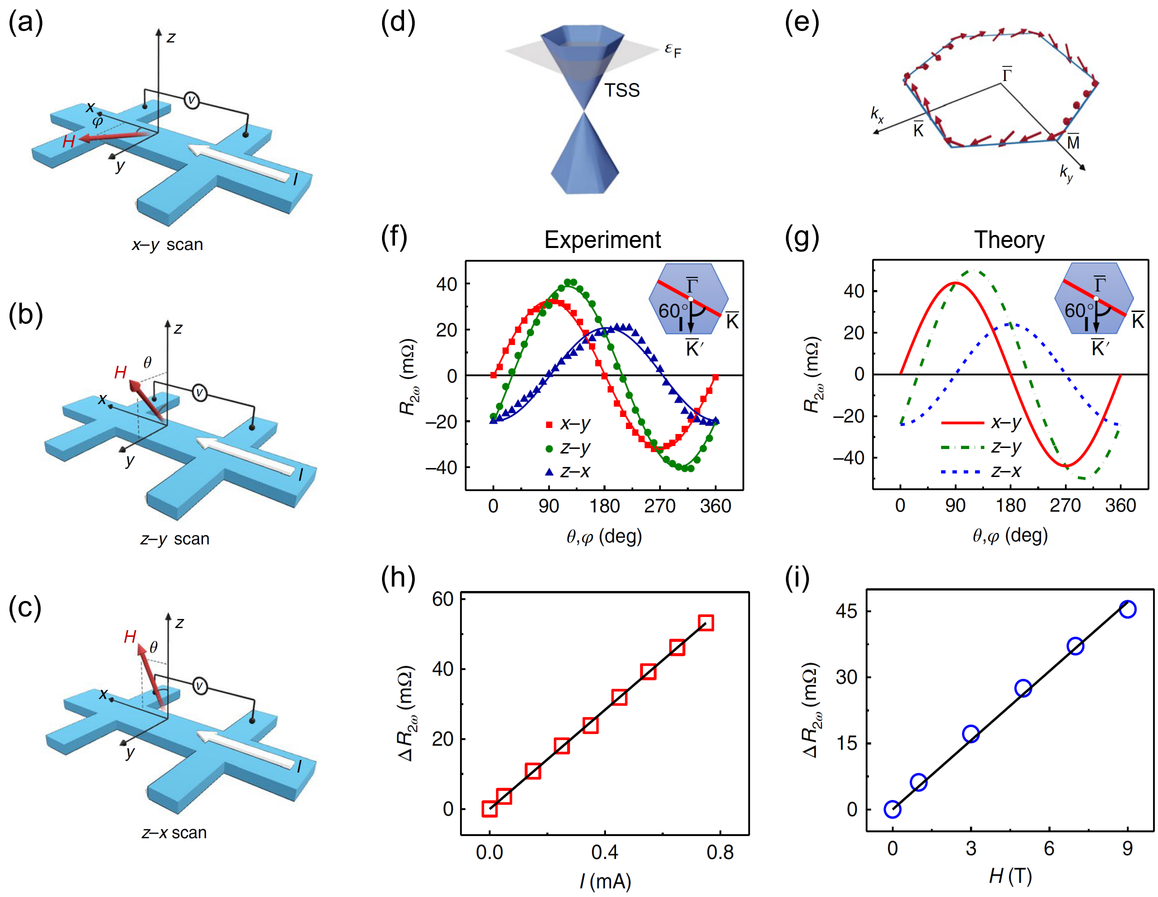

Figure 3.7: Hall bars for measurements with rotating the applied magnetic field H in the x-y (a), z-y (b) and z-x (c) planes. (d) Hexagonally warped energy dispersion for the surface states with Fermi surface lying in the conduction band. (e) Hexagonally warped spin texture at the Fermi contour of the surface states. (f) Second-harmonic resistance for all three scans for devices with current applied at an angle of $60°$ with respect to the $\bar{\Gamma}\bar{K}$ direction, respectively. The measurements were performed under $H = 9$ T, $T = 60$ K and $I = 0.55$ mA. The Fermi surface of Bi_2Se_3 is presented by the blue hexagon. The red line is along the $\bar{\Gamma}\bar{K}$ direction, and the black arrow denotes the current direction in k-space. (g) Theoretically calculated angular dependences of $R_{2\omega}$ for the three cases in (a)-(c), respectively. Parameters for calculations are $\alpha = 5 \times 10^5$ m s^{-1}, $\lambda = 165$ eV Å^3, $\varepsilon_F = 0.256$ eV, $g = 2$, $H = 9$ T, $E = 100$ V cm^{-1}, $l = 100$ μm and $w = 20$ μm. Current (h) and magnetic field (i) dependence of amplitude $\Delta R_{2\omega}$ in the z-y scan at $T = 60$ K for a device with current along $\bar{\Gamma}\bar{K}$ line. Solid black lines are fits to the data [8]. Reproduced with permission from Springer Nature.

(e)). This mechanism was used to explain the experimental observation of BMR signal measured for Bi_2Se_3 surface states, capped by MgO/Al_2O_3 [8, 204]. The measurements were performed on the Hall bar devices [212] with a rotation of the external magnetic field in different planes, as presented in Figs. 3.7(a)-(c). For scans in all three planes, the nonlinear resistance $R_{2\omega}$, shown in Fig. 3.7 (f), demonstrates sinusoidal angular dependences with a period $360°$, but with different phases in different planes. For further investigation of the physical origin of the observed magnetoresistance, it was measured the second-harmonic resistance $R_{2\omega}$ as a function of the applied magnetic field H and the current I, that is proportional to the electric field E. In

Fig. 3.7(h) it is demonstrated that the amplitude $\Delta R_{2\omega}$ of the angle-dependent $R_{2\omega}$ has a linear response on the current amplitude. And Fig. 3.7(i) presents the linear increasing of $\Delta R_{2\omega}$ with the amplitude of the applied magnetic field H and has a negligible value in the absence of the magnetic field. The linear response on both the electric and magnetic field identifies the observed magnetoresistance as bilinear. In order to show that BMR is a result of the spin-momentum locking of TSSs with hexagonal warping, it was obtained an analytical expression for $R_{2\omega}$ for model Hamiltonian of an electron in spin-momentum locked band [8]

$$H_{\mathrm{TI}} = \boldsymbol{\sigma} \cdot \left[\alpha\hbar\mathbf{k} \times \hat{\mathbf{z}} + \lambda\mathbf{k} \times \hat{\mathbf{y}}^{'} \left(k_{x'}^{2} - 3k_{y'}^{2}\right) + g\mu_B\mathbf{H}\right], \tag{3.5}$$

where $\hat{\mathbf{y}}^{'}$ and $\hat{\mathbf{z}}$ indicate the unit vectors that show the direction along $\bar{\Gamma}\bar{\mathrm{M}}$ and normal to the surface respectively, α is a Dirac velocity, $\boldsymbol{\sigma}$ denotes the Pauli matrices, and the hexagonal warping is described by the cubic term in **k** with the strength λ. The resulting expression for $R_{2\omega}$ has a form [8]

$$R_{2\omega} = E\frac{l}{w}\left(a_{\mathrm{IP}}H_y + a_{\mathrm{OP}}H_z\cos 3\phi_{\Gamma\mathrm{K}}\right), \tag{3.6}$$

where H_y and H_z are the y and z components of the magnetic field, whose directions are shown in Figs. 3.7(a)-(c), l and w are the length and width of the sample, respectively, $\phi_{\Gamma\mathrm{K}}$ is the angle between the direction of the current and the $\bar{\Gamma}\bar{\mathrm{K}}$ line with respect to the x axis (that is the direction of the electric field E), and $a_{\mathrm{IP}} = \frac{36\pi\lambda^2\varepsilon_{\mathrm{F}}g\mu_B}{e\alpha^5\hbar^4}$ and $a_{\mathrm{OP}} = \frac{6\pi\lambda g\mu_B}{e\alpha^2\hbar\varepsilon_{\mathrm{F}}}$ are the coefficients of the contributions to $R_{2\omega}$ from the in-plane and out-of-plane components of the magnetic field, respectively, with ε_{F} denoting the Fermi energy. The theoretical formula for $R_{2\omega}$ demonstrates that the second-harmonic resistance depends linearly on both the electric and magnetic fields and has perfect agreement with the experimental data, as shown in Fig. 3.7(g). Microscopically BMR is a result of the conversion of a pure spin current, induced by the second-order correction (with respect to the external electric field) to the electron distribution, into the charge current in the presence of an external in-plane magnetic field.

Another proposed mechanism of BMR in TIs can arise as a consequence of the interplay of the current-induced spin polarization and scattering in the presence of spin-momentum locking [7]. This interplay is caused by the spin-orbital structural defects, which introduce the inhomogeneities in the spin-momentum locking within the TSSs. Theoretical study of the minimal model describing surface states in TIs, taking into account the scattering term allows to write the total Hamiltonian for the system with applied electric and magnetic fields in **k** basis in a form [7]

$$H^{\mathrm{tot}}_{\mathbf{k}\mathbf{k}'} = \left(H^{0}_{\mathbf{k}} + H^{\mathbf{A}}_{\mathbf{k}}\right)\delta_{\mathbf{k}\mathbf{k}'} + V^{\mathrm{sc}}_{\mathbf{k}\mathbf{k}'}, \tag{3.7}$$

where $H^{\mathbf{A}}_{\mathbf{k}} = -e\hat{\mathbf{v}}_{\mathbf{k}} \cdot \mathbf{A}$ shows how the system interacts with the electric field (here e indicates the electron charge, $\hat{\mathbf{v}}_{\mathbf{k}} = \hbar^{-1}\nabla_{\mathbf{k}}\hat{H}^{0}_{\mathbf{k}}$ defines the velocity operator and $\mathbf{A}$ denotes the electromagnetic vector), $\hat{V}^{\mathrm{sc}}_{\mathbf{k},\mathbf{k}'}$ indicates the scattering term. $H^{0}_{\mathbf{k}} = v\left(\mathbf{k} \times \hat{\mathbf{z}}\right) \cdot \boldsymbol{\sigma} + \mathbf{B} \cdot \boldsymbol{\sigma} + \mathcal{J}\mathbf{S} \cdot \boldsymbol{\sigma}$ shows pure surface states of TIs, the influence of an applied in-plane magnetic field $\mathbf{B} = (B_x, B_y, 0)$ and also defines the effective coupling between electrons and spin polarization **S** that induced by an

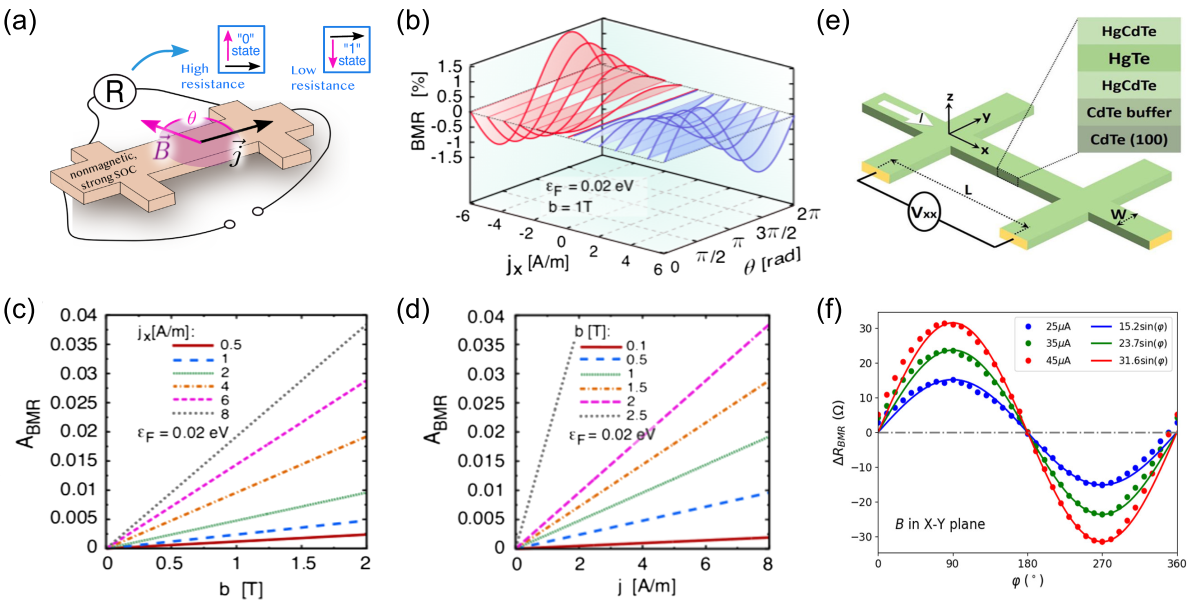

Figure 3.8: (a) Schematic picture of the system under consideration. The angle θ is defined as the angle between the orientation of charge current density j and external magnetic field b [7]. (b) BMR as a function of charge current density $j_x > 0$ and $j_x < 0$ [7]. (c)-(d) Amplitude of BMR induced by CISP A_{BMR} as a function of the applied magnetic field b (c) and current density j_x (d) [7]. (e) Schematic of Hall bars for magnetotransport measurements at 13 K with width $W = 3\ \mu$m and length $L = 15\ \mu$m. The 30 nm thick HgTe layer lies between two HgCdTe barriers. A dc current is injected along the x-axis [206]. (f) Azimuthal angular dependence of BMR at $B = 0.54$ T for different amplitudes of dc current. B field lies in x-y plane, $\varphi = 90°$ corresponding to B along y-axis, $\Delta R_{\text{BMR}} = [R(I) - R(-I)]/2$. The experimental data is presented by dots and follow a $\sin(\varphi)$ dependence that is shown by solid-lines [206].

external electric field. In this term of total Hamiltonian $v = \hbar v_{\text{F}}$ (with v_{F} denotes Fermi velocity), $\mathbf{k}$ is a wave vector, $\hat{\mathbf{z}}$ indicates the unit vector normal to the surface, $\boldsymbol{\sigma} = (\sigma_x, \sigma_y, \sigma_z)$ is the vector of Pauli matrices in the spin space, $\mathcal{J}$ is a constant describing coupling between surface states electrons and nonequilibrium spin polarization.

For the simplification, the effective field $\mathbf{B}_{\text{eff}} = \mathbf{B} + \mathcal{J}\mathbf{S}$ that makes only the shifting of the Dirac cone, can be removed from the first term of Hamiltonian (3.7) using the gauge transformation $\mathbf{k} \to \mathbf{q} - (e/\hbar)\,\boldsymbol{\Lambda}$ with $\boldsymbol{\Lambda} = (\hbar/ve)\,\mathbf{B}_{\text{eff}} \times \hat{\mathbf{z}}$. Assuming that the external electric field is oriented in the x-direction (Fig. 3.8(a)), the second term of Hamiltonian (3.7) can take the form $H^{\mathbf{A}}_{\mathbf{k}} = -e\hat{v}_{\mathbf{k}x} \cdot A_x$. After all these transformations the total Hamiltonian of the system (3.7) takes the form [7]

$$H^{\text{tot}}_{\mathbf{q}\mathbf{q}'} = \left(H^0_{\mathbf{q}} + H^{\mathbf{A}}_{\mathbf{q}}\right)\delta_{\mathbf{q}\mathbf{q}'} + V^{\text{sc}}_{\mathbf{q}\mathbf{q}'}, \tag{3.8}$$

$$H^0_{\mathbf{q}} = v\,(\mathbf{q} \times \hat{\mathbf{z}}) \cdot \boldsymbol{\sigma}, \tag{3.9}$$

$$V^{\text{sc}}_{\mathbf{q}\mathbf{q}'} = V^{i}_{\mathbf{q}\mathbf{q}'} + V^{\text{soc}}_{\mathbf{q}\mathbf{q}'}, \tag{3.10}$$

where $V^i_{\mathbf{q}\mathbf{q}'}$ is pure electrostatic potential that describes the scattering on pointlike randomly distributed defects with the assumption of the white noise distribution $\langle |V^i_{\mathbf{q}\mathbf{q}'}|^2 \rangle = n_i V_0^2$ and $V^{\text{soc}}_{\mathbf{q}\mathbf{q}'} = \frac{n_i \alpha^2}{2} \left[\left(q_y + q'_y \right) \sigma_x - \left(q_x + q'_x \right) \sigma_y \right] - \frac{n_i \alpha^2}{v} \left[B_x \sigma_x + \left(B_y + \mathcal{J} S_y \right) \sigma_y \right]$ is the part of scattering potential that shows the scattering process due to inhomogeneities of spin-momentum locking and have SOC (here n_i indicates the concentration of scattering centers, α is a parameter that defines SOC emerging from local defects distributed randomly in the structure).

In the result, the corresponding BMR can be determined as [7]

$$\text{BMR} = A_{\text{BMR}} \frac{j_x}{j} \sin\theta = 39\pi g \mu_B \frac{\hbar^2}{|e|} \frac{v_{\text{F}}}{|\varepsilon_{\text{F}}|^3} j b \frac{j_x}{j} \sin\theta, \tag{3.11}$$

where A_{BMR} is the amplitude of BMR, j_x is the density of current flowing parallel ($j_x = j$) or antiparallel ($j_x = -j$) to the x axis, ε_{F} is the Fermi energy, θ is an angle between the x axis and in-plane magnetic field with amplitude b. As shown in Fig. 3.8(b) for different values of positive and negative current density j_x, BMR changes depending on the direction of the magnetic field as $\sin\theta$. Also, in Figs. 3.8(c)-(d) it is presented the linear increasing of the amplitude of BMR with both b and j, what is the feature of the BMR effect.

For testing this theoretical model, it was made the observation of BMR in strained cubic HgTe 3D TI without hexagonal warping [206]. Magneto-transport measurements were performed at a low temperature (13 K) on a conventional Hall bar device [212] shown in Fig. 3.8(f). A dc current I is applied along the x axis together with the external magnetic filed B. BMR is derived from the measurement of the longitudinal voltage V_{xx}. Rotating the field in the x-y plane, in Fig. 3.8(e) it is demonstrated the expected angular dependence of the BMR.

Understanding the origins of BMR is crucial for potential applications in spintronics and quantum information processing [209]. Because of unique properties, BMR can be exploited in magnetic random-access memory (MRAM), spintronic devices (spin-based transistors, logic gates etc.), magnetic sensors for detection of magnetic fields or studying spin textures of novel materials via magnetotransport measurements without the fabrication of special heterostructures for spin injection or detection.

Chapter 4

Planar Hall Effect

This chapter aims to review the recent studies on the planar Hall effect (PHE). Firstly, it is important to understand the basic concepts of this intriguing phenomenon, which has demonstrated its complex and fascinating nature due to its ability to generate a measurable transverse voltage when a magnetic field is applied in the plane of a sample through which an electric current flows [9]. Then we explored the proposed microscopic mechanisms contributing to the PHE and aimed to elucidate its origins in materials, especially in topological insulators (TIs) [123]. The exploration of these mechanisms offers valuable opportunities to deepen our understanding of the complex interplay between electronic transport and magnetic properties in condensed matter systems. The investigation of the PHE holds great promise for advancing our knowledge in this field and potentially enabling the development of novel electronic devices with enhanced functionalities [213]. This effect has already found applications in various fields, including spintronics, magnetic sensing, and data storage.

4.1 Basic Concepts

The planar Hall effect (PHE) is a phenomenon that in recent times has attracted great attention due to its potential applications in various fields and has a rich history dating back to 1954 when it was first reported by Goldberg and Davis as a new galvanomagnetic effect [214]. This effect occurs when an electric current flows through the material with an applied external magnetic field. In contrast to the ordinary Hall effect (Section 2.4), which generates a voltage with electric and magnetic fields in perpendicular planes, PHE produces a voltage in response to the coplanar electric and magnetic fields (see Fig. 4.1).

PHE is driven by interactions between the electric and magnetic fields that result in the transverse voltage. But, unlike the ordinary effect, which is induced by the Lorentz force acting on moving charges, PHE should operate under entirely different principles. Therefore, various microscopic mechanisms have been proposed to describe PHE [49, 123]. This interplay between a magnetic and electric fields change the scattering process in the system, which leads to different

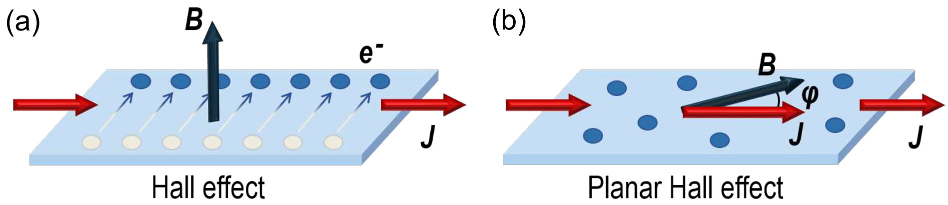

Figure 4.1: (a) Ordinary Hall effect scheme, where the black and red arrows indicate magnetic field B and current density J, respectively. The blue balls and white balls represent electrons and holes, respectively. (b) PHE scheme, with φ defined as the angle between the in-plane magnetic field and applied electric field (current density) [9]. Drawn according to the figure from Recent progress on the planar Hall effect in quantum materials, J. Zhong, J. Zhuang, Y. Du: Chin. Phys. B **32**, 047203 (2023)

resistances depending on the direction of the magnetic field – parallel (R_{xx}) or perpendicular (R_{xy}) to the current. For a two-dimensional (2D) system with an electric field, applied along x-direction, and a magnetic field, applied in the same plane, with the angle φ between them, one can find the expressions of PHE and longitudinal resistance [9]

$$R_{xx} = R_{\perp} + \left(R_{\parallel} - R_{\perp}\right)\cos^2\varphi, \tag{4.1}$$

$$R_{xy}^{\mathrm{PHE}} = \left(R_{\parallel} - R_{\perp}\right)\sin\varphi\cos\varphi. \tag{4.2}$$

From Eqs. (4.1) and (4.2) follows that the conventional PHE can be described in terms of transverse and longitudinal resistance, exhibiting a periodicity of π [123]. However, certain materials have displayed an unconventional PHE [121, 215], characterized by the periodicity of 2π and $\pi/2$. To provide insights into the underlying microscopic mechanisms responsible for these cases, various explanations have been proposed in addition to the existing understanding of PHE. For example, the conversion of a nonequilibrium spin current into a charge current explains the periodicity of 2π [11]. In turn, the $\pi/2$-periodic PHE originates from the orbital magnetic moments (OMMs) of bulk Dirac electrons [216].

PHE can manifest itself differently in various materials, depending on their specific characteristics [217–219]. For example, in some materials, the deflection of charge carriers may be linearly proportional to the magnetic field strength, while in others, it may exhibit a nonlinear relationship. Additionally, the presence of impurities, crystal structure, and electron-electron interactions can influence the behavior of PHE in a given material. PHE has been observed in ferromagnetic materials [220, 221], topological superconductors [132, 222], nonmagnetic materials [223], especially topological materials such as Dirac [224, 225] and Weyl semimetals [113, 226, 227] and topological insulators (TIs) [120, 228–230].

The broad range of materials and structures highlights the potential for PHE to be utilized in different technological advancements. One of the key advantages of this effect is its sensitivity to the orientation of the magnetic field. By measuring the transverse voltage, one can determine the magnitude and direction of the magnetic field with high precision. This makes PHE a valuable tool for magnetic field mapping and characterization. In addition, this effect has been a widely studied in the field of Hall sensors [213]. Its relevance in magnetic random

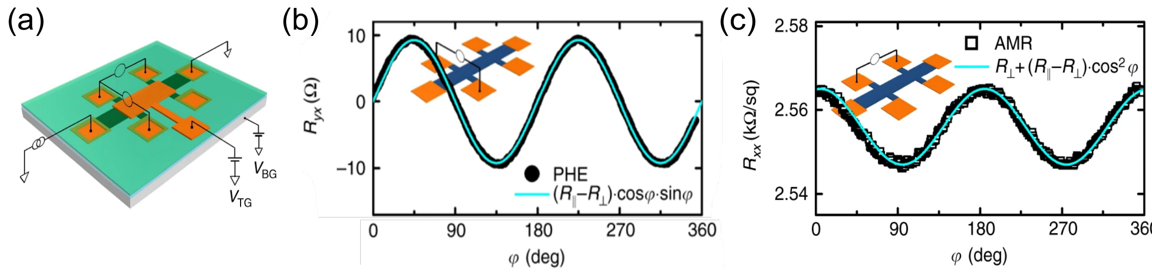

Figure 4.2: (a) Schematic of the dual-gate Hall-bar device and the measurement configuration. Angle-dependent (b) PHE R_{yx} and (c) AMR R_{xx} measurement in TI thin film $Bi_{2-x}Sb_xTe_3$ [10].

access memory (MRAM) devices has also gained recognition for its potential in memory storage applications [123, 213]. Also, there are many distorted PHE results, providing additional means to detect hidden information such as spins, SOC, symmetry of the crystal, and so on. PHE can operate at room temperature, eliminating the need for cooling systems and making it more cost-effective [131, 207].

4.2 Experimental Observations

Experimental studies of PHE in topological insulators (TIs) have demonstrated that, due to the intriguing properties of TIs, many different mechanisms can be involved in PHE.

By magnetotransport measurements in devices based on TIs it was shown that PHE vanishes in materials without the topological surface states (TSSs) [134, 135]. Furthermore, to investigate the microscopy of PHE, experiments were evaluated in various conditions and addressed to different mechanisms – from the anisotropic lifting of topological protection of the surface states [10] and resistivity anisotropy [132] to the bulk contribution [123] and others [122, 125].

The most remarkable experiment shows PHE, which is a response to anisotropic backscattering induced by an in-plane magnetic field [10]. Observations were made on dual-gated devices consisting of bulk-insulating $Bi_{2-x}Sb_xTe_3$ (BST) thin films grown on sapphire substrates using the molecular beam epitaxy (MBE) technique. [231] The dual-gate device [212], shown in Fig. 4.2(a), allows precise control over the charge carrier density on both surfaces, resulting in the high resistance and the Dirac-point crossing of the Fermi level.

The results of the experiment reveal that the backscattering of Dirac fermions on the TI surface is forbidden in zero field due to spin-momentum locking. But when time-reversal symmetry (TRS) becomes broken by the in-plane magnetic field [9], the topological protection [122] is selectively lifted. It leads to a magnetic field-induced anisotropy in the electrical resistivity measured along and perpendicularly to the field, which results in PHE and the anisotropic magnetoresistance (AMR) (Section 3.2.2). The planar Hall resistance (R_{yx}) is measured across the width of the sample, perpendicular to the direction of the electric current. It shows the $\sim \cos\varphi \sin\varphi$ angular dependence, as illustrated in the Fig. 4.2(b). Additionally, there is ob-

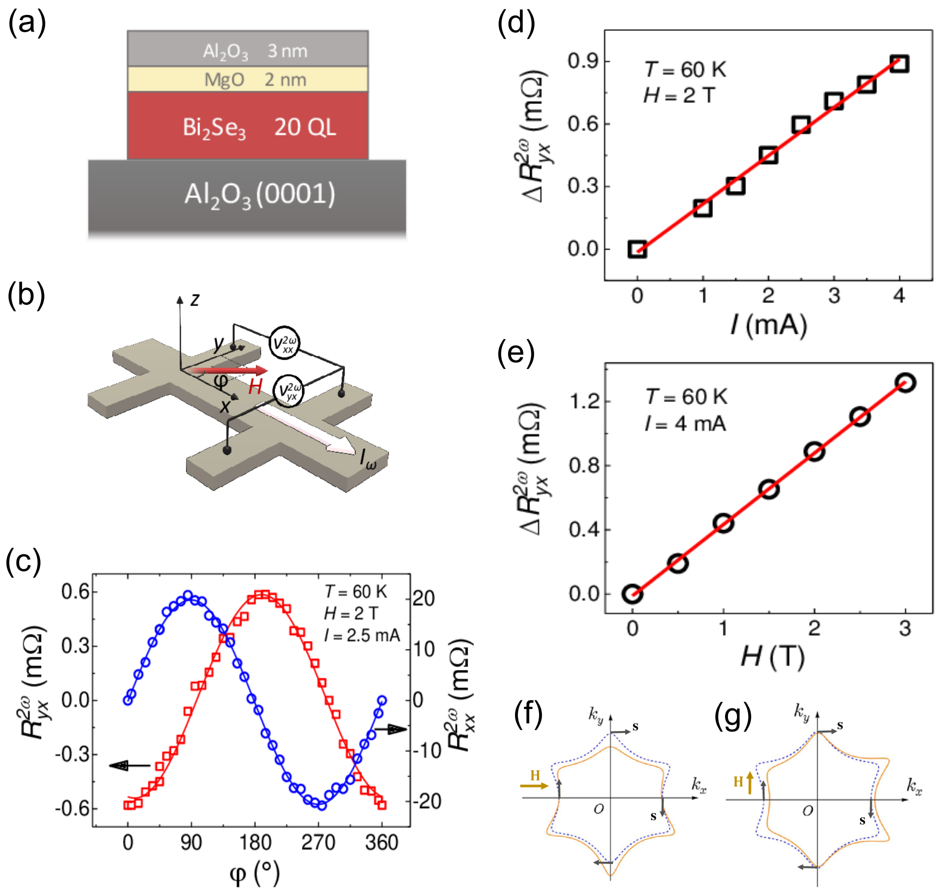

Figure 4.3: (a) Schematic illustration of the sample structure. (b) Schematic illustration of the simultaneous measurements of nonlinear PHE ($V_{yx}^{2\omega}$) and nonlinear magnetoresistance ($V_{xx}^{2\omega}$). (c) Comparison of the angular dependence of $R_{yx}^{2\omega}$ and $R_{xx}^{2\omega}$ while rotating H in plane in a Bi_2Se_3 film. A linear dependence of the sinusoidal amplitude $\Delta R_{yx}^{2\omega}$ on the current I (d) and magnetic field H (e). The solid lines are linear fits. An asymmetric distortion of the Fermi contour when H is aligned in the x-direction (f) and when H is aligned in the y-direction (g). The blue (yellow) curves show the schematic Fermi contours of the surface band under a zero (nonzero) external magnetic field. The black arrows indicate the spin directions of the four typical TSSs [11].

served the longitudinal resistance (R_{xx}) with a $180°$ periodic angular dependence, described by $\sim \cos^2(2\varphi)$, and called the anisotropic magnetoresistance (AMR), shown in Fig. 4.2(c).

Experimental studies have played a crucial role in unraveling the nonlinear PHE in TIs [134, 232]. PHE is nonlinear if it has nonlinear behavior with respect to the applied electric field. By employing different measurement techniques, it was observed that PHE in a nonlinear regime arises from the topological surface band structure of the material [8, 93, 233] as a second-order response to the external electric field. These observations have provided insights into the potential microscopic mechanisms that contribute to this phenomenon, such as the asymmetric scattering of surface electrons by magnons [234], hexagonal warping by the external magnetic field [11], Berry curvature and chiral anomaly [235], lifting of the Dirac dispersion enhanced by scattering off non-magnetic impurities [207] and many others.

One of the prominent experiments demonstrates that the nonlinear PHE can be attributed to the conversion of a transverse nonlinear spin current to a nonlinear charge Hall current through the application of an in-plane magnetic field. To conduct the experiment, it was grown high-quality Bi_2Se_3 films on Al_2O_3 (0001) substrates utilizing a sophisticated MBE system. In order to protect the Bi_2Se_3 films, a layer of MgO/Al_2O_3 was deposited on top of them, as depicted in Fig. 4.3(a). As a result, it was fabricated the Hall bar device [212], shown in Fig. 4.3(b) [11]. To detect the nonlinear PHE in a Bi_2Se_3 film, there was utilized the second harmonic Hall voltage technique with an external magnetic field in the film plane forming an angle φ with the longitudinal current, as illustrated in Fig. 4.3(b). For a specific current I and magnetic field H, the second harmonic resistance $R_{yx}^{2\omega}$ $\left(\equiv V_{yx}^{2\omega}/I\right)$ was measured. This experiment demonstrates a cosine angular dependence as shown in Fig. 4.3(c). Also, $R_{yx}^{2\omega}$ was measured for varying magnitudes of I and H, as demonstrated in Figs. 4.3(d)-(e). The observed nonlinear Hall effect in Bi_2Se_3 films adopts the form of $R_{yx}^{2\omega} \approx \mathbf{E} \cdot \mathbf{H}$, indicating the nonlinear nature of $R_{yx}^{2\omega}$ (**E** represents the applied electric field and **H** denotes the magnetic field applied in the plane of the films). Further in the same Hall bar [212], shown in Fig. 4.3(b), it was measured the longitudinal resistance $R_{xx}^{2\omega}$ – the bilinear magnetoresistance (BMR) [8, 211] (Section 3.3). This resistance also exhibits a linear scaling dependence on both the electric and magnetic fields. A detailed analysis of angular dependence of the two nonlinear resistances depicted in Fig. 4.3(c) uncovers a significant shift on the $90°$ angle, in contrast to the ordinary distinction on $45°$ angle that can be observed between conventional PHE and the longitudinal AMR in thin films of TIs [10] when the external magnetic field is rotated in the plane of the film. The presence of a $90°$ angle discrepancy is a result of the different reactions of the surface states electrons to the applied electric and magnetic fields. While the deformation of the Fermi contour, in response to the second order of the electric field, is symmetrical in **k** space, it becomes asymmetrical with an applied magnetic field. As presented in the Figs. 4.3(f)-(g), the Fermi contour becomes asymmetrically deformed in the y-direction with an applied magnetic field in the x-direction. This is the result of the action of two effects – spin-momentum locking [7] and the hexagonal warping effect [8]. Moreover, it manifests itself in the form of nonlinear transport phenomena, namely, the nonlinear PHE and the BMR effect.

4.3 Microscopic Mechanisms

Despite the experimental confirmation, the microscopic mechanisms responsible for PHE in TIs remain enigmatic. There are ongoing investigations of various hypotheses to shed light on these mechanisms. Some proposed mechanisms include the interplay between surface states and bulk bands, spin-orbit coupling effects, and the influence of magnetic impurities.

For instance, it was proposed a model of electron scattering off magnetic impurities polarized by an in-plane magnetic field [10]. And here the magnetization of the scatterers is essential which can be explained by how the anisotropic backscattering is induced by magnetic disorders. The details and experimental observations for this model were presented in the previous section. However, there was shown that the anisotropic backscattering leading to PHE, is a result of tilting of the Dirac cone [228] by an in-plane magnetic field, regardless of the magnetic properties of the scatterers. Also, it was analyzed the role of the nontrivial Berry curvature in the conduction band [236] in the emergence and manifestation of the planar Hall response. It was shown that such a phenomenon exists in TIs even in the absence of chiral anomaly and, additionally, the orbital magnetic moments (OMMs) enhance the magnitude of the planar Hall conductivity. Recently, it has been shown that the phenomenon of PHE can be attributed to the presence of spin-momentum locking surface states in TIs [10, 122]. Furthermore, PHE can originate from the dominant bulk contribution [123]. This assertion is justified by the noticeable augmentation of PHE signal within temperature in thicker devices.

The nonlinear PHE is a quite new phenomenon that still needs detailed study. Theoretical models are mostly developed to explain experimental data. The nonlinear PHE due to the conversion of a nonlinear transverse spin current to a charge current [11] was discussed in the previous section. Also, an asymmetric magnon scattering model [234] allows to evaluate a transverse resistance in magnetic TIs under certain configurations. In the case of the combination of TIs with magnetic insulators, it has been verified that the presence of backscattering due to out-of-plane spin texture formation, can lead to an enhancement in the nonlinear spin-to-charge conversion, thereby giving rise to the nonlinear PHE [207]. It was also found that the opening of the gap caused by the exchange interaction plays the necessary role in generation of the nonlinear PHE. In addition, some theories focus attention on analyzing the interplay of current-induced spin polarization (CISP) and scattering processes, which are caused by the inhomogeneities of spin-momentum locking [7]. These inhomogeneities arise as a consequence of structural defects present in TIs. The proposed mechanism, derived from this model, results in the occurrence of nonlinear PHE, even when the electronic band structure is isotropic. Besides, two extra mechanisms related to the nonlinear PHE [133] were proposed. The first mechanism, referred to as the tilt effect, is attributed to the tilting of the Dirac cones in response to an in-plane magnetic field, which leads to anisotropic backscattering caused by the distortion of the spin texture of the surface states. The second mechanism, known as the relative shift effect, arises from the presence of a nonzero net spin polarization. Remarkably, it was found that PHE can emerge on the surfaces of TIs even in the absence of magnetic impurities.

Chapter 5

Green's Functions and Diagrammatic Technique

This chapter discusses the basics and application of the most well-known and universal approaches to theoretical calculations – Green functions and diagrammatic techniques. It explores the mathematical formalism of Green's functions, figuring out their physical interpretation and their role in describing the systems. In addition, the diagrammatic technique is introduced as a graphical representation of processes in systems, emphasizing its effectiveness in theoretical calculations. These methods have important applications in fields such as condensed matter physics, quantum field theory, and statistical mechanics.

5.1 Introduction

A system consisting of numerous interacting particles inherently exhibits a rather complex and multifaceted level of behavior. The spectrum of energy levels associated with such a system is characterized by an almost continuous range, and the eigenfunctions that correspond to these energy levels are intricate mathematical representations that depend on the spatial coordinates of the individual particles. The precise formulation of the energy spectrum and the corresponding wave functions remains unknown, as it is neither fully calculable nor readily measurable. The most comprehensive understanding of a many-particle system can be achieved by solving the Schrödinger equation. Nevertheless, obtaining an accurate solution to the Schrödinger equation is an attempt that turns out to be impossible in most cases, which leads to an appeal to various approximation methods based on perturbation theory, which are used both for theoretical calculations and for experimental analysis. In the context of a typical experimental measurement that investigates a many-particle system, one often observes the cases when a system, that is already in equilibrium, is subjected to weak perturbation using one or more methods: for example, adding or removing a particle, applying a weak electromagnetic field, interacting a beam of electrons or neutrons that strike the system, or setting a thermal gradient across the system, and others. Rather than trying to compute the full energy spectrum of a many-particle system, it is more advantageous to focus on understanding the system's response to such external perturbations and influences. The most effective methodology to achieve this understanding involves the application of Green functions, as well as the use of Feynman diagrams, which serve as powerful tools for visualizing and calculating the impact of these perturbations on the many-particle system under investigation [237, 238].

5.2 Green's Functions at Zero Temperature

Many-body calculations are often carried out for simplified model systems that are specifically analyzed at absolute zero temperature, which serves as a theoretical limit that helps to understand complex interactions in different systems. It is important to admit that real experimental systems, in practice, are never really at zero temperature; however, they often operate under conditions that can be considered low temperature. It is noteworthy that many physical quantities demonstrate a remarkable insensitivity to temperature changes, especially when it comes to low temperature scenarios, which allows for certain simplifications in the analysis. Despite the apparent gap between zero temperature estimation and actual physical systems, these theoretical calculations prove to be quite useful in providing insights that relate to the real scenarios being studied. Moreover, the characteristics of a system at zero temperature are recognized as an essential quantity that determines the ground state of the interacting system, which is fundamental to understanding its properties. Generally, a system is described by its ground state along with its excitations, and the ground state can often be derived from exact zero-temperature calculations [237, 238]. A significant number of zero temperature calculations have been performed to establish, for example, the ground state of a homogeneous electron gas or to elucidate the ground state characteristics of superfluid He^4 [239–241]. Thus, zero temperature formalism arises as an indispensable component of computational strategies and methodologies used in theoretical and applied physics.

It is usually necessary to solve the Hamiltonian, which is characterized by its complexity and is often unsolvable using conventional analytical methods. In scenarios where a solution can be reached in a direct way, the use of Green's functions becomes unnecessary and superfluous, since the problem can be solved without resort to such advanced mathematical constructions. It should be noted that a very limited number of accurate results were obtained using Green's functions and which were not first established using more traditional theoretical methodologies.

Typically, it is assumed that it is necessary to find out the basic properties and behavior of a particular physical system, which is described by the Hamiltonian, denoted as H, which, due to its complexity, may not have an accurate solution. This Hamiltonian can be separated into two parts [237, 239, 240]

$$H = H_0 + V, \tag{5.1}$$

where H_0 is usually selected as Hamiltonian which can be solved exactly, V denotes the rest parts of Hamiltonian H. It is good to choose H_0 in such way that influence of part V will be small. H_0 shows an unperturbed part, V indicates interactions and additional effects in the system. The procedure of calculation is started from describing the part H_0. Then, after introducing the part V, one investigates how this part changes the properties. These steps represent the basic procedure in many-body theory [240].

Next, considering an operator A

$$A(t) = e^{iHt} A e^{-iHt} \tag{5.2}$$

and in the same way an operator B, it is possible to define the real-time casual correlation function [237, 241]

$$C_{AB}\left(t, t'\right) = -i\langle TA\left(t\right)B\left(t'\right)\rangle, \tag{5.3}$$

where $\langle ... \rangle$ represents the grand canonical ensemble average, T is the time-ordering operator, and $TA\left(t\right)B\left(t'\right) = A\left(t\right)B\left(t'\right)$ for the case when $t > t'$, $TA\left(t\right)B\left(t'\right) = \mp B\left(t'\right)A\left(t\right)$, when $t < t'$ ($\mp$ refers to the case when A and B are fermion (boson) operators).

Now it is possible to define the retarded correlation function C^R [237, 239]

$$C^R_{AB}\left(t, t'\right) = -i\theta\left(t - t'\right)\langle\left[A\left(t\right)B\left(t'\right)\right]_{\pm}\rangle, \tag{5.4}$$

with upper (lower) sign refers to fermions (bosons), and $\theta\left(t - t'\right)$ denotes the step function

$$\theta\left(t - t'\right) = \begin{cases} 0, \ t < t', \\ 1, \ t > t'. \end{cases} \tag{5.5}$$

$C^R_{AB}\left(t, t'\right)$ is nonzero only in case of $t > t'$. This is the reason why it is called "retarded". A common property of correlation functions is that for case when the Hamiltonian is time-independent, they depend on $t - t'$, not on t and t' independently [237].

The real-time Green's function is a special case of correlation functions for $A = \Psi_\sigma\left(\mathbf{r}\right)$ and $B = \Psi^\dagger_\sigma\left(\mathbf{r}\right)$, where $\Psi_\sigma\left(\mathbf{r}\right)$ ($\Psi^\dagger_\sigma\left(\mathbf{r}\right)$) denotes the field operator that annihilates (creates) a particle with spin projection σ at position $\mathbf{r}$. There are different types of real-time Green's functions – casual G, retarded G^R, advanced G^A [237, 239]

$$G\left(\mathbf{r}\sigma t, \mathbf{r}'\sigma' t'\right) = -i\langle T\Psi_\sigma\left(\mathbf{r}t\right)\Psi^\dagger_\sigma\left(\mathbf{r}'t'\right)\rangle, \tag{5.6}$$

$$G^R\left(\mathbf{r}\sigma t, \mathbf{r}'\sigma' t'\right) = -i\theta\left(t - t'\right)\langle|\Psi_\sigma\left(\mathbf{r}t\right)\Psi^\dagger_\sigma\left(\mathbf{r}'t'\right)|_{\pm}\rangle, \tag{5.7}$$

$$G^A\left(\mathbf{r}\sigma t, \mathbf{r}'\sigma' t'\right) = i\theta\left(t - t'\right)\langle|\Psi_\sigma\left(\mathbf{r}t\right)\Psi^\dagger_\sigma\left(\mathbf{r}'t'\right)|_{\pm}\rangle, \tag{5.8}$$

with the upper (lower) sign refers to fermions (bosons). Retarded "R" for Green's function means that the appearance of the particle at the position $\mathbf{r}$ at time t depends on its position $\mathbf{r}'$ at earlier time t', while advanced "A" causes the dependence on the presence of the particle with the position $\mathbf{r}'$ at future time t'.

Further, it will be discussed only the retarded Green's functions. They, which are the most instrumental among various types of correlation functions, serve a critical role in elucidating and quantifying the dynamic response of a physical system which is subjected to external perturbations, such as those induced by electromagnetic fields, incident electrons, or neutrons, and consequently, these functions are intrinsically linked to quantities that can be directly observed and measured through experimental methods [238, 239].

Assuming that Hamiltonian (5.1) is time-independent, the retarded Green's function is a special case of such correlation functions that depend on the difference $t - t'$, so it can be set t' to zero and then the function G^R will depend only on t.

In addition, if to consider translationally invariant systems, in which the function of positions does not change with a simultaneous spontaneous change in the positions of $\mathbf{r}$ and $\mathbf{r}'$, then Green's functions will depend on the difference in positions $\mathbf{r} - \mathbf{r}'$. Then, for the case of a translationally invariant system with a Hamiltonian independent of time, the retarded Green's function will be [237, 240, 241]

$$G^R\left(\mathbf{r} - \mathbf{r}'\sigma, t\right) = -i\theta\left(t\right)\langle|\Psi_\sigma\left(\mathbf{r}t\right)\Psi_\sigma^\dagger\left(\mathbf{r}'0\right)|_\pm\rangle. \tag{5.9}$$

For this case, after determination of a complete set of single-particle momentum states $|\mathbf{k}\sigma\rangle$ with the corresponding operators [237]

$$\Psi_\sigma\left(\mathbf{r}t\right) = \frac{1}{\sqrt{V}}\sum_{\mathbf{k}} e^{i\mathbf{k}\cdot\mathbf{r}} a_{\mathbf{k}\sigma}\left(t\right), \qquad \Psi_\sigma^\dagger\left(\mathbf{r}t\right) = \frac{1}{\sqrt{V}}\sum_{\mathbf{k}} e^{-i\mathbf{k}\cdot\mathbf{r}} a_{\mathbf{k}\sigma}^\dagger\left(t\right),$$

where $a_{\mathbf{k}\sigma}^\dagger$ ($a_{\mathbf{k}\sigma}$) is the operator that creates (annihilates) a particle in state $|\mathbf{k}\sigma\rangle$, it can be defined the spatial Fourier transform [237]

$$G^R\left(\mathbf{k}\sigma, t\right) = -i\theta\left(t\right)\langle|a_{\mathbf{k}\sigma}\left(t\right)a_{\mathbf{k}\sigma}^\dagger\left(0\right)|_\pm\rangle \tag{5.10}$$

with the correspond spectral representation [237, 239]

$$G^R\left(\mathbf{k}\sigma, \omega\right) = \int_{-\infty}^{\infty} e^{i\omega t} G^R\left(\mathbf{k}\sigma, t\right) dt. \tag{5.11}$$

Also one can generalize the definition (5.7) for the retarded real-time Green's functions. These functions can be defined via corresponding annihilation and creation operators for any complete set of single-particle states $|\psi_1\rangle$, $|\psi_2\rangle$, ... In the result, the retarded Green's function in ψ_λ-representation will be [237, 240]

$$G^R\left(\lambda, t - t'\right) = -i\theta\left(t - t'\right)\langle|c_\lambda\left(t\right)c_\lambda^\dagger\left(t'\right)|\rangle. \tag{5.12}$$

The quantum number λ can have any definition, depending on the problem under consideration. At zero temperature the state $|\rangle$ is defined as the ground state. Since it is chosen that the problem is described by the Hamiltonian H (5.1), and therefore $|\rangle$ denotes the ground state of this Hamiltonian, whence it follows that $|\rangle$ is the eigenstate of the Hamiltonian H. Certainly, at the beginning, neither the ground state nor the other eigenstates of the problem's Hamiltonian H are known, since this is the final task to be solved by using Green's functions. Having written the Hamiltonian H (5.1) in two parts, the unperturbed part H_0 should be chosen so that its eigenstates are known. As noted, c_λ is defined through terms of a complete set of states ψ_λ. Next, this set of states is chosen as the eigenstates of the unperturbed Hamiltonian H_0. Then, in the final definition of the Green's function, c_λ is responsible for the states of the unperturbed Hamiltonian H_0, and the ground state $|\rangle$ represents an eigenstate of the complete Hamiltonian H [240].

To solve the problem under consideration, there may be needed a special case of the Green's function, when the interaction part of Hamiltonian (5.1) $V = 0$. This case corresponds to the unperturbed Green's function, or free propagator [240]

$$G^0 \left(\lambda, t-t'\right) = -i\theta \left(t-t'\right) \ {}_0\langle| c_\lambda \left(t\right) c_\lambda^\dagger \left(t'\right) |\rangle_0, \tag{5.13}$$

where $|\rangle_0$ is a ground state of the unperturbed Hamiltonian H_0.

Any (casual, retarded or advanced) full Green's function of the system with taking into account all necessary perturbations can be found from so-called Dyson's equation, that in general has a form [239, 240]

$$G = G^0 + G^0 V G. \tag{5.14}$$

For this equation, there can be made a lot of different modifications, depending on the problem under consideration. In addition, for ease of understanding the system, the Dyson's equation can be rewritten as Feynman diagrams and can be used not only for the full Green's function, but also for any others needed for calculations.

5.3 Linear Response Theory

Linear response theory is a deeply significant and widely used basis in all fields of physics, demonstrating its universality and applicability in many contexts. This fundamental principle states that the reaction or response of the system to a slight external perturbation is directly proportional to the magnitude of this perturbation, thereby indicating that the main focus of the study should be on determining the constant that defines this proportional relationship. Among the many potential applications that can be derived from the linear response formula, one can especially highlight the charge and spin susceptibility observed in various electronic systems during the action of external electric or magnetic fields. In addition, it can be used to calculate the responses of materials to external mechanical forces or vibration [237].

At the beginning, one considers a quantum system that is described by the unperturbed time-independent Hamiltonian H_0 in thermodynamic equilibrium. Then, it is assumed that an external perturbation is applied to the system at some point in time $t = t_0$, what brings the system out of equilibrium. To describe this perturbation, one needs to add additional term that depends on time

$$H = H_0 + H'(t)\,\theta(t - t_0)\,. \tag{5.15}$$

The main goal of calculations is to find an expectation value of a physical quantity, described by the operator A at the time t, greater then t_0. For this, it is needed to find the time evolution of the density matrix or the time evolution of eigenstates of the unperturbed time-independent Hamiltonian H_0, that describes the system before perturbation. If to take H' as a small perturbation, the result is the expectation value of A up to linear order of the perturbation, that gives the retarded correlation function or retarded response function [239]

$$\delta\langle A(t)\rangle \equiv \langle A(t)\rangle - \langle A\rangle_0 \int_{t_0}^{\infty} dt' C^R_{AH'}(t, t')\,, \tag{5.16}$$

where

$$C^R_{AH'}(t, t') = -i\theta(t - t')\,\langle[A(t)\,H'(t')]\rangle_0. \tag{5.17}$$

This is the Kubo formula, which describe the linear response to a perturbation H' [237, 239].

5.4 Feynman Diagram Technique

From the linear response theory and method of Green's functions, it becomes apparent that carrying out complete calculations of phenomena in the quantum field theory is an extremely difficult task. Even the basic operators can manifest as an infinite series of terms for all orders in relation to the perturbations in the system. Consequently, it becomes challenging to choose which terms are important. In 1948, Feynman solved this problem with the idea of representing all terms in the form of drawings. These drawings, called Feynman diagrams, are an accurate mathematical representation of perturbation theory in infinite order and are extremely useful in clarifying the physical processes that these terms represent. Diagrams can be drawn for both Green's function depending on time and Green's function after Fourier transformation that depends on the frequency or energy [239, 240].

The first step in drawing diagrams is to choose a so-called graphical vocabulary, that is, it is necessary to determine how to designate basic quantities – Green's functions, interactions V and effects. For example, the full Green's function of the system can be shown by two solid lines as in Fig. 5.1(a), while the unperturbed Green's function can be denoted by one solid line with an arrow indicating the direction of change in the system, as presented in Fig. 5.1(b). Then, add lines of interactions, perturbations or other additional effects, showing them with dashed lines. (Fig. 5.1(c)) It can be, for instance, scattering processes in the system. Next, determine what information should be invested in the connection points (vertex) of the lines of Green's functions. For example, it can be conservation of energy or momentum. The next step is to carry out sums for all necessary values, such as momentum, energy or spin.

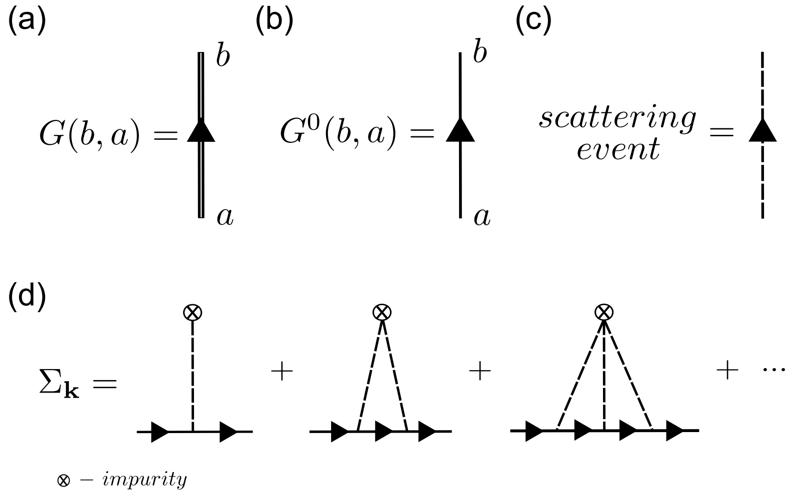

Figure 5.1: Feynman diagrams. (a) Full Green's function of the system. (b) Unperturbed Green's function. In (a) and (b) a is a point of the beginning of an effect (for example, the creation of a particle), b is a point of the ending of an effect (for instance, the annihilation of a particle). (c) Scattering process (perturbation). (d) Self-energy diagrams for scattering from a single impurity [239, 240]. Drawn according to figures from Many-Body Quantum Theory in Condensed Matter Physics, H. Bruus, K. Flensberg, (2004) and Many-Particle Physics (Second Edition), G. D. Mahan, (2000).

Impurity Self-Averaging and Self-Energy

For simplification and reduction of fluctuations, in the system with scattering on randomly positioned impurities, for which the coherent length between impurities is significantly smaller than the size of the sample in the system at all experimentally realized temperatures, it can be made a certain averaging on these impurities as on the subsystems. This averaging is defined by the physical properties of the system itself, therefore this effective averaging is considered as self-averaging and is called impurity self-averaging. Mathematically, this averaging is carried out through summation over all subsystems, then divided by the number of these subsystems. However, taking into account random distribution of impurities, this average corresponds to the average over the impurity position in one subsystem. Nevertheless, considering that the system is homogeneous, one can carry out an averaging procedure that incorporates all uncorrelated positions of the number of impurities distributed throughout the entirety of the system, and introduce the impurity averaged Green's function $\langle G_{\mathbf{k}} \rangle_{\text{imp}}$ with momentum $\mathbf{k}$ [239].

This impurity averaged Green's function can be determined using Dyson's equation. However, deriving this equation is quite complex, involving many steps and the application of various theorems. To simplify the process, the concept of self-energy $\Sigma_{\mathbf{k}}$ is introduced. With this approach, Dyson's equation for the impurity averaged Green's function can be expressed in the form [239, 240]

$$\langle G_{\mathbf{k}} \rangle_{\text{imp}} = \frac{1}{(G^0_{\mathbf{k}})^{-1} - \Sigma_{\mathbf{k}}}. \tag{5.18}$$

This equation also shows why $\Sigma_{\mathbf{k}}$ is called "self-energy". It can be considered as an additive correction to the unperturbed energy. The problem of finding a function $\langle G_{\mathbf{k}} \rangle_{\text{imp}}$ has been reduced to calculating only the self-energy, what will be correct only in the limit of low impurity concentration.

Self-energy is defined as the sum of an infinite series of different diagrams. This method is best used in the case when the approximations of the lowest terms can be enough for the final result. As an alternative, there are instances in which it becomes possible to create specific subsets of diagrams from the extensive series, thereby simplifying the computational process. Nevertheless, except for a limited number of some cases, achieving an exact value for $\Sigma_{\mathbf{k}}$ remains impossible, therefore it is necessary to accept approximate results [239]. It is essential to understand that Dyson's equation gives good insights typically only within the weak coupling theory, where the involved perturbation is small enough to get an approximation with just a few terms from $\Sigma_{\mathbf{k}}$ [240].

For the case of scattering from a single impurity with the low density concentration, the diagrams of the self-energy can be depicted as in the Fig. 5.1(d). Each of the diagrams represents its own level of approximation. The lowest order of the approximation is obtained from the first diagram from Fig. 5.1(d) and gives the contribution [239, 240]

$$\Sigma_{\mathbf{k}}^{1} = n_i \int d\mathbf{r} V\left(\mathbf{r}\right) = n_i V\left(0\right), \tag{5.19}$$

where n_i denotes impurity densities. This approximation only shows a simple constant shift of all energy levels with magnitude $n_i V\left(0\right)$.

Further, the second diagram in Fig. 5.1(d), called the "wigwam" diagram, corresponds to the first non-trivial approximation of the self-energy, which is called the first-order Born approximation [239, 240]

$$\Sigma_{\mathbf{k}}^{2} = n_i \int \frac{d^3k'}{\left(2\pi\right)^3} V\left(\mathbf{k}-\mathbf{k}'\right) G_{\mathbf{k}'}^{0} V\left(\mathbf{k}'-\mathbf{k}\right). \tag{5.20}$$

This result is obtained not just from an assumption, but comes directly from the expansion of the Green's function.

An extension of the first-order Born approximation is the full Born approximation, which is determined by the self-energy, that takes into account any number of scattering on the same impurity, that is, more dashed lines on the "wigwam" diagram with such an n-th term [240]

$$\begin{aligned}\Sigma_{\mathbf{k}}^{n} &= n_i \times \\ &\times \int \frac{d^3k_1}{\left(2\pi\right)^3} \cdots \frac{d^3k_n}{\left(2\pi\right)^3} V\left(\mathbf{k}-\mathbf{k}_1\right) G_{\mathbf{k}_1}^{0} V\left(\mathbf{k}_1-\mathbf{k}_2\right) \ldots V\left(\mathbf{k}_{n-1}-\mathbf{k}_n\right) G_{\mathbf{k}_n}^{0} V\left(\mathbf{k}_n-\mathbf{k}\right).\end{aligned} \tag{5.21}$$

From the n-th term, it can be seen that the obtained total self-energy will be proportional to the concentration n_i.

Also, for the accuracy of calculations, additional approaches and approximations can be used along with their combinations. For example, one can create a set of diagrams called the vertex correction [240]. This set will contain additional, extended information about the perturbations in the system. The vertex correction function can be found from the vertex equation. Since this equation is self-consistent, one can gradually increase the order of diagrams that are taken into account in the calculations. This approach can greatly facilitate the solution of the problem under consideration [239].

Another notable example is the ladder diagrams approach [240]. Most often, such diagrams represent a gradual increase in the number of perturbations. Ladder diagrams usually appear in higher orders of perturbation theory. Unfortunately, it is necessary to investigate each term-diagram because the high order of diagram does not necessarily have less influence than from the low-order diagrams [239].

These approaches can be applied both to finding the full Green's function and the self-energy of the system, and to calculating various required quantities, such as polarization, conductivity, etc [239, 240].

Chapter 6

Bilinear Magnetoresistance and Nonlinear Planar Hall Effect in Topological Insulators with Isotropic Fermi Contours

In this chapter, we focus on the unidirectional magnetotransport of surface electrons in a three-dimensional (3D) topological insulator (TI) with isotropic Fermi contour (without hexagonal warping, tilting, or particle-hole asymmetry), especially on the bilinear magnetoresistance (BMR) and nonlinear planar Hall effect (NPHE). We study another physical mechanism of BMR and NPHE related to scattering processes on spin-orbital impurities. Using the Green's function formalism and diagramatic method, discussed in Chapter 5, we have derived analytical results for diagonal and off-diagonal elements of the conductivities and determined nonlinear signals in two levels of the approximation [242, 243]. Both of these remarkable phenomena, which exhibit intriguing characteristics and behaviors, can be measured during one transport experiment and can be a highly effective instrument for the evaluation of material constants.

The content of this chapter is based on the original results that have been published in two articles [242, 243].

6.1 Model and Method

We consider electronic surface states of 3D topological insulator (TI) (Section 2.1) with applied in-plane external electric and magnetic fields. This system is described by a minimal model, which means that we neglect the effect of hexagonal warping, bands tilting, and electron-hole asymmetry, since they are not related to the mechanism that we propose for the bilinear magnetotransport. In addition, we make the assumption that TI is thick enough to neglect the hybridization between top and bottom surface states [242, 243].

Strong spin-orbit interaction (Section 2.2) in TIs is responsible for the so-called spin-momentum locking of surface electrons, that was introduced in Section 2.1. As a result, the net spin polarization in the electron subsystem is zero in equilibrium. However, under an external electric field, the Fermi contour is shifted in the momentum space, and a nonzero charge current and spin polarization of the conduction electrons appear. Accordingly, the current-induced spin polarization (CISP) (Section 2.3) is oriented in the plane of the system and perpendicular to the orientation of charge current density. This nonequilibrium spin polarization acts as an effective spin-orbital (SO) field [7] $\mathbf{B}_{\text{SO}} = \mathcal{J}\mathbf{S}$ with $\mathcal{J} = -8\pi v_{\text{F}}/k_{\text{F}}$ being the effective coupling between surface electrons and nonequilibrium spin polarization (v_{F} and k_{F} are Fermi velocity and Fermi wavevector, respectively). This SO field can be added to the external in-plane magnetic field, $\mathbf{B} = (B_x, B_y, 0) = B(\cos\theta, \sin\theta, 0)$ (here θ is an angle between the x-axis and orientation of magnetic field, and $B = g\mu_B\mathbf{b}$ is the magnetic field amplitude given in the energy units, i.e., b is given in Tesla).

6.1.1 Model Hamiltonian

The Hamiltonian describing surface electrons of 3D TI in the presence of external electric and magnetic fields can be written in the Bloch basis as follows:

$$H_{\mathbf{kk}'} = H^0_{\mathbf{k}}\delta_{\mathbf{k},\mathbf{k}'} + H^{\text{imp}}_{\mathbf{kk}'} + H^{\mathbf{A}}_{\mathbf{kk}'}, \tag{6.1}$$

where, $H^0_{\mathbf{k}}$ has the form

$$H^0_{\mathbf{k}} = v(\mathbf{k}\times\hat{\mathbf{z}})\cdot\boldsymbol{\sigma} + \mathbf{B}_{\text{eff}}\cdot\boldsymbol{\sigma}. \tag{6.2}$$

Here $v = \hbar v_{\text{F}}$, $\mathbf{k}$ is the wave vector and $\boldsymbol{\sigma} = (\sigma_x, \sigma_y, \sigma_z)$ is a vector of Pauli matrices acting in the spin space. The effective magnetic field, $\mathbf{B}_{\text{eff}}$, is a superposition of the external in-plane magnetic field and SO field due to the nonequilibrium CISP, i.e., $\mathbf{B}_{\text{eff}} = \mathbf{B} + \mathbf{B}_{\text{SO}}$. In addition, we note that formal incorporation of the SO field into Hamiltonian (6.2), and thus also calculation of the conductivity, should be done in a self-consistent way (see also Supplemental Material in Ref. [7]). However, because the effect of the SO field is a small perturbation (responsible for a small correction to the longitudinal current), cutting the self-consistent procedure on the lowest step and also keeping the expression for spin polarization in the zero magnetic field [7] is fully justified.

The second term in Eq. (6.1) describes scattering on randomly distributed point-like impurities that are also a source of SO scattering. The corresponding scattering potential is given by the expression [14, 20, 243]

$$H^{\text{imp}}_{\mathbf{kk}'} = V_{\mathbf{kk}'}\left(\sigma_0 - i\lambda\boldsymbol{\sigma}\cdot(\mathbf{k}\times\mathbf{k}')\right), \tag{6.3}$$

which contains the scalar component (proportional to the identity matrix σ_0) as well as the SO term, where λ describes the strength of spin-orbit coupling (SOC). The scattering potential is modeled here as short-range white noise disorder with only the second-order cumulant being nonzero, i.e., $\langle |V_{\mathbf{kk}'}|^2 \rangle = n_i V_0^2$ (n_i is a concentration of impurities and $\langle ... \rangle$ means the configurational average over impurities' positions).

The last term of Eq. (6.1) describes the coupling of electrons to the external electric field represented by the vector potential $\mathbf{A} = (A_x, A_y)$. This term can be simply obtained by the Peierls substitution [242,244,245]: $\mathbf{k} \to \mathbf{k} - \frac{e}{\hbar}\mathbf{A}$, i.e., $H^0_{\mathbf{k}}\delta_{\mathbf{k},\mathbf{k}'} + H^{\text{imp}}_{\mathbf{kk}'} \xrightarrow[\mathbf{k}\to\mathbf{k}-\frac{e}{\hbar}\mathbf{A}]{} H^0_{\mathbf{k}}\delta_{\mathbf{k},\mathbf{k}'} + H^{\text{imp}}_{\mathbf{kk}'} + H^{\mathbf{A}}_{\mathbf{kk}'}$, and takes the form

$$\begin{aligned} H^{\mathbf{A}}_{\mathbf{kk}'} = & \frac{e}{\hbar}A_x \left(v\,\sigma_y\delta_{\mathbf{kk}'} + i\lambda\, V_{\mathbf{kk}'}(k'_y - k_y)\sigma_z\right) \\ & -\frac{e}{\hbar}A_y \left(v\,\sigma_x\delta_{\mathbf{kk}'} + i\lambda\, V_{\mathbf{kk}'}(k'_x - k_x)\sigma_z\right). \end{aligned} \tag{6.4}$$

6.1.2 Current-Induced Spin Polarization

The nonequilibrium spin polarization, induced by electric field, applied in y-direction, [7,45,46] for the minimal model describing surface states of a TI can be found from

$$S_x = \frac{e\hbar}{2\pi}E_y \mathrm{Tr}\int \frac{d^2\mathbf{k}}{(2\pi)^2}\hat{S}_x \bar{G}^{0R}_{\mathbf{k}}(\varepsilon)\,\hat{v}_{\mathbf{k}x}\bar{G}^{0A}_{\mathbf{k}}(\varepsilon), \tag{6.5}$$

where E_y is a y-component of the electric field, $\hat{v}_{\mathbf{k}x}$ is x-component of the velocity operator that can be found as $\hat{v}_{\mathbf{k}x} = (1/\hbar)\left(d\hat{H}^0_{\mathbf{k}}/dk_x\right)$ and $\bar{G}^{0R/0A}_{\mathbf{k}}(\varepsilon)$ is the impurity-averaged retarded/advanced Green's function of the Hamiltonian (6.2) in the absence of magnetic field. The impurity-averaged retarded Green's function in the absence of magnetic field can be found from $\bar{G}^{0R}_{\mathbf{k}}(\varepsilon) = \left[(\varepsilon + i\Gamma_0)\sigma_0 - H^0_{\mathbf{k}}\right]^{-1}$ with $\Gamma_0 = \frac{1}{4}n_i V_0^2 \frac{|\varepsilon|}{v^2}$ and after algebraic transformations will have a form

$$\bar{G}^{0R}_{\mathbf{k}} = \frac{\varepsilon\sigma_0 + v\,(k_y\sigma_x - k_x\sigma_y)}{(\varepsilon - vk + i\Gamma_0)\,(\varepsilon + vk + i\Gamma_0)}. \tag{6.6}$$

Upon substituting Eq.(6.6) into Eq.(6.5) and after the integration, the spin polarization takes the form

$$S_x = \frac{e}{8\pi}E_y\frac{|\varepsilon|}{v}\tau_0, \tag{6.7}$$

where $\tau_0 = \frac{\hbar}{2\Gamma_0}$. In turn, the charge current density for the TI with zero magnetic field is given by

$$j_y = -\frac{e^2}{\hbar}\frac{|\varepsilon|}{4\pi\hbar}E_y\tau_0. \tag{6.8}$$

Combining (6.8) with (6.7) one finds the final result

$$S_x = -\frac{\hbar^2}{2ev}j_y. \tag{6.9}$$

Performing similar steps for the case when the electric current is applied in the x-direction, we get the spin polarization in the y-direction

$$S_y = \frac{\hbar^2}{2ev}j_x. \tag{6.10}$$

The vector form for the nonequilibrium spin polarization for the minimal model describing surface states of a TI takes a form

$$\mathbf{S} = -\frac{\hbar^2}{2ev}\mathbf{j} \times \hat{\mathbf{z}}, \tag{6.11}$$

where $\hat{\mathbf{z}}$ is a unit vector normal to the surface.

6.1.3 Gauge Transformation

The in-plane effective field $\mathbf{B}_{\text{eff}}$ included into the unperturbed Hamiltonian (6.2) leads only to a shift of electronic energy dispersion in the $\mathbf{k}$ space (i.e., the Dirac cone is shifted out of the Brillouin zone center in the presence of $\mathbf{B}_{\text{eff}}$). Accordingly, one can define a gauge transformation that removes the effect of in-plane effective magnetic field from Eq. (6.2): $\mathbf{k} \to \mathbf{q} + (e/\hbar)\mathbf{\Lambda}$, with $\mathbf{\Lambda} = (\hbar/ve)\mathbf{B}_{\text{eff}} \times \hat{\mathbf{z}}$. This transformation technically simplifies our further calculations, even though the scattering term, Eq. (6.3), is modified. The total Hamiltonian of the system after the above gauge transformation takes the form

$$H_{\mathbf{qq'}} = H^0_{\mathbf{q}}\delta_{\mathbf{qq'}} + H^{\text{imp}}_{\mathbf{qq'}} + H^{\mathbf{A}}_{\mathbf{qq'}} \tag{6.12}$$

with

$$H^0_{\mathbf{q}} = v(q_y\sigma_x - q_x\sigma_y), \tag{6.13}$$

$$\begin{aligned} H^{\text{imp}}_{\mathbf{qq'}} =& V_{\mathbf{qq'}}\left(\sigma_0 - i\lambda\,\mathbf{q}\times\mathbf{q'}\cdot\boldsymbol{\sigma}\right) \\ &+ i\frac{e}{\hbar}\lambda V_{\mathbf{qq'}}\mathbf{\Lambda}\times(\mathbf{q}-\mathbf{q'})\cdot\boldsymbol{\sigma}, \end{aligned} \tag{6.14}$$

$$H^{\mathbf{A}}_{\mathbf{qq'}} = -v\frac{e}{\hbar}\mathbf{A}\times\hat{\mathbf{z}}\cdot\boldsymbol{\sigma} - i\frac{e}{\hbar}\lambda V_{\mathbf{qq'}}\,\mathbf{A}\times(\mathbf{q}-\mathbf{q'})\cdot\boldsymbol{\sigma}. \tag{6.15}$$

For further calculation it is need to define also the charge current density operator that after the gauge transformation will have a form

$$\hat{\mathbf{j}}_{\mathbf{qq'}} = -\frac{\partial\hat{H}_{\mathbf{qq'}}}{\partial\mathbf{A}} \equiv e\hat{\mathbf{v}}_{\mathbf{qq'}}, \tag{6.16}$$

where $\hat{\mathbf{v}}_{\mathbf{qq'}}$ is the velocity operator which, based on Eq. (6.15), has two components

$$\hat{\mathbf{v}}_{\mathbf{qq'}} = \hat{v}^0_{\mathbf{qq'}}\delta_{\mathbf{q},\mathbf{q'}} + \hat{v}^a_{\mathbf{qq'}}, \tag{6.17}$$

$$\hat{v}^0_{\mathbf{qq'}} = -\frac{v}{\hbar}(\boldsymbol{\sigma}\times\hat{\mathbf{z}}), \tag{6.18}$$

$$\hat{v}^a_{\mathbf{qq'}} = i\,\frac{\lambda}{\hbar}\,V_{\mathbf{qq'}}\,(\mathbf{q}-\mathbf{q'})\times\boldsymbol{\sigma}. \tag{6.19}$$

The first term of the velocity operator is the ordinary part of the velocity operator, whereas the second term is the so-called anomalous velocity [57] due to SOC associated with impurities.

6.1.4 Green's Functions and Self-Energy

To find transport characteristics, it is needed to calculate the self-energy and impurity averaged Green's functions. The retarded self-energy in the Born approximation is given by the following expression

$$\Sigma^R_{\mathbf{q}}(\varepsilon) = \int \frac{d^2\mathbf{q}'}{(2\pi)^2} H^{\text{imp}}_{\mathbf{q}\mathbf{q}'}\, G^{0R}_{\mathbf{q}'}(\varepsilon)\, H^{\text{imp}}_{\mathbf{q}'\mathbf{q}}, \tag{6.20}$$

where $G^{0R}_{\mathbf{q}'}(\varepsilon)$ denotes the zero-order retarded Green's function corresponding to the Hamiltonian (6.13) after the gauge transformation. This function can be found from

$$G^{0R}_{\mathbf{q}}(\varepsilon) = \left[(\varepsilon + i0^+)\sigma_0 - H^0_{\mathbf{q}}\right]^{-1}. \tag{6.21}$$

In the result, after performing all the necessary substitutions and various calculations, the resulting zero-order retarded Green's function will have a form

$$G^{0R}_{\mathbf{q}}(\varepsilon) = g^R_{0\,\mathbf{q}}(\varepsilon)\sigma_0 + g^R_{x\,\mathbf{q}}(\varepsilon)\sigma_x + g^R_{y\,\mathbf{q}}(\varepsilon)\sigma_y, \tag{6.22}$$

where

$$g^R_{0\,\mathbf{q}}(\varepsilon) = \frac{1}{2}\,(G^{0R}_{\mathbf{q}+} + G^{0R}_{\mathbf{q}-}), \tag{6.23a}$$

$$g^R_{x\,\mathbf{q}}(\varepsilon) = \frac{q_y}{2q}\,(G^{0R}_{\mathbf{q}+} - G^{0R}_{\mathbf{q}-}), \tag{6.23b}$$

$$g^R_{y\,\mathbf{q}}(\varepsilon) = -\frac{q_x}{2q}\,(G^{0R}_{\mathbf{q}+} - G^{0R}_{\mathbf{q}-}) \tag{6.23c}$$

with $G^{0R}_{\mathbf{q}\pm}(\varepsilon) = \frac{1}{\varepsilon \mp qv + i\Gamma_0}$, $\Gamma_0 = \frac{1}{4} n_i V_0^2 \frac{|\varepsilon|}{v^2}$.

To simplify further calculations, after substitutions of Hamiltonian (6.14) and Eq. (6.22) one can rewrite self-energy (6.20) according to order of the SOC parameter λ for the electric current applied in the x-direction

$$\Sigma^R_{\mathbf{q}}(\varepsilon) = \Sigma^R_{\lambda^0\,\mathbf{q}}(\varepsilon) + \Sigma^R_{\lambda^1\,\mathbf{q}}(\varepsilon) + \Sigma^R_{\lambda^2\,\mathbf{q}}(\varepsilon), \tag{6.24}$$

where

$$\Sigma^R_{\lambda^0\,\mathbf{q}}(\varepsilon) = n_i V_0^2 \int \frac{d^2\mathbf{q}'}{(2\pi)^2} \left(g^R_{0\,\mathbf{q}'}(\varepsilon)\sigma_0 + g^R_{x\,\mathbf{q}'}(\varepsilon)\sigma_x + g^R_{y\,\mathbf{q}'}(\varepsilon)\sigma_y\right) \tag{6.25}$$

and $\Sigma^R_{\lambda^1\,\mathbf{q}}(\varepsilon)$ can be written as

$$\Sigma^R_{\lambda^1\,\mathbf{q}}(\varepsilon) = \Sigma^R_{\lambda^1_x\,\mathbf{q}}(\varepsilon)\sigma_x + \Sigma^R_{\lambda^1_y\,\mathbf{q}}(\varepsilon)\sigma_y \tag{6.26}$$

with components

$$\Sigma^R_{\lambda^1_x\,\mathbf{q}}(\varepsilon) = 2\lambda n_i V_0^2 \int \frac{d^2\mathbf{q}'}{(2\pi)^2} h_{\mathbf{q}'\mathbf{q}}\, g^R_{y\,\mathbf{q}'}(\varepsilon), \tag{6.27}$$

$$\Sigma^R_{\lambda^1_y\,\mathbf{q}}(\varepsilon) = -2\lambda n_i V_0^2 \int \frac{d^2\mathbf{q}'}{(2\pi)^2} h_{\mathbf{q}'\mathbf{q}}\, g^R_{x\,\mathbf{q}'}(\varepsilon), \tag{6.28}$$

where $h_{\mathbf{q}'\mathbf{q}} = q'_x q_y - q'_y q_x - (B_x/v)(q'_x - q_x) - ((B_y + \mathcal{J}S_y)/v)\left(q'_y - q_y\right)$.
The term of the self-energy with second-order of SOC parameter $\Sigma^R_{\lambda^2}$ has a form

$$\Sigma^R_{\lambda^2\,\mathbf{q}}(\varepsilon) = \Sigma^R_{\lambda_0^2\,\mathbf{q}}(\varepsilon)\sigma_0 + \Sigma^R_{\lambda_x^2\,\mathbf{q}}(\varepsilon)\sigma_x + \Sigma^R_{\lambda_y^2\,\mathbf{q}}(\varepsilon)\sigma_y, \tag{6.29}$$

where

$$\Sigma^R_{\lambda_0^2\,\mathbf{q}}(\varepsilon) = -\lambda^2 n_i V_0^2 \int \frac{d^2\mathbf{q}'}{(2\pi)^2} h_{\mathbf{q}\mathbf{q}'} h_{\mathbf{q}'\mathbf{q}}\, g^R_{0\,\mathbf{q}'}(\varepsilon), \tag{6.30}$$

$$\Sigma^R_{\lambda_x^2\,\mathbf{q}}(\varepsilon) = \lambda^2 n_i V_0^2 \int \frac{d^2\mathbf{q}'}{(2\pi)^2} h_{\mathbf{q}\mathbf{q}'} h_{\mathbf{q}'\mathbf{q}}\, g^R_{x\,\mathbf{q}'}(\varepsilon), \tag{6.31}$$

$$\Sigma^R_{\lambda_y^2\,\mathbf{q}}(\varepsilon) = \lambda^2 n_i V_0^2 \int \frac{d^2\mathbf{q}'}{(2\pi)^2} h_{\mathbf{q}\mathbf{q}'} h_{\mathbf{q}'\mathbf{q}}\, g^R_{y\,\mathbf{q}'}(\varepsilon). \tag{6.32}$$

After integration over $\mathbf{q}'$ components of the self energy (6.25), (6.27) and (6.30) have the following form

$$\Sigma^R_{\lambda^0\,\mathbf{q}}(\varepsilon) = -in_i V_0^2 \frac{1}{4}\frac{|\varepsilon|}{v^2}\sigma_0, \tag{6.33}$$

$$\Sigma^R_{\lambda_x^1\,\mathbf{q}}(\varepsilon) = \pm i\lambda n_i V_0^2 \frac{1}{4v^2}\frac{\varepsilon^2}{v^2}\left(vq_y - B_x\right), \tag{6.34}$$

$$\Sigma^R_{\lambda_y^1\,\mathbf{q}}(\varepsilon) = \mp i\lambda n_i V_0^2 \frac{1}{4v^2}\frac{\varepsilon^2}{v^2}\left(vq_x + (B_y + \mathcal{J}S_y)\right), \tag{6.35}$$

$$\begin{aligned}\Sigma^R_{\lambda_0^2\,\mathbf{q}}(\varepsilon) = &-i\lambda^2 n_i V_0^2 \frac{1}{8v^3}\frac{|\varepsilon|}{v}\frac{\varepsilon^2}{v^2}\left((vq_y - B_x)^2 + (vq_x + B_y + \mathcal{J}S_y)^2\right) \\ &- i\lambda^2 n_i V_0^2 \frac{1}{8v^3}\frac{|\varepsilon|}{v} 2\left(B_x q_x + (B_y + \mathcal{J}S_y)\, q_y\right)^2,\end{aligned} \tag{6.36}$$

$$\Sigma^R_{\lambda_x^2\,\mathbf{q}}(\varepsilon) = \mp i\lambda^2 n_i V_0^2 \frac{1}{4v^3}\frac{\varepsilon^2}{v^2}\left(B_x q_x + (B_y + \mathcal{J}S_y)\, q_y\right)\left(vq_x + B_y + \mathcal{J}S_y\right), \tag{6.37}$$

$$\Sigma^R_{\lambda_y^2\,\mathbf{q}}(\varepsilon) = \mp i\lambda^2 n_i V_0^2 \frac{1}{4v^3}\frac{\varepsilon^2}{v^2}\left(B_x q_x + (B_y + \mathcal{J}S_y)\, q_y\right)\left(vq_y - B_x\right). \tag{6.38}$$

Groping together all terms near each Pauli matrices allows to write (6.20) in the form

$$\Sigma^R_{\mathbf{q}}(\varepsilon) = \Sigma^R_{0\mathbf{q}}(\varepsilon)\sigma_0 + \Sigma^R_{x\mathbf{q}}(\varepsilon)\sigma_x + \Sigma^R_{y\mathbf{q}}(\varepsilon)\sigma_y. \tag{6.39}$$

As can be seen from previous calculations, coefficients $\Sigma^R_{0,x,y}$ will have the form which is dependent on the orientation of the charge current density (as it determines the orientation of CISP) that makes the self-energy (6.39) in general a function that depends on the current flow direction, and also the external magnetic field and nonequilibrium spin polarization.

After algebraic transformations for the charge current density flowing in the x-direction, one finds

$$
\begin{aligned}
\Sigma_0^R =& - i n_i V_0^2 \frac{1}{4} \frac{|\varepsilon|}{v^2} \left(1 + \frac{\lambda^2}{2v^2} \frac{\varepsilon^2}{v^2} \left(v q_y - B_x \right)^2 \right) \\
& - i n_i V_0^2 \frac{1}{4} \frac{|\varepsilon|}{v^2} \frac{\lambda^2}{2v^2} \frac{\varepsilon^2}{v^2} \left(v q_x + B_y + \mathcal{J} S_y \right)^2 \\
& - i n_i V_0^2 \frac{1}{4} \frac{|\varepsilon|}{v^2} \frac{\lambda^2}{v^2} \left(B_x q_x + \left(B_y + \mathcal{J} S_y \right) q_y \right)^2 ,
\end{aligned} \tag{6.40}
$$

$$
\begin{aligned}
\Sigma_x^R =& \pm i \lambda n_i V_0^2 \frac{1}{4v^2} \frac{\varepsilon^2}{v^2} \left(v q_y - B_x \right) \\
& \mp i \lambda n_i V_0^2 \frac{1}{4v^2} \frac{\varepsilon^2}{v^2} \frac{\lambda}{v} \left(B_x q_x + \left(B_y + \mathcal{J} S_y \right) q_y \right) \left(v q_x + B_y + \mathcal{J} S_y \right) ,
\end{aligned} \tag{6.41}
$$

$$
\begin{aligned}
\Sigma_y^R =& \mp i \lambda n_i V_0^2 \frac{1}{4v^2} \frac{\varepsilon^2}{v^2} \left(v q_x + B_y + \mathcal{J} S_y \right) \\
& \mp i \lambda n_i V_0^2 \frac{1}{4v^2} \frac{\varepsilon^2}{v^2} \frac{\lambda}{v} \left(B_x q_x + \left(B_y + \mathcal{J} S_y \right) q_y \right) \left(v q_y - B_x \right) .
\end{aligned} \tag{6.42}
$$

The signs in front of Σ_x^R and Σ_y^R correspond to the positive and negative energy branches, respectively. It should be stressed that the self-energy coefficients given by Eqs. (6.40)-(6.42) is also expanded up to the second order with respect to parameter λ.

When the charge current density is oriented in the y-direction, we get

$$
\begin{aligned}
\Sigma_0^R =& - i n_i V_0^2 \frac{1}{4} \frac{|\varepsilon|}{v^2} \left(1 - \frac{\lambda^2}{2v^2} \frac{\varepsilon^2}{v^2} \left(v q_y - B_x - \mathcal{J} S_x \right)^2 \right) \\
& - i n_i V_0^2 \frac{1}{4} \frac{|\varepsilon|}{v^2} \frac{\lambda^2}{2v^2} \frac{\varepsilon^2}{v^2} \left(v q_x + B_y \right)^2 \\
& - i n_i V_0^2 \frac{1}{4} \frac{|\varepsilon|}{v^2} \frac{\lambda^2}{v^2} \left(\left(B_x + \mathcal{J} S_x \right) q_x + B_y q_y \right)^2 ,
\end{aligned} \tag{6.43}
$$

$$
\begin{aligned}
\Sigma_x^R =& \pm i \lambda n_i V_0^2 \frac{1}{4v^2} \frac{\varepsilon^2}{v^2} \left(v q_y - \left(B_x + \mathcal{J} S_x \right) \right) \\
& \mp i \lambda n_i V_0^2 \frac{1}{4v^2} \frac{\varepsilon^2}{v^2} \frac{\lambda}{v} \left(\left(B_x + \mathcal{J} S_x \right) q_x + B_y q_y \right) \left(v q_x + B_y \right) ,
\end{aligned} \tag{6.44}
$$

$$
\begin{aligned}
\Sigma_y^R =& \mp i \lambda n_i V_0^2 \frac{1}{4v^2} \frac{\varepsilon^2}{v^2} \left(v q_x + B_y \right) \\
& \mp i \lambda n_i V_0^2 \frac{1}{4v^2} \frac{\varepsilon^2}{v^2} \frac{\lambda}{v} \left(\left(B_x + \mathcal{J} S_x \right) q_x + B_y q_y \right) \left(v q_y - \left(B_x + \mathcal{J} S_x \right) \right) .
\end{aligned} \tag{6.45}
$$

The impurity-averaged retarded Green's function can be found from the Dyson's equation (Chapter 5)

$$
\left[G_{\mathbf{q}}^R(\varepsilon) \right]^{-1} = \left[G_{\mathbf{q}}^{0R}(\varepsilon) \right]^{-1} - \Sigma_{\mathbf{q}}^R(\varepsilon). \tag{6.46}
$$

Solving this equation and making all the necessary substitutions of Eq. (6.22) and Eq. (6.39) and simplifications, after algebraic transformations, the impurity-averaged retarded Green's function can be expressed in the following form

$$
G_{\mathbf{q}}^R(\varepsilon) = G_{0\,\mathbf{q}}^R(\varepsilon) \sigma_0 + G_{x\,\mathbf{q}}^R(\varepsilon) \sigma_x + G_{y\,\mathbf{q}}^R(\varepsilon) \sigma_y, \tag{6.47}
$$

where

$$G_{0\mathbf{q}}^{R}(\varepsilon) = \frac{\varepsilon}{2\varepsilon + i(\Gamma_{\mathbf{q}+} + \Gamma_{\mathbf{q}-})} (G_{\mathbf{q}+}^{R} + G_{\mathbf{q}-}^{R}), \tag{6.48a}$$

$$G_{x\mathbf{q}}^{R}(\varepsilon) = \frac{vq_y}{2\varepsilon + i(\Gamma_{\mathbf{q}+} + \Gamma_{\mathbf{q}-})} (G_{\mathbf{q}+}^{R} + G_{\mathbf{q}-}^{R}), \tag{6.48b}$$

$$G_{y\mathbf{q}}^{R}(\varepsilon) = -\frac{vq_x}{2\varepsilon + i(\Gamma_{\mathbf{q}+} + \Gamma_{\mathbf{q}-})} (G_{\mathbf{q}+}^{R} + G_{\mathbf{q}-}^{R}) \tag{6.48c}$$

with $G_{\mathbf{q}\pm}^{R}(\varepsilon) = \frac{1}{\varepsilon \mp qv + i\Gamma_{\mathbf{q}\pm}}$ and relaxation rates, $\Gamma_{\mathbf{q}\pm} = \Gamma_{\pm}(\varepsilon)$, defined as follows

$$\Gamma_{\mathbf{q}\pm} = \Gamma_0(1 + \gamma_{\mathbf{q}\pm}), \tag{6.49}$$

where $\Gamma_0 = \frac{1}{4} n_i V_0^2 \frac{|\varepsilon|}{v^2}$ and $\gamma_{\mathbf{q}\pm}$ is a correction due to SO part of the scattering potential, and depends on $\mathbf{B}_{\text{eff}}$.

$$\begin{aligned}
\gamma_{\mathbf{q}+} = & -\lambda \frac{1}{|\varepsilon|}\frac{\varepsilon^3}{v^2} + \frac{\lambda^2}{2}\frac{\varepsilon^2}{v^4}\left(\varepsilon^2 + 3\left(B_x^2 + (B_y + \mathcal{J}S_y)^2\right)\right) \\
& + \lambda^2 \frac{\varepsilon^2}{v^4}\left(2B_x\left(B_y + \mathcal{J}S_y\right)\sin 2\phi + \left(B_x^2 - (B_y + \mathcal{J}S_y)^2\right)\cos 2\phi\right) \\
& - \lambda \frac{\varepsilon^2}{v^2}\left(\lambda \frac{\varepsilon}{v^2} - \frac{1}{|\varepsilon|}\right)\left(B_x \sin\phi - (B_y + \mathcal{J}S_y)\cos\phi\right),
\end{aligned} \tag{6.50}$$

$$\begin{aligned}
\gamma_{\mathbf{q}-} = & \lambda \frac{1}{|\varepsilon|}\frac{\varepsilon^3}{v^2} + \frac{\lambda^2}{2}\frac{\varepsilon^2}{v^4}\left(\varepsilon^2 + \left(2 - \frac{|\varepsilon|}{\varepsilon}\right)\left(B_x^2 + (B_y + \mathcal{J}S_y)^2\right)\right) \\
& + \frac{\lambda^2}{2}\frac{\varepsilon^2}{v^4}\left(1 - \frac{|\varepsilon|}{\varepsilon}\right)\left(2B_x\left(B_y + \mathcal{J}S_y\right)\sin 2\phi + \left(B_x^2 - (B_y + \mathcal{J}S_y)^2\right)\cos 2\phi\right) \\
& - \lambda \frac{\varepsilon^2}{v^2}\left(\lambda \frac{\varepsilon}{v^2} + \frac{1}{|\varepsilon|}\right)\left(B_x \sin\phi - (B_y + \mathcal{J}S_y)\cos\phi\right),
\end{aligned} \tag{6.51}$$

where used the transition to radial variables $q_x = q\cos\phi$, $q_y = q\sin\phi$. It should be stressed that $\Gamma_{\mathbf{q}+}(\varepsilon_{\text{F}} > 0) = \Gamma_{\mathbf{q}-}(\varepsilon_{\text{F}} < 0) = \Gamma$, and $\Gamma = \frac{\hbar}{2\tau}$ is the relaxation rate at the Fermi level (τ is the corresponding relaxation time) [7, 242].

With the analogy to the Eqs. (6.47) and (6.48) the impurity-averaged advanced Green's function will have the form

$$G_{\mathbf{q}}^{A}(\varepsilon) = G_{0\mathbf{q}}^{A}(\varepsilon)\sigma_0 + G_{x\mathbf{q}}^{A}(\varepsilon)\sigma_x + G_{y\mathbf{q}}^{A}(\varepsilon)\sigma_y, \tag{6.52}$$

where

$$G_{0\mathbf{q}}^{A}(\varepsilon) = \frac{\varepsilon}{2\varepsilon - i(\Gamma_{\mathbf{q}+} + \Gamma_{\mathbf{q}-})} (G_{\mathbf{q}+}^{A} + G_{\mathbf{q}-}^{A}), \tag{6.53a}$$

$$G_{x\mathbf{q}}^{A}(\varepsilon) = \frac{vq_y}{2\varepsilon - i(\Gamma_{\mathbf{q}+} + \Gamma_{\mathbf{q}-})} (G_{\mathbf{q}+}^{A} + G_{\mathbf{q}-}^{A}), \tag{6.53b}$$

$$G_{y\mathbf{q}}^{A}(\varepsilon) = -\frac{vq_x}{2\varepsilon - i(\Gamma_{\mathbf{q}+} + \Gamma_{\mathbf{q}-})} (G_{\mathbf{q}+}^{A} + G_{\mathbf{q}-}^{A}) \tag{6.53c}$$

with $G_{\mathbf{q}\pm}^{A}(\varepsilon) = \frac{1}{\varepsilon \mp qv - i\Gamma_{\mathbf{q}\pm}}$.

The above expressions for impurity-averaged Green's functions and relaxation rate (time)

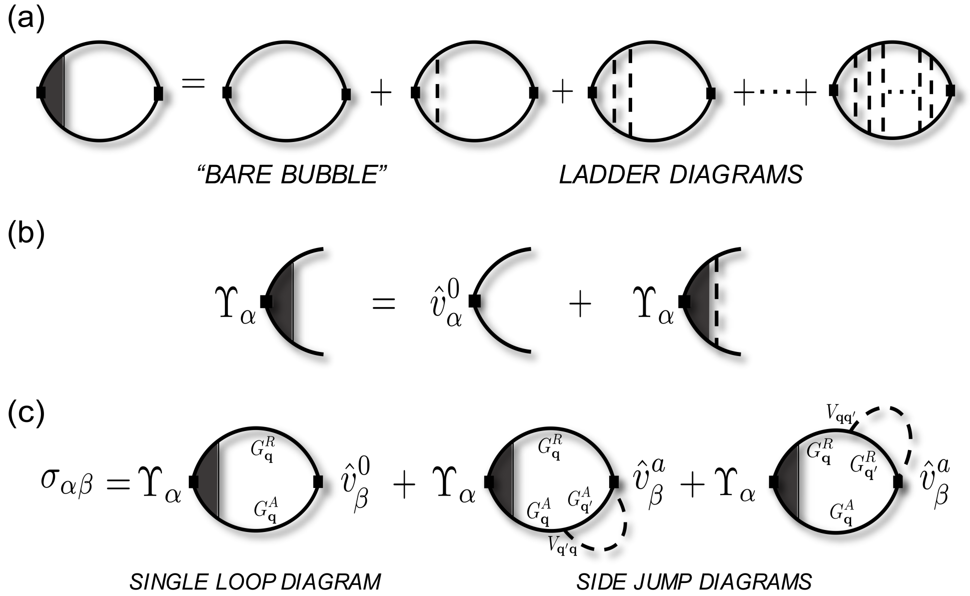

Figure 6.1: (a) Ladder approximation. (b) α-th component of renormalised velocity vertex function Υ_α. (c) Diagrammatic representation of the conductivity tensor elements $\sigma_{\alpha\beta}$ [243].
Reprinted with permission from K. Boboshko, A. Dyrdał: Phys. Rev. B. **109**, 155420 (2024). Copyright (2024) by the American Physical Society.

allow us to obtain diagonal and off-diagonal elements of the conductivity tensor within the diagrammatic perturbation expansion of the Green's function in two levels of the approximation, as presented in Fig. 6.1. For simplicity (without loss of generality), we consider further only the case when the Fermi energy is positive, i.e., only the conduction band contributes to the conductivity [243].

6.1.5 Electric Conductivity

As the SO field $\mathbf{B}_{\text{SO}}$, that we introduced to the Hamiltonian (6.2), already depends on the electric field (Section 6.1.1), the nonlinear to external electric field system response can be obtained using perturbation expansion of Green's function up to the first order with respect to $H^{\mathbf{A}}_{\mathbf{qq}'}$. Accordingly, the corresponding diagrams are depicted in Fig. 6.1. The elements of the conductivity tensor can be written as follows [243]

$$\sigma_{\alpha\beta} = \sigma^{(1)}_{\alpha\beta} + \sigma^{(2)}_{\alpha\beta} + \sigma^{(3)}_{\alpha\beta}, \tag{6.54}$$

where

$$\sigma^{(1)}_{\alpha\beta} = \frac{e^2\hbar}{2\pi}\int \frac{d^2\mathbf{q}}{(2\pi)^2}\mathrm{Tr}\langle \Upsilon_\alpha\, G^R_{\mathbf{q}}\, \hat{v}^0_\beta\, G^A_{\mathbf{q}}\rangle, \tag{6.55}$$

$$\sigma^{(2)}_{\alpha\beta} = \frac{e^2\hbar}{2\pi}\int \frac{d^2\mathbf{q}}{(2\pi)^2}\int \frac{d^2\mathbf{q}'}{(2\pi)^2}\mathrm{Tr}\left\langle \Upsilon_\alpha\, G^R_{\mathbf{q}}\, V_{\mathbf{qq}'}\, G^R_{\mathbf{q}'}\, \hat{v}^a_{\beta\,\mathbf{q}'\mathbf{q}}\, G^A_{\mathbf{q}}\right\rangle, \tag{6.56}$$

$$\sigma^{(3)}_{\alpha\beta} = \frac{e^2\hbar}{2\pi}\int \frac{d^2\mathbf{q}}{(2\pi)^2}\int \frac{d^2\mathbf{q}'}{(2\pi)^2}\mathrm{Tr}\left\langle \Upsilon_\alpha\, G^R_{\mathbf{q}}\, \hat{v}^a_{\beta\,\mathbf{qq}'}\, G^A_{\mathbf{q}'}\, V_{\mathbf{q}'\mathbf{q}}\, G^A_{\mathbf{q}}\right\rangle. \tag{6.57}$$

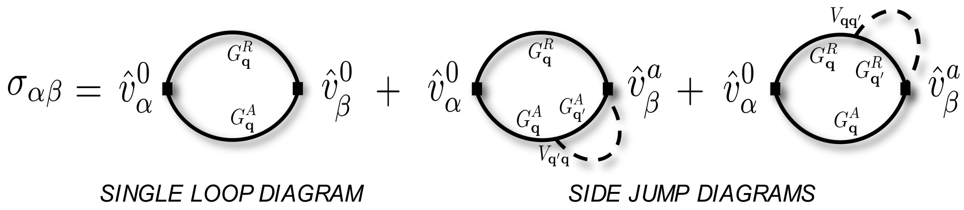

Figure 6.2: Diagrammatic representation of the conductivity tensor elements $\sigma_{\alpha\beta}$ in the "bare bubble" approximation [242].

The first term corresponds to the first diagram that is the so-called single-loop diagram with the α-th component of the renormalized velocity vertex function Υ_α, which contains the information about the approximation, i.e., this term describes conductivity in the ladder approximation (or "bare bubble" approximation, as one of the levels of approximation). The contribution related to the second and third diagrams due to the anomalous velocity describes the side-jump scattering processes (Fig. 6.1(c)). The skew-scattering diagrams are not considered, as we assumed that the disorder is described by the Gaussian distribution [7].

6.2 "Bare Bubble" Approximation

For a deeper understanding of the system, we consider first the case of the "bare bubble" approximation. That is, only one diagram is taken into account from the series, presented in Fig. 6.1(a), so-called "bare bubble" diagram [242]. This also means that we consider the case without the vertex correction. Instead of the α-th component of renormalised velocity vertex function, Υ_α, only the ordinary part of the velocity operator $\hat{v}^0_{\mathbf{qq}'}$ in a form Eq. (6.18) is taken. In the result, the diagrammatic representation of the conductivity tensor in the "bare bubble" approximation will take a form, depicted in Fig. 6.2. The contributions to the conductivity (6.54) take the following explicit form

$$\sigma^{(1)}_{\alpha\beta} = \frac{e^2\hbar}{2\pi}\int\frac{d^2\mathbf{q}}{(2\pi)^2}\mathrm{Tr}\langle\hat{v}^0_\alpha\, G^R_{\mathbf{q}}\,\hat{v}^0_\beta\, G^A_{\mathbf{q}}\rangle, \tag{6.58}$$

$$\sigma^{(2)}_{\alpha\beta} = \frac{e^2\hbar}{2\pi}\int\frac{d^2\mathbf{q}}{(2\pi)^2}\int\frac{d^2\mathbf{q}'}{(2\pi)^2}\mathrm{Tr}\left\langle\hat{v}^0_\alpha\, G^R_{\mathbf{q}}\, V_{\mathbf{qq}'}\, G^R_{\mathbf{q}'}\,\hat{v}^a_{\beta\,\mathbf{q}'\mathbf{q}}\, G^A_{\mathbf{q}}\right\rangle, \tag{6.59}$$

$$\sigma^{(3)}_{\alpha\beta} = \frac{e^2\hbar}{2\pi}\int\frac{d^2\mathbf{q}}{(2\pi)^2}\int\frac{d^2\mathbf{q}'}{(2\pi)^2}\mathrm{Tr}\left\langle\hat{v}^0_\alpha\, G^R_{\mathbf{q}}\,\hat{v}^a_{\beta\,\mathbf{qq}'}\, G^A_{\mathbf{q}'}\, V_{\mathbf{q}'\mathbf{q}}\, G^A_{\mathbf{q}}\right\rangle. \tag{6.60}$$

Then we can find the analytical solutions for longitudinal and transverse conductivities in the "bare bubble" approximation that will be used to define magnetoresistance (MR) and its components.

The calculations of the longitudinal conductivity one can start from calculations of each traces $T^{(1)}$, $T^{(2)}$ and $T^{(3)}$ separately. Then, for further simplification of the integration over $\mathbf{q}$

and $\mathbf{q}'$, it is need to sum traces from Eqs. (6.59) and (6.60). In the result one can get

$$T^{(1)} = \frac{2v^2}{\hbar^2}\left(\varepsilon^2 + q^2v^2\cos 2\phi\right)\frac{\left(G^A_{\mathbf{q}+} + G^A_{\mathbf{q}-}\right)\left(G^R_{\mathbf{q}+} + G^R_{\mathbf{q}-}\right)}{\left(2\varepsilon - i\left(\Gamma_{\mathbf{q}+} + \Gamma_{\mathbf{q}-}\right)\right)\left(2\varepsilon + i\left(\Gamma_{\mathbf{q}+} + \Gamma_{\mathbf{q}-}\right)\right)}, \tag{6.61}$$

$$\begin{aligned} T^{(2+3)} &= \frac{2v^2}{\hbar^2}\lambda\, n_i V_0^2 q'\left(q\sin\phi - q'\sin\phi'\right)\left(\varepsilon^2\sin\phi' + q^2v^2\sin\left(\phi' - 2\phi\right)\right) \\ &\times \frac{\left(G^A_{\mathbf{q}+} + G^A_{\mathbf{q}-}\right)\left(G^R_{\mathbf{q}+} + G^R_{\mathbf{q}-}\right)}{\left(2\varepsilon - i\left(\Gamma_{\mathbf{q}+} + \Gamma_{\mathbf{q}-}\right)\right)\left(2\varepsilon + i\left(\Gamma_{\mathbf{q}+} + \Gamma_{\mathbf{q}-}\right)\right)} \\ &\times \left(\frac{G^A_{\mathbf{q}'+} + G^A_{\mathbf{q}-}}{2\varepsilon - i\left(\Gamma_{\mathbf{q}'+} + \Gamma_{\mathbf{q}'-}\right)} + \frac{G^R_{\mathbf{q}'+} + G^R_{\mathbf{q}-}}{2\varepsilon + i\left(\Gamma_{\mathbf{q}'+} + \Gamma_{\mathbf{q}'-}\right)}\right). \end{aligned} \tag{6.62}$$

Making integration over $\mathbf{q}$ and $\mathbf{q}'$, after algebraic transformations, the longitudinal conductivity at Fermi energy for the electric field, applied in the x-direction will have a form

$$\sigma_{xx} = \frac{e^2}{8\pi\hbar}\frac{\varepsilon_{\mathrm{F}}}{\Gamma_0}\left(1 + \lambda\frac{\varepsilon_{\mathrm{F}}^2}{v^2}\left(1 + \frac{\Gamma_0^2}{\varepsilon_{\mathrm{F}}^2}\right) - \frac{\lambda^2}{2}\frac{\varepsilon_{\mathrm{F}}^4}{v^4}\left(1 - \frac{2\Gamma_0^2}{\varepsilon_{\mathrm{F}}^2}\right) - \lambda^2\frac{\varepsilon_{\mathrm{F}}^2}{v^4}\left(2B_x^2 + \left(B_y + \mathcal{J}S_y\right)^2\right)\right). \tag{6.63}$$

Then, in the limit of low-impurity concentration one can further make a simplification that leads to the analytical representation of the longitudinal conductivity in the "bare bubble" approximation (with expansion up to the second-order of the SOC parameter λ) [7, 242]

$$\sigma_{xx} = \frac{e^2}{8\pi\hbar}\frac{\varepsilon_{\mathrm{F}}}{\Gamma_0}\left(1 + \lambda\frac{\varepsilon_{\mathrm{F}}^2}{v^2} - \frac{\lambda^2}{2}\frac{\varepsilon_{\mathrm{F}}^4}{v^4} - \lambda^2\frac{\varepsilon_{\mathrm{F}}^2}{v^4}\left(B^2(1 + \cos^2\theta) + 2\mathcal{J}S_yB\sin\theta\right)\right). \tag{6.64}$$

In analogical way to derivation of σ_{xx} one can derive analytical expression for σ_{yx}

$$\sigma_{yx} = -\frac{e^2}{8\pi\hbar}\frac{\varepsilon_{\mathrm{F}}}{\Gamma_0}\frac{\lambda^2}{2}\frac{\varepsilon_{\mathrm{F}}^2}{v^4}\left(B^2\sin 2\theta + 2\mathcal{J}S_yB\cos\theta\right). \tag{6.65}$$

Magnetoresistance

Based on the results for the conductivity tensor and taking into account the explicit form of $\mathcal{J}$ and relation between the nonequilibrium spin polarization and charge current density as Eq. (6.11), we can find the longitudinal resistance, from which we can further determine MR.

According to the definition, the resistivity tensor is inverse to the conductivity tensor. So, for the diagonal and off-diagonal components of the resistivity tensor one can find

$$\rho_{xx} = \frac{\sigma_{xx}}{\sigma_{xx}\sigma_{yy} - \sigma_{xy}\sigma_{yx}}, \tag{6.66}$$

$$\rho_{yx} = -\frac{\sigma_{yx}}{\sigma_{xx}\sigma_{yy} - \sigma_{xy}\sigma_{yx}}. \tag{6.67}$$

After algebraic transformations, the longitudinal and transverse resistivity with the assumption that the electric field (current) is parallel to the x axis and expansion up to the second-order of the SOC parameter λ, can be written as follows:

$$\rho_{xx} = \frac{4h}{e^2}\frac{\Gamma_0}{\varepsilon_{\mathrm{F}}}\left(1 - \tilde{\lambda} + \frac{3}{2}\tilde{\lambda}^2\right) + \frac{4h}{e^2}\frac{\Gamma_0}{\varepsilon_{\mathrm{F}}}\tilde{\lambda}^2\left(\frac{B^2}{\varepsilon_{\mathrm{F}}^2}\left(1 + \cos^2\theta\right) - 4v\frac{h}{e}\frac{Bj_x}{\varepsilon_{\mathrm{F}}^3}\sin\theta\right), \tag{6.68}$$

$$\rho_{yx} = \frac{2h}{e^2}\frac{\Gamma_0}{\varepsilon_{\mathrm{F}}}\tilde{\lambda}^2\left(\frac{B^2}{\varepsilon_{\mathrm{F}}^2}\sin 2\theta - 4v\frac{h}{e}\frac{Bj_x}{\varepsilon_{\mathrm{F}}^3}\cos\theta\right), \tag{6.69}$$

where $\tilde{\lambda} = \lambda k_{\mathrm{F}}^2$ is a dimensionless parameter.

After substitution the expression for the amplitude of the applied magnetic field in the form $B = g\mu_B b$, and introducing the following notation $\rho_{xx}^0 = 4\frac{h}{e^2}\frac{\Gamma_0}{\varepsilon_{\mathrm{F}}}\left(1 - \tilde{\lambda} + \frac{3}{2}\tilde{\lambda}^2\right)$, $\rho_{yx}^0 = 2\frac{h}{e^2}\frac{\Gamma_0}{\varepsilon_{\mathrm{F}}}\tilde{\lambda}^2$, where ρ_{xx}^0, and ρ_{yx}^0 are respectively the longitudinal and transverse resistivities in the absence of the external magnetic field, and $\mathcal{F}_{xx}\left(b, j_x\right) = \left(g\mu_B\right)^2 \frac{b^2}{\varepsilon_{\mathrm{F}}^2}\left(1 + \cos^2\theta\right) - 4v\frac{h}{e}g\mu_B\frac{bj_x}{\varepsilon_{\mathrm{F}}^3}\sin\theta$ and $\mathcal{F}_{yx}\left(b, j_x\right) = \left(g\mu_B\right)^2 \frac{b^2}{\varepsilon_{\mathrm{F}}^2}\sin 2\theta\ -4v\frac{h}{e}g\mu_B\frac{bj_x}{\varepsilon_{\mathrm{F}}^3}\cos\theta$, one can simplify the longitudinal and transverse resistivities in the "bare bubble" approximation to the form [7, 242]

$$\rho_{xx} = \rho_{xx}^0\left(1 + \frac{\tilde{\lambda}^2}{1 - \tilde{\lambda} + \frac{3}{2}\tilde{\lambda}^2}\mathcal{F}_{xx}\left(b, j_x\right)\right), \tag{6.70}$$

$$\rho_{yx} = \rho_{yx}^0\,\mathcal{F}_{yx}\left(b, j_x\right). \tag{6.71}$$

To describe relative MR we need to use the conventional definition with $\rho = \rho_{xx}$, MR $= \left[\rho\left(b\right) - \rho\left(b = 0\right)\right]/\rho\left(b = 0\right)$, as well as its symmetric and antisymmetric components. Without loss of generality one can assume that the charge current density is oriented along x-direction. In such a case, after substitution of Eq. (6.70) in the mentioned definition of MR, one finds:

$$\mathrm{MR} = \frac{\tilde{\lambda}^2}{1 - \tilde{\lambda} + \frac{3}{2}\tilde{\lambda}^2}\mathcal{F}\left(b, j_x\right). \tag{6.72}$$

The symmetric component of MR, that does not change upon the sign reversal of charge current density, is called quadratic magnetoresistance. According to the definition QMR $= \left[\mathrm{MR}\left(j_\alpha = j\right) + \mathrm{MR}\left(j_\alpha = -j\right)\right]/2$ (assuming $j_\alpha = j_x$), and after algebraic transformation one gets

$$\mathrm{QMR} = 2\frac{\tilde{\lambda}^2}{1 - \tilde{\lambda} + \frac{3}{2}\tilde{\lambda}^2}\frac{\left(g\mu_B\right)^2}{\varepsilon_{\mathrm{F}}^2}b^2\left(1 + \cos^2\theta\right). \tag{6.73}$$

The antisymmetric part of MR is called bilinear magnetoresistance (Section 3.3), as it behaves linearly with both charge current density and external in-plane magnetic field. BMR is defined as BMR $= \left[\mathrm{MR}\left(j_\alpha = j\right) - \mathrm{MR}\left(j_\alpha = -j\right)\right]/2$ (where $j_\alpha = j_x$), and after algebraic transformations one finds [7, 242]

$$\mathrm{BMR} = 4\frac{\tilde{\lambda}^2}{1 - \tilde{\lambda} + \frac{3}{2}\tilde{\lambda}^2}\frac{h}{|e|}vg\mu_B\frac{bj_x}{\varepsilon_{\mathrm{F}}^3}\sin\theta. \tag{6.74}$$

From magnetotransport measurement, it is easy to extract amplitudes of QMR and BMR signals that, based on the above equations, take the following analytical form

$$A_{\mathrm{BMR}} = 4\frac{\tilde{\lambda}^2}{1 - \tilde{\lambda} + \frac{3}{2}\tilde{\lambda}^2}\frac{h}{|e|}vg\mu_B\frac{bj_x}{\varepsilon_{\mathrm{F}}^3}, \tag{6.75}$$

$$A_{\mathrm{QMR}} = 2\frac{\tilde{\lambda}^2}{1 - \tilde{\lambda} + \frac{3}{2}\tilde{\lambda}^2}\frac{\left(g\mu_B\right)^2}{\varepsilon_{\mathrm{F}}^2}b^2, \tag{6.76}$$

as well as the ratio

$$\frac{A_{\mathrm{BMR}}}{A_{\mathrm{QMR}}} = 2\frac{h}{|e|}\frac{v}{g\mu_B}\frac{j_x}{b\varepsilon_{\mathrm{F}}}. \tag{6.77}$$

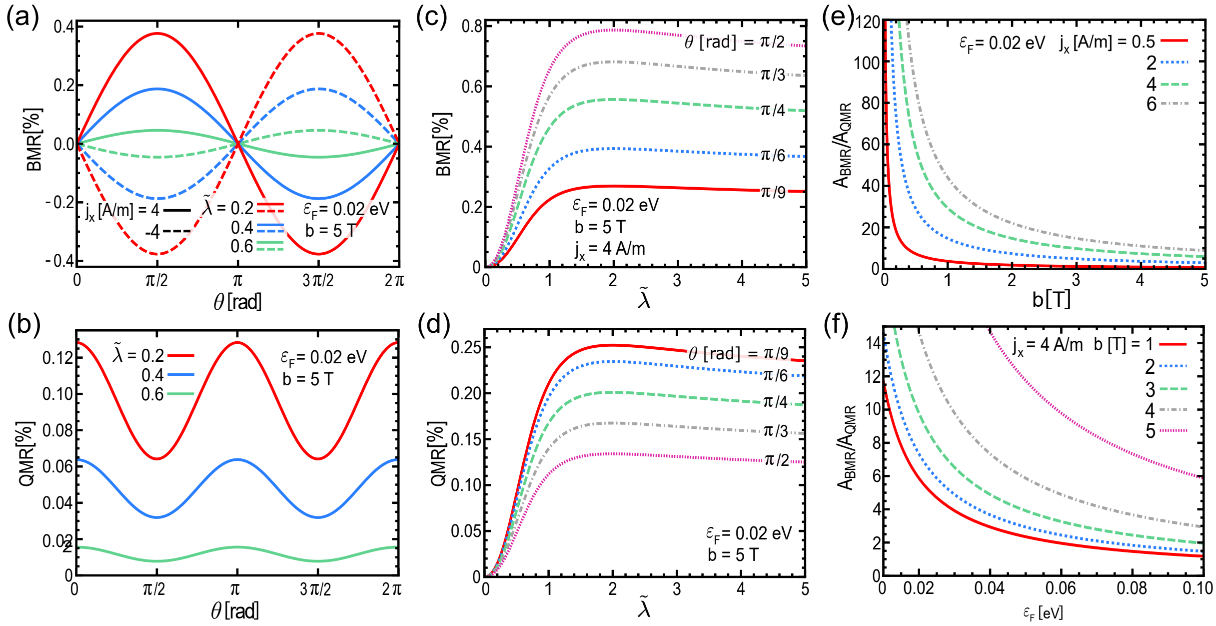

Figure 6.3: BMR (a) and QMR (b) as a function of the angle between external magnetic field b and the axis x (the axis x is parallel to the current orientation j_x) for indicated values of the parameter $\tilde{\lambda}$ proportional to the SOC parameter λ. The solid (dashed) line in the case of BMR corresponds to positive (negative) current. BMR (c) and QMR (d) as functions of the parameter $\tilde{\lambda}$ for various orientations of the magnetic field. Both BMR and QMR reach saturation at the high $\tilde{\lambda}$ values. Ratio of the amplitudes of BMR and QMR as a function of the magnetic field b for different current densities j_x (e) and as a function of the Fermi energy ε_{F} for different values of magnetic field (f). $n_i V_0^2 = 1.58 \times 10^{-24}\,\mathrm{eV^2m^2}$ and the other parameters as indicated [242].

This ratio is a quite universal quantity which depends only on the universal constants and experimentally controlled amplitudes of the magnetic b field and charge current density j_x.

From Eqs. (6.75) and (6.76) follows that BMR and QMR drop with increasing Fermi energy as $1/\varepsilon_{\mathrm{F}}^3$ and $1/\varepsilon_{\mathrm{F}}^2$, respectively. Accordingly, ratio of the amplitudes of BMR and QMR also drops with increasing ε_{F} as $1/\varepsilon_{\mathrm{F}}$, see Eq. (6.77). In turn, BMR grows linearly with magnetic field b while QMR grows with b as b^2. Thus, the ratio of the amplitudes of BMR and QMR drops with increasing b as $1/b$.

In Figs. 6.3(a)-(b) we show BMR and QMR as a function of the angle between magnetic field b and the axis x (parallel to current) for two opposite orientations of charge current density (it can be positive or negative), and for indicated values of the normalized SOC parameter $\tilde{\lambda}$. From this figure follows that BMR changes sign when the direction of current flow is reversed. In addition, BMR varies periodically with the angle θ between magnetic field and current direction (with period equal to 2π), and changes sign when the field is rotated to the opposite orientation. Apart from this, absolute magnitude of BMR appears when magnetic field is oriented perpendicularly to the current direction, and disappears when magnetic field is parallel to the current. In turn, QMR has two components, one is independent of the angle θ between magnetic field and current direction, and another one which varies periodically with θ, with the period equal to π. This behaviour of BMR and QMR is in qualitative agreement with that observed in other models of BMR. From this figure follows that both, BMR and QMR tend to zero in the limit of zero SOC $\lambda \to 0$ [242].

Figs. 6.3(c)-(d) shows BMR and QMR as a function of the normalized SOC parameter $\tilde{\lambda}$, and for a constant Fermi energy. Note, both BMR and QMR vanish for $\tilde{\lambda} \to 0$, and for small values of $\tilde{\lambda}$ they increase rapidly with $\tilde{\lambda}$. Upon reaching a maximum value they slowly decrease with increasing $\tilde{\lambda}$ and saturate for large values of $\tilde{\lambda}$ (according to the prefactors in Eqs. (6.73) and (6.74)).

Figs. 6.3(e)-(f), in turn, shows the ratio of the amplitude of BMR to that of QMR as a function of the magnitude of magnetic field b (Fig. 6.3(e)) and also as a function of the Fermi energy ε_{F} (Fig. 6.3(f)), and for indicated other parameters. From this figure follows that the amplitude ratio falls down with increasing magnetic field b, in agreement with Eq. (6.77), from which follows that this ratio is proportional to $1/b$. This is because amplidude of QMR grows faster with b than the amplidude of BMR, as already discussed above. Interestingly, this ratio also decreases with increasing Fermi energy, as follows from Eq. (6.77).

6.3 Ladder Approximation

In this section we consider the ladder approximation which gives more detailed information about the system and processes in it. As has been mentioned in Section 6.1.5, perturbation expansion for the Green's functions leads to a series of diagrams contributing to the longitudinal and transverse conductivities. Corresponding diagrams for the conductivity tensor (6.54) in the ladder approximation are shown in Fig. 6.1(c) and their mathematical representations take the form of Eqs. (6.55)-(6.57). As mentioned earlier, term (6.55) corresponds to the single-loop diagram in the ladder approximation, $\sigma^{(1)}_{\alpha\beta} := \sigma^{l}_{\alpha\beta}$. Terms (6.56)-(6.57) are related to the contribution due to the anomalous velocity and contains the information about side-jump processes, $\sigma^{sj}_{\alpha\beta} := \sigma^{(2)}_{\alpha\beta} + \sigma^{(3)}_{\alpha\beta}$ [7].

6.3.1 Renormalized Vertex Function

The renormalized velocity vertex function Υ_α in Eqs. (6.55)-(6.57) can be found analytically by solving the self-consistent equation presented in Fig. 6.1(b) and taking the following mathematical representation [7, 239, 243, 246]

$$\Upsilon_\alpha = \hat{v}^0_\alpha + \int \frac{d^2\mathbf{q}'}{(2\pi)^2} H^{\mathrm{imp}}_{\mathbf{q}\mathbf{q}'}\, G^A_{\mathbf{q}'}(\varepsilon)\, \Upsilon_{\alpha\mathbf{q}'}\, G^R_{\mathbf{q}'}(\varepsilon)\, H^{\mathrm{imp}}_{\mathbf{q}'\mathbf{q}}, \tag{6.78}$$

where $\hat{v}^0_\alpha$ is given by Eq. (6.18).

Assuming that the renormalized vertex function has the following form

$$\Upsilon_\alpha = \frac{v}{\hbar}\left(\mathcal{A}_\alpha q_\alpha \sigma_0 + \mathcal{B}_\alpha \sigma_x + \mathcal{C}_\alpha \sigma_y + \mathcal{D}_\alpha \sigma_z\right), \tag{6.79}$$

substituting it into the Eq. (6.78), then, comparing the terms in front of the same Pauli matrices on the left and right sides of the equation, one gets a system of algebraic equations for coefficients $\mathcal{A}_\alpha$, $\mathcal{B}_\alpha$, $\mathcal{C}_\alpha$, $\mathcal{D}_\alpha$ [243].

Accordingly, after algebraic transformations, the coefficients in Eq. (6.79) take the following explicit form for the x-component of the renormalized velocity

$$\mathcal{A}_x = \lambda\frac{\varepsilon}{v^2}\frac{1}{q_x}\left(B_y + \mathcal{J}S_y\right) + \lambda^2\frac{\varepsilon}{v^2}\left(2q_yB_x + \frac{\varepsilon^2}{v^3}\frac{1}{q_x^2}B_y\left(B_y + 2\mathcal{J}S_y\right) + 2\frac{q_y^2}{q_x}\left(B_y + \mathcal{J}S_y\right)\right), \quad (6.80)$$

$$\begin{aligned}\mathcal{B}_x = &-4\lambda\frac{1}{v}\left(q_xB_x + q_y\left(B_y + \mathcal{J}S_y\right)\right)\\ &-\lambda^2\frac{\varepsilon^2}{v^3}\left(4\frac{1}{v}\frac{q_y}{q_x}B_y\left(B_y + 2\mathcal{J}S_y\right) + 5\frac{1}{v}B_x\left(B_y + \mathcal{J}S_y\right) - q_xq_yv\right)\\ &-14\lambda^2\frac{\varepsilon^2}{v^3}\left(q_xB_x + q_y\left(B_y + \mathcal{J}S_y\right)\right),\end{aligned} \quad (6.81)$$

$$\begin{aligned}\mathcal{C}_x = &-2 - \lambda\frac{\varepsilon^2}{v^2}\left(2 + \frac{1}{v}\frac{1}{q_x}\left(B_y + \mathcal{J}S_y\right)\right)\\ &+\lambda^2\frac{\varepsilon^2}{v^2}\left(\frac{q_x^2}{2} + \frac{3q_y^2}{2} - \frac{\varepsilon^2}{v^2} + \frac{10}{\varepsilon^2}\left(q_x^2B_x^2 + q_y^2B_y^2\right) + \frac{1}{2v^2}\left(9B_x^2 + 7B_y^2\right)\right)\\ &+\lambda^2\frac{\varepsilon^2}{v^2}\left(-\frac{\varepsilon^2}{v^4}\frac{1}{q_x^2}B_y^2 + 7\frac{1}{v^2}B_y\mathcal{J}S_y - 2\frac{\varepsilon^2}{v^4}B_y\mathcal{J}S_y\right.\\ &\left.-\frac{2}{v}\left(2q_yB_x - q_x\left(B_y + \mathcal{J}S_y\right)\right) - 2\frac{q_y^2}{q_x}\frac{1}{v}\left(B_y + \mathcal{J}S_y\right)\right)\\ &+\lambda^2\frac{\varepsilon^2}{v^2}\left(-\frac{5}{2}\frac{\varepsilon^2}{v^3}\frac{1}{q_x}\left(B_y + \mathcal{J}S_y\right) + 20\frac{q_xq_y}{\varepsilon^2}B_x\left(B_y + \mathcal{J}S_y\right) + 20\frac{q_y^2}{\varepsilon^2}B_y\mathcal{J}S_y\right),\end{aligned} \quad (6.82)$$

$$\mathcal{D}_x = 0. \quad (6.83)$$

Renormalized y-component of the velocity operator can be calculated in analogy to the x-component. In this case the coefficients in equation (6.79) have the following form:

$$\mathcal{A}_y = -\lambda\frac{\varepsilon}{v^2}\frac{1}{q_y}B_x + \lambda^2\frac{\varepsilon}{v^2}\left(\frac{\varepsilon^2}{v^3}\frac{1}{q_y^2}B_x^2 - 2\frac{q_x^2}{q_y}B_x - 2q_x\left(B_y + \mathcal{J}S_y\right)\right), \quad (6.84)$$

$$\begin{aligned}\mathcal{B}_y = &\,2 + \lambda\frac{\varepsilon^2}{v^2}\left(2 - \frac{1}{v}\frac{1}{q_y}B_x\right)\\ &+\lambda^2\frac{\varepsilon^2}{v^2}\left(-\frac{3q_x^2}{2} - \frac{q_y^2}{2} + \frac{\varepsilon^2}{v^2} - \frac{10}{\varepsilon^2}\left(q_x^2B_x^2 + q_y^2B_y^2\right) - \frac{1}{2v^2}\left(7B_x^2 + 9B_y\left(B_y + 2\mathcal{J}S_y\right)\right)\right)\\ &+\lambda^2\frac{\varepsilon^2}{v^2}\left(\frac{\varepsilon^2}{v^4}\frac{1}{q_y^2}B_x^2 + \frac{2}{v}\left(q_yB_x - 2q_x\left(B_y + \mathcal{J}S_y\right)\right) - 2\frac{q_x^2}{q_y}\frac{1}{v}B_x - 2\frac{\varepsilon^2}{v^3}\frac{1}{q_y}B_x\right)\\ &-20\lambda^2\frac{\varepsilon^2}{v^2}\frac{q_y}{\varepsilon^2}\left(q_xB_x\left(B_y + \mathcal{J}S_y\right) + q_yB_y\mathcal{J}S_y\right),\end{aligned} \quad (6.85)$$

$$\begin{aligned}\mathcal{C}_y = &-4\lambda\frac{1}{v}\left(q_xB_x + q_y\left(B_y + \mathcal{J}S_y\right)\right) + \lambda^2\frac{\varepsilon^2}{v^3}\left(4\frac{1}{v}\frac{q_x}{q_y}B_x^2 + 5\frac{1}{v}B_x\left(B_y + \mathcal{J}S_y\right)\right)\\ &-14\lambda^2\frac{\varepsilon^2}{v^3}\left(q_xB_x + q_y\left(B_y + \mathcal{J}S_y\right) - q_xq_yv\right),\end{aligned} \quad (6.86)$$

$$\mathcal{D}_y = 0. \quad (6.87)$$

Note, that the coefficients $\mathcal{A}_\alpha$, $\mathcal{B}_\alpha$, $\mathcal{C}_\alpha$, $\mathcal{D}_\alpha$ have been derived up to the second order with respect to the SOC parameter λ.

6.3.2 Electric Conductivity

Longitudinal Conductivity

Calculations of the longitudinal conductivity for the case, when the electric filed is applied parallel to the x axis, are provided in the similar way to those one, described in Section 6.2. On the beginning, it is better to calculate traces that in the result will have a form

$$
\begin{aligned}
T^{(1)} &= \frac{2v^2}{\hbar^2}\left(2\,\mathcal{A}\,q^2 v\varepsilon\cos^2\phi + \mathcal{B}\,q^2v^2\sin 2\phi - \mathcal{C}\left(\varepsilon^2 + q^2v^2\cos 2\phi\right)\right) \\
&\times \frac{\left(G^A_{\mathbf{q}+} + G^A_{\mathbf{q}-}\right)\left(G^R_{\mathbf{q}+} + G^R_{\mathbf{q}-}\right)}{\left(2\varepsilon - i\left(\Gamma_{\mathbf{q}+} + \Gamma_{\mathbf{q}-}\right)\right)\left(2\varepsilon + i\left(\Gamma_{\mathbf{q}+} + \Gamma_{\mathbf{q}-}\right)\right)},
\end{aligned} \tag{6.88}
$$

$$
\begin{aligned}
T^{(2+3)} &= \frac{2v^2}{\hbar^2}\lambda\,n_i V_0^2 q'\left(q\sin\phi - q'\sin\phi'\right)\big(2\,\mathcal{A}\,q^2v\varepsilon\cos\phi\sin\left(\phi' - \phi\right) \\
&-\mathcal{B}\left(\varepsilon^2\cos\phi' - q^2v^2\cos\left(\phi' - 2\phi\right)\right) - \mathcal{C}\left(\varepsilon^2\sin\phi' + q^2v^2\sin\left(\phi' - 2\phi\right)\right)\big) \\
&\times \frac{\left(G^A_{\mathbf{q}+} + G^A_{\mathbf{q}-}\right)\left(G^R_{\mathbf{q}+} + G^R_{\mathbf{q}-}\right)}{\left(2\varepsilon - i\left(\Gamma_{\mathbf{q}+} + \Gamma_{\mathbf{q}-}\right)\right)\left(2\varepsilon + i\left(\Gamma_{\mathbf{q}+} + \Gamma_{\mathbf{q}-}\right)\right)} \\
&\times \left(\frac{G^A_{\mathbf{q}'+} + G^A_{\mathbf{q}-}}{2\varepsilon - i\left(\Gamma_{\mathbf{q}'+} + \Gamma_{\mathbf{q}'-}\right)} + \frac{G^R_{\mathbf{q}'+} + G^R_{\mathbf{q}-}}{2\varepsilon + i\left(\Gamma_{\mathbf{q}'+} + \Gamma_{\mathbf{q}'-}\right)}\right).
\end{aligned} \tag{6.89}
$$

Taking into account expressions for coefficients of the x-component of the renormalized vertex function from Eqs. (6.80)-(6.82), making integration over $\mathbf{q}$ and $\mathbf{q}'$, and evaluation of the results up to the leading terms with respect to the parameter λ leads to the following analytical expression for the longitudinal conductivity at Fermi energy in the ladder approximation [243]

$$
\begin{aligned}
\sigma^l_{xx} &= \frac{e^2}{4\pi\hbar}\frac{\varepsilon_{\mathrm{F}}}{\Gamma_0}\left(1 + 2\lambda\frac{\varepsilon_{\mathrm{F}}^2}{v^2} + \frac{3}{4}\lambda^2\frac{\varepsilon_{\mathrm{F}}^4}{v^4} - \frac{\lambda^3}{4}\frac{\varepsilon_{\mathrm{F}}^6}{v^6}\right) \\
&- \frac{e^2}{4\pi\hbar}\frac{\varepsilon_{\mathrm{F}}}{\Gamma_0}\frac{\lambda^2}{2}\frac{\varepsilon_{\mathrm{F}}^2}{v^4}\left(B^2(7 + 8\cos^2\theta) + 14\mathcal{J}S_yB\sin\theta\right) \\
&- \frac{e^2}{4\pi\hbar}\frac{\varepsilon_{\mathrm{F}}}{\Gamma_0}\frac{3}{4}\lambda^3\frac{\varepsilon_{\mathrm{F}}^4}{v^6}\left(B^2\left(7 + 3\cos^2\theta\right) + 14\mathcal{J}S_yB\sin\theta\right)
\end{aligned} \tag{6.90}
$$

and the following contribution due to the side-jump scattering mechanism

$$
\begin{aligned}
\sigma^{sj}_{xx} &= \frac{e^2}{4\pi\hbar}\frac{\Gamma_0}{\varepsilon_{\mathrm{F}}}\lambda\frac{\varepsilon_{\mathrm{F}}^2}{v^2}\left(1 + 2\lambda\frac{\varepsilon_{\mathrm{F}}^2}{v^2} + \frac{5}{4}\lambda^2\frac{\varepsilon_{\mathrm{F}}^4}{v^4}\right) \\
&- \frac{e^2}{4\pi\hbar}\frac{\Gamma_0}{\varepsilon_{\mathrm{F}}}\frac{9}{4}\lambda^3\frac{\varepsilon_{\mathrm{F}}^4}{v^6}\left(B^2\left(1 + 2\cos^2\theta\right) + 3\mathcal{J}S_yB\sin\theta\right).
\end{aligned} \tag{6.91}
$$

The contribution from the side-jump scattering to the total conductivity is however negligibly small, as we show in Figs. 6.4(c)-(d), where the longitudinal conductivity is plotted as a function of the Fermi energy, ε_{F}, and decomposed into the contributions from the ladder term, σ^l_{xx}, and

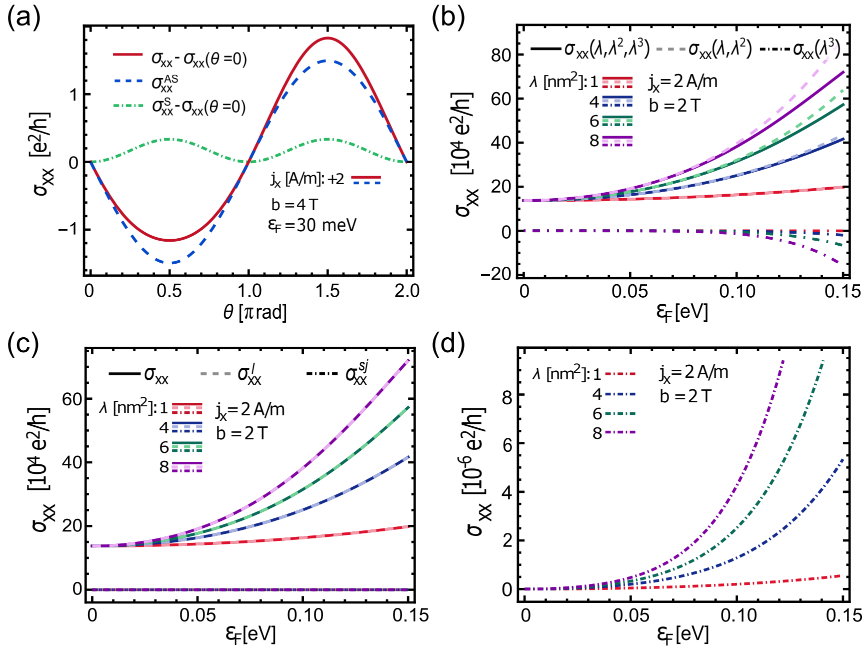

Figure 6.4: The longitudinal conductivity σ_{xx} as a function of the angle θ defining the orientation of in-plane magnetic field b with respect to x-direction (a) and Fermi energy ε_{F} (b)-(d). The angular dependence (a) is plotted for charge current density oriented along to the unit vector $\hat{\mathbf{x}}$, the symmetric and antisymmetric parts of the conductivity are also plotted. The contributions to the longitudinal conductivity from ladder and side-jump diagrams are presented in (c) and (d), whereas the contributions from the second and third orders with respect to λ to the conductivity are presented in (b). In (a) $\lambda = 6\,\mathrm{nm}^2$, whereas in (b)-(d) $\theta = \pi/2$, $n_i V_0^2 = 1.58 \times 10^{-24}\,\mathrm{eV}^2\mathrm{m}^2$ [243]. Reprinted with permission from K. Boboshko, A. Dyrdał: Phys. Rev. B. **109**, 155420 (2024). Copyright (2024) by the American Physical Society.

side-jump term, σ_{xx}^{sj}. Moreover, the terms proportional to λ^3 give a negligible contribution to the total conductivity, as it is clearly seen in Fig. 6.4(b), where the total longitudinal conductivity plotted as a function of ε_{F} is decomposed into the term containing expressions up to λ^2, i.e., $\sigma_{xx}(\lambda, \lambda^2)$, and the term proportional to λ^3, $\sigma_{xx}(\lambda^3)$. Accordingly, one can restrict the final analytical formulas for the longitudinal conductivity up to the second order terms with respect to SO parameter λ. With these terms, Eqs. (6.90) and (6.91) lead to the following expression for the dc conductivity

$$\sigma_{xx} = \sigma_{xx}^0 \left(1 - 7 \frac{\tilde{\lambda}^2}{\xi(\tilde{\lambda})} \left(\frac{B^2}{\varepsilon_{\mathrm{F}}^2} \left(\frac{1}{2} + \frac{4}{7} \cos^2\theta \right) + \frac{\mathcal{J} S_y B}{\varepsilon_{\mathrm{F}}^2} \sin\theta \right) \right), \tag{6.92}$$

where $\tilde{\lambda} = \lambda k_{\mathrm{F}}^2$ is a dimensionless parameter describing strength of SOC, $\sigma_{xx}^0 = \frac{e^2}{4\pi\hbar}\frac{\varepsilon_{\mathrm{F}}}{\Gamma}$ is the diagonal conductivity in the absence of external magnetic field, $\Gamma = \Gamma_0/\xi(\tilde{\lambda}) = \frac{\hbar}{2\tau}$ is the relaxation rate (with τ denoting the relaxation time) in the presence of SO impurity potential, and $\xi(\tilde{\lambda}) = (1 + 2\tilde{\lambda} + \frac{3}{4}\tilde{\lambda}^2)$.

Taking into account the explicit form of the relation between spin polarization and current from Eq. (6.10), the above equation can be rewritten in a form that is more useful for interpretation

$$\sigma_{xx} = \sigma_{xx}^{0}\left(1 - 7\frac{\tilde{\lambda}^2}{\xi(\tilde{\lambda})}\left(\frac{B^2}{\varepsilon_{\mathrm{F}}^2}\left(\frac{1}{2}+\frac{4}{7}\cos^2\theta\right) - 2\frac{hv}{e}\frac{j_x B_y}{\varepsilon_{\mathrm{F}}^3}\right)\right). \tag{6.93}$$

In the above equation, one can easily identify two terms that appear as a consequence of the in-plane magnetic field: (i) the term which is symmetric with respect to the sign reversal of charge current density and proportional to B^2 and (ii) the term which scales linearly with B as well as linearly with current density, and therefore it is antisymmetric with respect to the sign reversal of j_x. The symmetric part, $\sigma^{\mathrm{S}} = (\sigma(j_x = j) + (\sigma(j_x = -j))/2$, depends on the orientation of magnetic field as $\cos^2\theta$, whereas the antisymmetric one, $\sigma^{\mathrm{AS}} = (\sigma(j_x = j) - \sigma(j_x = -j))/2$, scales as $\sin\theta$. This behavior is presented in Fig. 6.4(a), where the longitudinal conductivity, σ_{xx}, is plotted as a function of the angle θ for two opposite orientations of the charge current density. We recall that the angle θ is defined as the angle between the in-plane magnetic field and the x direction. The asymmetry between $\theta = \pi/2$ and $\theta = 3\pi/2$ is well pronounced and indicates the unidirectional behavior of the system response. In Fig. 6.4(a), the total conductivity is decomposed into the symmetric and antisymmetric parts. Note that the antisymmetric part dominates. This is a feature of unidirectional magnetoresistance (UMR) in TIs (Section 3.1), where the effective SO field, $\mathbf{B}_{\mathrm{SO}}$, can be much larger than the strength of the external magnetic field.

Sometimes, it is convenient to write Eq. (6.93) in a general and compact form as [243]

$$\sigma = \sigma_0\left(1 - 7\frac{\tilde{\lambda}^2}{\xi(\tilde{\lambda})}\left(\frac{B^2}{2\varepsilon_{\mathrm{F}}^2} + \frac{4}{7}\frac{(\mathbf{j}\cdot\mathbf{B})^2}{\varepsilon_{\mathrm{F}}^2} - 2\frac{hv}{e}\frac{(\mathbf{j}\times\mathbf{B})}{\varepsilon_{\mathrm{F}}^3}\cdot\hat{\mathbf{z}}\right)\right), \tag{6.94}$$

where $\sigma_0 = \sigma_{xx}^0 = \sigma_{yy}^0$ is the isotropic longitudinal conductivity.

Transverse Conductivity

Providing calculations for the transverse conductivity σ_{yx} in the analogical way to the longitudinal conductivity σ_{xx}, making the evaluation of the single-loop diagram with the vertex correction (i.e. ladder approximation) presented in Fig. 6.1(c) for the case, when the currents flows in the x-direction, leads to the following expression

$$\begin{aligned}\sigma_{yx}^{l} = &-\frac{e^2}{4\pi\hbar}\frac{3}{\varepsilon_{\mathrm{F}}\Gamma_0}\lambda^2\frac{\varepsilon_{\mathrm{F}}^4}{v^4}\left(B^2\sin 2\theta + 2\mathcal{J}S_yB\cos\theta\right)\\ &-\frac{e^2}{2\pi\hbar}\frac{1}{\varepsilon_{\mathrm{F}}\Gamma_0}\lambda^3\frac{\varepsilon_{\mathrm{F}}^6}{v^6}\left(B^2\sin 2\theta + 2\mathcal{J}S_yB\cos\theta\right).\end{aligned} \tag{6.95}$$

In turn, diagrams describing the side-jump scattering give the following contribution

$$\sigma_{yx}^{sj} = -\frac{e^2}{16\pi\hbar}\frac{13\Gamma_0}{\varepsilon_{\mathrm{F}}^3}\lambda^3\frac{\varepsilon_{\mathrm{F}}^6}{v^6}\left(B^2\sin 2\theta + 2\mathcal{J}S_yB\cos\theta\right). \tag{6.96}$$

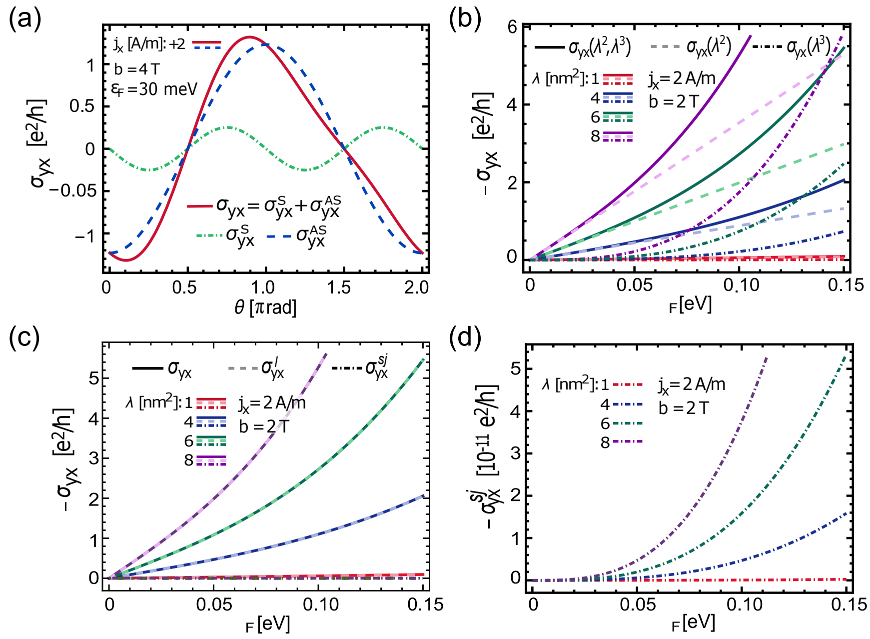

Figure 6.5: The off-diagonal conductivity σ_{yx} as a function of the angle θ, defining the orientation of in-plane magnetic field b with respect to the axis x (a) and Fermi energy ε_F (b)-(d). The angular dependence in (a) is plotted for charge current density oriented along to $\hat{\mathbf{x}}$, the symmetric and antisymmetric parts of the conductivity are also plotted there. The contributions to the off-diagonal conductivity from the ladder and side-jump diagrams are presented in (c) and (d), whereas the contributions to conductivity in second and third order with respect to λ are presented in (b). In (a) $\lambda = 6\,\mathrm{nm}^2$, whereas in (b)-(d) $\theta = 0$, $n_i V_0^2 = 1.58 \times 10^{-24}\,\mathrm{eV}^2\mathrm{m}^2$ [243].

The sum of Eqs. (6.95) and (6.96) gives the following formula for the transverse conductivity

$$\begin{aligned}\sigma_{yx} = &-\frac{e^2}{4\pi\hbar}\frac{3}{\varepsilon_{\mathrm{F}}\Gamma_0}\tilde{\lambda}^2\left(B^2\sin 2\theta + 2\mathcal{J}S_y B\cos\theta\right)\\ &-\frac{e^2}{2\pi\hbar}\frac{1}{\varepsilon_{\mathrm{F}}\Gamma_0}\tilde{\lambda}^3\left(1+\frac{13}{8}\frac{\Gamma_0^2}{\varepsilon_{\mathrm{F}}^2}\right)B^2\sin 2\theta\\ &-\frac{e^2}{2\pi\hbar}\frac{1}{\varepsilon_{\mathrm{F}}\Gamma_0}\tilde{\lambda}^3\left(1+\frac{13}{8}\frac{\Gamma_0^2}{\varepsilon_{\mathrm{F}}^2}\right)2\mathcal{J}S_y B\cos\theta.\end{aligned} \tag{6.97}$$

As follows from Figs. 6.5(c)-(d), the side-jump contribution is small. Also, the contribution of the third order in λ is negligible, see Fig. 6.5(b). Thus, the dominant term in the limit of $\Gamma_0/\varepsilon_{\mathrm{F}} \ll 1$ can be written as [243]

$$\sigma_{yx} = -\sigma_0\frac{\kappa(\tilde{\lambda})}{\varepsilon_{\mathrm{F}}^2}(B_y + \mathcal{J}S_y)B_x, \tag{6.98}$$

where $\kappa(\tilde{\lambda}) = 6\tilde{\lambda}^2\frac{1+\frac{2}{3}\tilde{\lambda}}{\xi(\tilde{\lambda})}$. Taking into account the relation between spin polarization and current density (6.10), the above equation can be rewritten in a more convenient form as

$$\sigma_{yx} = -\sigma_0\frac{\kappa(\tilde{\lambda})}{\varepsilon_{\mathrm{F}}^2}\left(B_y - 2\frac{hv}{e}\frac{j_x}{\varepsilon_{\mathrm{F}}}\right)B_x, \tag{6.99}$$

which in turn can be written as a sum of the symmetric and antisymmetric parts with respect to the reversal of charge current flow, i.e., $\sigma_{yx} = \sigma_{yx}^{\mathrm{S}} + \sigma_{yx}^{\mathrm{AS}}$.

The symmetric part, $\sigma_{yx}^{\mathrm{S}} \sim B^2 \sin 2\theta$, i.e., it is proportional to B^2 and changes with the orientation of in-plane magnetic field as $\sin 2\theta$. Thus, it has the periodicity of π. In turn, the antisymmetric part of the off-diagonal conductivity is proportional $j_x B_x$, i.e., $\sigma_{yx}^{\mathrm{AS}} \sim jB\cos\theta$. This part of the off-diagonal conductivity changes sign when the orientation of charge current density is reversed, i.e., $\sigma_{yx}^{\mathrm{AS}}(j_x) = -\sigma_{yx}^{\mathrm{AS}}(-j_x)$. Thus, this contribution is a purely nonlinear unidirectional system response to the external electric field. This component reveals the periodicity of 2π when the in-plane magnetic field rotates with respect to the orientation of the x direction. This behavior is shown in Fig. 6.5(a), where the symmetric and antisymmetric parts are shown as a function of θ. This figure also shows the total conductivity σ_{yx}.

The component σ_{xy} can be derived in a similar way to σ_{yx} and one finds [243]

$$\sigma_{xy} = \sigma_0 \frac{\kappa(\tilde{\lambda})}{\varepsilon_{\mathrm{F}}^2} \left(B_x + 2\frac{hv}{e}\frac{j_y}{\varepsilon_{\mathrm{F}}} \right) B_y. \tag{6.100}$$

Accordingly, for describing the planar Hall effect in the system, the planar Hall conductivity can be presented in general and compact form as

$$\sigma_{\mathrm{PH}} = \sigma_0 \frac{\kappa(\tilde{\lambda})}{\varepsilon_{\mathrm{F}}^2} \left((\mathbf{B} \times \mathbf{j}) \cdot \hat{\mathbf{z}} + 2\frac{hv}{e}\frac{j}{\varepsilon_{\mathrm{F}}} \right) \mathbf{j} \cdot \mathbf{B}, \tag{6.101}$$

where j is an amplitude of charge current density vector $\mathbf{j}$.

The above equation can be written as a sum of the symmetric and antisymmetric parts with respect to the reversal of charge current flow, i.e., $\sigma_{\mathrm{PH}} = \sigma_{\mathrm{PH}}^{\mathrm{S}} + \sigma_{\mathrm{PH}}^{\mathrm{AS}}$. The symmetric part, $\sigma_{\mathrm{PH}}^{\mathrm{S}} = \sigma_{xy}^{\mathrm{S}} = -\sigma_{yx}^{\mathrm{S}} \sim (\mathbf{j}\cdot\mathbf{B})(\mathbf{j}\times\mathbf{B})$, is proportional to B^2 and changes with the orientation of the in-plane magnetic field with respect to the direction of the charge current density, with periodicity π. The antisymmetric part of the off-diagonal conductivity, $\sigma_{yx}^{\mathrm{AS}} = \sigma_{xy}^{\mathrm{AS}} \sim (\mathbf{j} \cdot \mathbf{B})$, is proportional to the nonequilibrium spin polarization as $\mathbf{S} \sim \mathbf{j} \times \hat{\mathbf{z}}$. This part of the off-diagonal conductivity changes the sign when the charge current density is reversed, i.e., $\sigma_{\mathrm{PH}}^{\mathrm{AS}}(j_x) = -\sigma_{\mathrm{PH}}^{\mathrm{AS}}(-j_x)$. Thus, this contribution is a purely nonlinear (unidirectional) system response to the external electric field. This component reveals the periodicity of 2π when the in-plane magnetic field rotates with respect to the orientation of the charge current.

6.3.3 Magnetoresistance and Nonlinear Planar Hall Angle

Based on the analytical results, found in the Section 6.3.2, we can derive the expressions for the components of the resistivity tensor and magnetoresistance (MR) [11, 204, 243].

According to the definition of the resistivity, $\boldsymbol{\rho} = [\boldsymbol{\sigma}]^{-1}$, with the assumption that the electric field (current) is parallel to the x axis, after algebraic transformations, the diagonal Eq. (6.66) and off-diagonal Eq. (6.67) components of the resistivity tensor take the following form

$$\begin{aligned}\rho_{xx} &= \frac{2h}{e^2}\frac{\Gamma_0}{\varepsilon_\mathrm{F}}\left(1+2\tilde{\lambda}+\frac{3}{4}\tilde{\lambda}^2\right)\\ &+\frac{14h}{e^2}\frac{\Gamma_0}{\varepsilon_\mathrm{F}}\tilde{\lambda}^2\left(\frac{B^2}{\varepsilon_\mathrm{F}^2}\left(\frac{1}{2}+4\cos^2\theta\right)-2v\frac{h}{e}\frac{Bj_x}{\varepsilon_\mathrm{F}^3}\sin\theta\right),\end{aligned} \tag{6.102}$$

$$\rho_{yx} = \frac{6h}{e^2}\frac{\Gamma_0}{\varepsilon_\mathrm{F}}\tilde{\lambda}^2\left(\frac{B^2}{\varepsilon_\mathrm{F}^2}\sin 2\theta-4v\frac{h}{e}\frac{Bj_x}{\varepsilon_\mathrm{F}^3}\cos\theta\right). \tag{6.103}$$

Comparing the obtained equation for the longitudinal resistivity with the previously obtained in Section 6.2, Eq. (6.70), we see that the behavior of the resistivity in our system in the different approximations is preserved.

From definitions for the relative MR and its symmetric and antisymmetric components, quadratic (QMR) and bilinear magnetoresistance (BMR), mentioned in Section 6.2 and results from Section 6.3.2, after algebraic transformations one finds the resulting expression for MR

$$\mathrm{MR} = 7\tilde{\lambda}^2\xi(\tilde{\lambda})\left(\frac{(g\mu_B)^2}{\varepsilon_\mathrm{F}^2}b^2\left(\frac{1}{2}+4\cos^2\theta\right)+2\frac{h}{e}vg\mu_B\frac{bj_x}{\varepsilon_\mathrm{F}^3}\sin\theta\right), \tag{6.104}$$

and its symmetric and antisymmetric components

$$\mathrm{QMR} = 7\tilde{\lambda}^2\xi(\tilde{\lambda})\frac{(g\mu_B)^2}{\varepsilon_\mathrm{F}^2}b^2\left(\frac{1}{2}+4\cos^2\theta\right), \tag{6.105}$$

$$\mathrm{BMR} = 14\tilde{\lambda}^2\xi(\tilde{\lambda})\frac{h}{e}vg\mu_B\frac{bj_x}{\varepsilon_\mathrm{F}^3}\sin\theta. \tag{6.106}$$

We can also define the amplitudes of BMR and QMR

$$A_\mathrm{QMR} = 28\tilde{\lambda}^2\xi(\tilde{\lambda})(q\mu_B)^2\frac{b^2}{\varepsilon_\mathrm{F}^2}, \tag{6.107}$$

$$A_\mathrm{BMR} = 14\tilde{\lambda}^2\xi(\tilde{\lambda})vg\mu_B\frac{h}{|e|}\frac{bj_x}{\varepsilon_\mathrm{F}^3}. \tag{6.108}$$

The ratio of BMR and QMR amplitudes has a simple form

$$\frac{A_\mathrm{BMR}}{A_\mathrm{QMR}} := \Lambda = \frac{1}{2}\frac{h}{|e|g\mu_B}\frac{1}{k_\mathrm{F}}\frac{j}{b}. \tag{6.109}$$

This ratio is useful and universal quantity for experiments, because, apart from the experimentally controlled variables b and j, it depends only on universal constants and the ratio $v/\varepsilon_\mathrm{F} = 1/k_\mathrm{F}$ that defines the Fermi wavevector k_F. As can be seen from the equation, this ratio does not depend on the relaxation time or $\tilde{\lambda}$.

To describe the planar Hall effect (PHE) in our system, it is good to define the planar Hall angle. The planar Hall angle in the lowest order with respect to $\tilde{\lambda}$ is defined as $\Theta_\mathrm{PH} = \sigma_\mathrm{PH}/\sigma_0$ and can be divided by the symmetric and antisymmetric parts, regarding the charge current flow direction. That is $\Theta_\mathrm{PH} = \Theta_\mathrm{PH}^\mathrm{S} + \Theta_\mathrm{PH}^\mathrm{AS}$, where $\Theta_\mathrm{PH}^\mathrm{S} = \left(\Theta_\mathrm{PH}(j_\alpha)+\Theta_\mathrm{PH}(-j_\alpha)\right)/2$ and

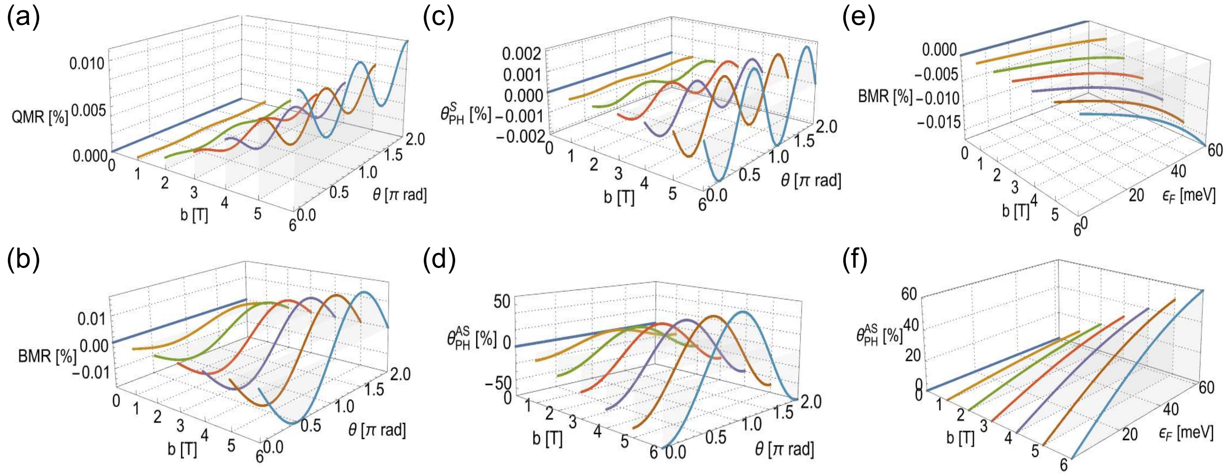

Figure 6.6: (a), (b) Quadratic and bilinear magnetoresistance (QMR, BMR) as well as (c), (d) symmetric and antisymmetric parts of the planar Hall angle ($\Theta_{\rm PH}^{\rm S}$, $\Theta_{\rm PH}^{\rm AS}$) as a function of angle θ defining the orientation of in-plane magnetic field with respect to x-direction. (e), (f) BMR and $\Theta_{\rm PH}^{\rm AS}$ as a function of the Fermi energy $\varepsilon_{\rm F}$ and amplitude of magnetic field b for $\theta = \pi/2$ and $\theta = \pi$, respectively. The other parameters, if not indicated, are as follows: $j_x = 4\,{\rm A/m}$, $\varepsilon_{\rm F} = 60\,{\rm meV}$, $\lambda = 8\,{\rm nm}^2$, $n_i V_0^2 = 1.58 \times 10^{-24}\,{\rm eV}^2{\rm m}^2$ [243].

$\Theta_{\rm PH}^{\rm AS} = \left(\Theta_{\rm PH}(j_\alpha) - \Theta_{\rm PH}(-j_\alpha)\right)/2$. Thus, the symmetric and antisymmetric parts of the planar Hall angle take form

$$\Theta_{\rm PH}^{\rm S} = \frac{\kappa(\tilde{\lambda})}{\varepsilon_{\rm F}^2}(\mathbf{j}\cdot\mathbf{B})(\mathbf{B}\times\mathbf{j})\cdot\hat{\mathbf{z}}, \tag{6.110}$$

$$\Theta_{\rm PH}^{\rm AS} = 2\frac{\kappa(\tilde{\lambda})}{\varepsilon_{\rm F}^3}\frac{vh}{e}\mathbf{j}\cdot\mathbf{B}. \tag{6.111}$$

The amplitude of the ratio of the symmetric and antisymmetric parts takes the form

$$\frac{A_{\Theta_{\rm PH}^{\rm AS}}}{A_{\Theta_{PH}^{\rm S}}} := R = 4\frac{h}{|e|g\mu_B}\frac{1}{k_{\rm F}}\frac{j}{b}. \tag{6.112}$$

Interestingly, the ratio of $R/\Lambda = 8 = const$. In turn, comparing expressions for $A_{\Theta_{\rm PH}^{\rm AS}}$ and $A_{\rm BMR}$ one finds

$$\frac{A_{\Theta_{\rm PH}^{\rm AS}}}{A_{\rm BMR}} = \frac{6}{7}\frac{1+\frac{2}{3}\tilde{\lambda}}{(1+2\tilde{\lambda}+\frac{3}{4}\tilde{\lambda}^2)^2}. \tag{6.113}$$

This relation depends only on $\tilde{\lambda}$, thus their experimental determination allows for determining $\tilde{\lambda}$. When $\tilde{\lambda}$ and $k_{\rm F}$ (determined, i.e., from Eq. 6.109) are known the SOC constant, λ, can be determined.

Fig. 6.6 presents the general behaviour of BMR, QMR, $\Theta_{\rm PH}^{\rm S}$ and $\Theta_{\rm PH}^{\rm AS}$ as a function of the amplitude of the in-plane magnetic field, angle θ (an angle between charge current density and magnetic field), and Fermi energy, $\varepsilon_{\rm F}$. Figs. 6.6(a)-(d) reflects the symmetric with respect to b dependence of QMR and $\Theta_{\rm PH}^{\rm S}$, as well as antisymmetric (i.e., unidirectional behaviour)

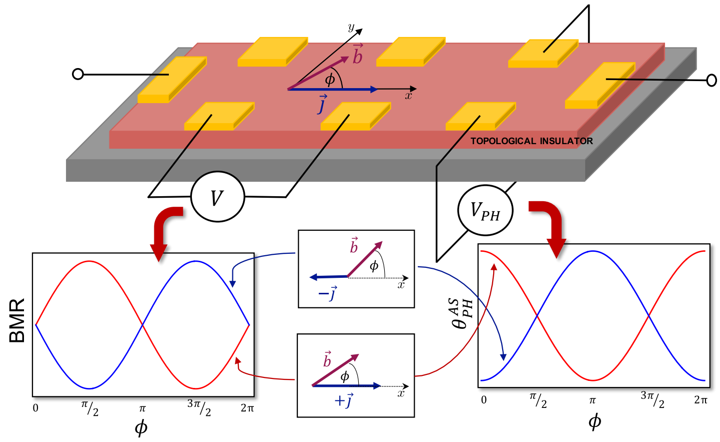

Figure 6.7: Schematic picture of measurement of the longitudinal, V, and transverse, V_{PH}, voltage. The antisymmetric part of the signals determines the bilinear magnetoresistance (BMR) and nonlinear planar Hall effect (NPHE) [243].

with respect to b dependence of BMR and $\Theta_{\mathrm{PH}}^{\mathrm{AS}}$. Moreover, the antisymmetric components of magnetoresistance and planar Hall angle have the periodicity 2π, whereas their symmetric components have the periodicity π. Figs. 6.6(e)-(f) show that, in general, both the absolute values of BMR and $\Theta_{\mathrm{PH}}^{\mathrm{AS}}$ increase with $|\varepsilon_{\mathrm{F}}|$, however, their explicit dependence on Fermi energy is determined by the functions $\xi(\tilde{\lambda})$ and $\kappa(\tilde{\lambda})$, respectively [7, 11, 243].

Both BMR and the bilinear part of planar Hall conductivity can be useful in spintronics applications, as well as a tool for the determination of the Fermi wave vector (energy) or material constants related to the strength of SO interaction. They can be measured during one transport experiment under a rotating in-plane magnetic field, as presented in Fig. 6.7.

It should be stressed that the full theoretical description of the bilinear system response needs further expansion of Green's function with respect to the external electric field, similarly to that done recently by Parker et al. [247] and Du et al. [248]. Also, it can be done by expansion of the distribution function with respect to external electric field, as developed by Zhang and Vignale [11, 204]. This formal analysis provides additional contributions to the bilinear magnetotransport, that in general can coexists and interplay with the mechanism that we have described and discussed. Importantly, the mechanism proposed here explains the bilinear magnetotransport in systems with isotropic Fermi contours in contrast to the theory of Zhang and Vignale that needs anisotropic Fermi contours (e.g., hexagonal warping term) to obtain a nonzero BMR, that was discussed in Sections 3.3 and 4.2.

Chapter 7

Conclusions

This PhD thesis focuses on the theory of bilinear magnetoresistance and the nonlinear planar Hall effect in the surface states of three-dimensional topological insulators with an isotropic Fermi contour. Both effects arise in systems with strong spin-orbit coupling and are very promising for controlling spin currents and magnetic responses in spintronic devices.

The thesis begins with an in-depth study of topological insulators in Section 2.1, materials that exhibit insulating behavior in their bulk while revealing topologically protected conducting states on their surfaces. These surface states are characterized by spin-momentum locking, which makes them promising candidates for spintronic devices. Starting from a detailed analysis of spin-orbit coupling, the Rashba effect, and current-induced spin polarization (Edelstein effect) in Sections 2.2 and 2.3, the thesis provides a review of the most important phenomena for today's spintronics, with particular emphasis on various kinds of Hall effects in Section 2.4, magnetoresistance effects in Chapter 3, and planar Hall effect in Chapter 4.

The key original contribution of this work is the formulation of the theory of bilinear magnetoresistance and the nonlinear planar Hall effect of surface states of three-dimensional topological insulators, presented in Chapter 6. These phenomena are discussed in the case of systems with isotropic Fermi contour, performing calculations in the so called "bare bubble" approximation, in Section 6.2, and considering the vertex correction in the ladder approximation, as presented in Section 6.3. For this case, the hexagonal warping is absent, and the Zhang-Vignale mechanism leading to the magnetoelectric magnetotransport response does not occur. However, due to the strong nonequilibrium spin polarization (Edelstein effect), the conduction electrons experience an effective spin-orbital field that adds to the external in-plane magnetic field and results in linear to charge current density and to magnetic field (i.e., socalled bilinear or unidirectional) contribution to the magnetoresistance and planar Hall effect. Using the Green's function formalism and diagrammatic technique, principles of which were considered in Chapter 5, all components of the conductivity tensor have been determined, taking into account both single-loop and side-jump diagrams. In the leading terms to the spin-orbit coupling constant, we derived general expressions for the arbitrary orientation of charge current density and magnetic field. These equations allowed us to determine the symmetric and antisymmetric (i.e., linear and nonlinear) to the charge current density contributions to the magnetoresistance and planar Hall effect, i.e., bilinear magnetoresistance and antisymmetric part to planar Hall angle, respectively. The expressions describing the amplitudes of bilinear and quadratic magnetoresistance have been derived, as well as symmetric and antisymmetric planar Hall angles. In Sections 6.2 and 6.3 relations between magnetoresistance and planar Hall angle have been derived. The mechanism discussed in the thesis is based on the interplay of a nonequilibrium effective spin-orbital field due to current-induced spin polarization and momentum-dependent scattering on spin-orbital impurities.

The presented mechanism is one of the various possible mechanisms that can appear in real materials and lead to the bilinear system response. However, the proposed mechanism seems to be especially important in systems with isotropic Fermi contours or close to the Dirac-like crossing points. It has been shown that, in our approach, the side-jump contribution is rather small, whereas the skew-scattering has not been considered, as we have assumed Gaussian disorder distribution. It should be noted that recently it has been shown that the skew-scattering in cooperation with Berry curvature contribution can be an essential mechanism leading to the nonlinear Hall effect in $\mathcal{PT}-$symmetric antiferromagnets [249]. The results obtained in this thesis may be useful in the experimental determination of the material constants such as the Fermi wave vector (or Fermi velocity) and spin-orbit coupling parameter.

Chapter 8

List of Abbreviations

2D – two-dimensional
2DEG – two-dimensional electron gas
3D – three-dimensional
AC – alternating current
AHE – anomalous Hall effect
AMR – anisotropic magnetoresistance
ARPES – angle resolved photoemission spectroscopy
BIA – bulk inversion asymmetry
BMR (BMER) – bilinear magnetoresistance (bilinear magnetoelectric resistance)
BST – $Bi_{2-x}Sb_xTe_3$
CISP – current-induced spin polarization
CMR – colossal magnetoresistance
DC – direct current
DEE – direct Edelstein effect
EE – Edelstein effect
FI – ferromagnetic insulator
GMR – giant magnetoresistance
HDD – hard disk drive
ISB – inversion symmetry breaking
MBE – molecular beam epitaxy
MR – magnetoresistance
MRAM – magnetic random access memories
MTJ – magnetic tunnel junction
NM – non-magnetic; normal metal
NPHE – nonlinear planar Hall effect
OMM – orbital magnetic moment
OMR – ordinary magnetoresistance
PHE – planar Hall effect
SHE – spin Hall effect
SIA – structural inversion asymmetry
SMR – spin Hall magnetoresistance
SO – spin-orbital
SOC – spin-orbit coupling
TI – topological insulator
TMD – transition metal dichalcogenides
TMR – tunneling magnetoresistance
TRS – time-reversal symmetry
TSSs – topological surface states
UMR – unidirectional magnetoresistance

Chapter 9

List of Publications

[1] M. Tkach, O. Pytiuk, J. Seti, O. Voitsekhivska, K. Boboshko, and V. Hutiv. *Main, excited and hybrid states of the system of localized two-level quasi-particle interacting with polarization phonons at cryogenic temperature.* In Proceedings, 2017 IEEE 7th International Conference Nanomaterials: Application & Properties (NAP), pages 03NE03-1–03NE03-4, IEEE, (2017).

[2] I. Gudyma, K. Boboshko, and K. Boukheddaden. *Reentrant behavior of magnetic ordered phase in spin-crossover solids with quenched disordered ligand field.* Phys. Lett. A, 384(26):126677, (2020).

[3] K. Boboshko, A. Dyrdał, and J. Barnaś. *Bilinear magnetoresistance in topological insulators: The role of spin-orbit scattering on impurities.* J. Magn. Magn. Mater., 545:168698, (2022).

[4] K. Boboshko, and A. Dyrdał. *Bilinear magnetoresistance and planar Hall effect in topological insulators: Interplay of scattering on spin-orbital impurities and nonequilibrium spin polarization.* Phys. Rev. B, 109(15):155420, (2024).

Chapter 10

List of Publications Being the Basis of the Thesis

[1] K. Boboshko, A. Dyrdał, and J. Barnaś. *Bilinear magnetoresistance in topological insulators: The role of spin-orbit scattering on impurities.* J. Magn. Magn. Mater., 545:168698, (2022).

[2] K. Boboshko, and A. Dyrdał. *Bilinear magnetoresistance and planar Hall effect in topological insulators: Interplay of scattering on spin-orbital impurities and nonequilibrium spin polarization.* Phys. Rev. B, 109(15):155420, (2024).

Chapter 11

Statements of the Authors

Oświadczenie doktoranta opisujące własny merytoryczny wkład w powstanie pracy

Poznań, 27.09.2024r.

Kateryna Boboshko
Zakład Fizyki Mezoskopowej,
Instytut Spintroniki i Informacji Kwantowej
Wydział Fizyki i Astronomii UAM

Oświadczenie

Oświadczam, że w pracach:

1) Boboshko, K., & Dyrdał, A. (2024). Bilinear magnetoresistance and planar Hall effect in topological insulators: Interplay of scattering on spin-orbital impurities and nonequilibrium spin polarization. *Physical Review B*, 109, 155420;
2) Boboshko, K., Dyrdał, A., & Barnaś, J. (2022). Bilinear magnetoresistance in topological insulators: The role of spin-orbit scattering on impurities. *Journal of Magnetism and Magnetic Materials*, 545, 168698;

mój udział polegał w wykonywaniu obliczeń analitycznych i numerycznych, przygotowaniu wykresów, wstępnej analizie danych oraz przygotowaniu wstępnych wersji manuskryptów.

A. Dyrdał
....
podpis promotora

Boboshko
....
podpis doktoranta

UNIWERSYTET IM. ADAMA MICKIEWICZA W POZNANIU
Wydział Fizyki

Poznań, 27 września 2024 r.

Prof. UAM dr hab. Anna Dyrdał
Zakład Fizyki Mezoskopowej
Instytut Spintroniki i Informacji Kwantowej,
Wydział Fizyki i Astronomii,
Uniwersytet im. A. Mickiewicza w Poznaniu

Oświadczenie

Oświadczam, że w poniższych publikacjach

1) K. Boboshko and A. Dyrdał, *Bilinear magnetoresistance and planar Hall effect in topological insulators: Interplay of scattering on spin-orbital impurities and nonequilibrium spin polarization*, Physical Review B 109, 155420 (2024)
2) K. Boboshko, A. Dyrdał, J. Barnaś, *Bilinear magnetoresistance in topological insulators: The role of spin-orbit scattering on impurities*, Journal of Magnetism and Magnetic Materials 545, 168698 (2022)

mój wkład w ich powstanie polegał na sformułowaniu zagadnienia, zaproponowaniu metody obliczeniowej, sprawowaniu merytorycznej opieki nad obliczeniami Pani Boboshko, sprawdzeniu części wyników, analizie i interpretacji wyników oraz redakcji manuskryptu.

Anna Dyrdał
A. Dy

ul. H. Wieniawskiego 1, 61-712 Poznań
tel. +48 61 829 00 00, fax +48 61 829 00 00
adres.email@amu.edu.pl

Poznań, 27.09.2024

Prof. dr hab. Józef Barnaś
Zakład Fizyki Mezoskopowej,
Wydział Fizyki i Astronomii,
Uniwersytet im. Adama Mickiewicza
w Poznaniu

Oświadczenie

Oświadczam, że w publikacji
K. Boboshko, A. Dyrdał, J. Barnaś, Bilinear magnetoresistance in topological insulators: The role of spin–orbit scattering on impurities, Journal of Magnetism and Magnetic Materials 545 (2022) 168698,
mój udział polegał na dyskusji na etapie formułowania problemu, oraz pomocy w interpretacji wyników numerycznych i w redakcji końcowej wersji manuskryptu.

Józef Barnaś

Bibliography

[1] A. Fert and F. N. Van Dau. Spintronics, from giant magnetoresistance to magnetic skyrmions and topological insulators. *C. R. Phys.*, 20(7):817–831, (2019).

[2] Y. Chen, Y. Xie, X. Yan, M. L. Cohen, and S. Zhang. Topological carbon materials: A new perspective. *Phys. Rep.*, 868:1–32, (2020).

[3] M. Z. Hasan and C. L. Kane. Colloquium: Topological insulators. *Rev. Mod. Phys.*, 82(4):3045–3067, (2010).

[4] G. Tkachov. *Topological Insulators: The Physics of Spin Helicity in Quantum Transport*. Taylor & Francis, (2015).

[5] A. Manchon, H. C. Koo, J. Nitta, S. M. Frolov, and R. A. Duine. New perspectives for Rashba spin-orbit coupling. *Nat. Mater.*, 14(9):871–882, (2015).

[6] H. Gu, X. Zhang, H. Wei, Y. Huang, S. Wei, and Z. Guo. An overview of the magnetoresistance phenomenon in molecular systems. *Chem. Soc. Rev.*, 42(13):5907–5943, (2013).

[7] A. Dyrdał, J. Barnaś, and A. Fert. Spin-momentum-locking inhomogeneities as a source of bilinear magnetoresistance in topological insulators. *Phys. Rev. Lett.*, 124:046802, (2020).

[8] P. He, S. S. L. Zhang, D. Zhu, Y. Liu, Y. Wang, J. Yu, G. Vignale, and H. Yang. Bilinear magnetoelectric resistance as a probe of three-dimensional spin texture in topological surface states. *Nature Physics*, 14(5):495–499, (2018).

[9] J. Zhong, J. Zhuang, and Y. Du. Recent progress on the planar Hall effect in quantum materials. *Chin. Phys. B*, 32(4):047203, (2023).

[10] A. A. Taskin, H. F. Legg, F. Yang, S. Sasaki, Y. Kanai, K. Matsumoto, A. Rosch, and Y. Ando. Planar Hall effect from the surface of topological insulators. *Nat. Commun.*, 8(1340):1–7, (2017).

[11] P. He, S. S.-L. Zhang, D. Zhu, S. Shi, O. G. Heinonen, G. Vignale, and H. Yang. Nonlinear planar Hall effect. *Phys. Rev. Lett.*, 123(1):016801, (2019).

[12] C. L. Kane and E. J. Mele. Quantum spin Hall effect in graphene. *Phys. Rev. Lett.*, 95(22):226801, (2005).

[13] B. A. Bernevig and S.-C. Zhang. Quantum spin Hall effect. *Phys. Rev. Lett.*, 96(10):106802, (2006).

[14] L. Fu, C. L. Kane, and E. J. Mele. Topological insulators in three dimensions. *Phys. Rev. Lett.*, 98(10):106803, (2007).

[15] J. E. Moore and L. Balents. Topological invariants of time-reversal-invariant band structures. *Phys. Rev. B*, 75(12):121306, (2007).

[16] M. König, S. Wiedmann, C. Brüne, A. Roth, H. Buhmann, L. W. Molenkamp, X.-L. Qi, and S.-C. Zhang. Quantum spin Hall insulator state in HgTe quantum wells. *Science*, 318(5851):766–770, (2007).

[17] Y. Wang, R. Ramaswamy, and H. Yang. FMR-related phenomena in spintronic devices. *J. Phys. D: Appl. Phys.*, 51(27):273002, (2018).

[18] Y. Ando. Topological insulator materials. *J. Phys. Soc. Jpn.*, 82(10):102001, (2013).

[19] F. Bussolotti, D. Chi, K. E. J. Goh, Y. L. Huang, and A. T. S. Wee. STM/STS and ARPES characterization-structure and electronic properties. In *2D Semiconductor Materials and Devices*, pages 199–220. Elsevier, Walthm, MA, USA, (2020).

[20] D. Culcer, A. C. Keser, Y. Li, and G. Tkachov. Transport in two-dimensional topological materials: Recent developments in experiment and theory. *2D Mater.*, 7(2):022007, (2020).

[21] R. Winkler. Spin-orbit coupling in solids. In *Encyclopedia of Condensed Matter Physics (Second Edition)*, volume 2, pages 186–192. Academic Press, Cambridge, MA, USA, (2024).

[22] J. Xia, W. Ge, and K. Chang. *Semiconductor Spintronics*. World Scientific Publishing Company, (2011).

[23] G. Dresselhaus. Spin-orbit coupling effects in zinc blende structures. *Phys. Rev.*, 100(2):580–586, (1955).

[24] J. Nitta. Spin-orbit interaction based spintronics. In *Encyclopedia of Condensed Matter Physics (Second Edition)*, volume 2, pages 193–204. Academic Press, Cambridge, MA, USA, (2024).

[25] E. I. Rashba and V. I. Sheka. Symmetry of energy bands in crystals of wurtzite type: II. Symmetry of bands including spin-orbit interaction. *Fiz. Tverd. Tela: Collected Papers*, 2:162–176, (1959).

[26] F. T. Vas'ko. Spin splitting in the spectrum of two-dimensional electrons due to the surface potential. *JETP Lett.*, 30:574–577, (1979).

[27] Yu. A. Bychkov and E. I. Rashba. Properties of a 2D electron gas with lifted spectral degeneracy. *JETP Lett.*, 39:66–69, (1984).

[28] K. V. Shanavas. Overview of theoretical studies of Rashba effect in polar perovskite surfaces. *J. Electron Spectrosc. Relat. Phenom.*, 201:121–126, (2015).

[29] V. Litvinov. *Magnetism in Topological Insulators*. Springer International Publishing, (2019).

[30] G. Bihlmayer, P. Noël, D. V. Vyalikh, E. V. Chulkov, and A. Manchon. Rashba-like physics in condensed matter. *Nat. Rev. Phys.*, 4(10):642–659, (2022).

[31] W. Han, R. K. Kawakami, M. Gmitra, and J. Fabian. Graphene spintronics. *Nat. Nanotechnol.*, 9(10):794–807, (2014).

[32] L. E. F. F. Torres, S. Roche, and J.-C. Charlier. *Introduction to Graphene-Based Nanomaterials: From Electronic Structure to Quantum Transport*. Cambridge University Press, (2014).

[33] P. D. C. King, R. C. Hatch, M. Bianchi, R. Ovsyannikov, C. Lupulescu, G. Landolt, B. Slomski, J. H. Dil, D. Guan, J. L. Mi, E. D. L. Rienks, J. Fink, A. Lindblad, S. Svensson, S. Bao, G. Balakrishnan, B. B. Iversen, J. Osterwalder, W. Eberhardt, F. Baumberger, and Ph. Hofmann. Large tunable rashba spin splitting of a two-dimensional electron gas in Bi_2Se_3. *Phys. Rev. Lett.*, 107(9):096802, (2011).

[34] H. Isshiki, P. Muduli, J. Kim, K. Kondou, and Y. Otani. Phenomenological model for the direct and inverse Edelstein effects. *Phys. Rev. B*, 102(18):184411, (2020).

[35] K. Vaklinova, A. Hoyer, M. Burghard, and K. Kern. Current-induced spin polarization in topological insulator-graphene heterostructures. *Nano Lett.*, 16(4):2595–2602, (2016).

[36] S. D. Ganichev, E. L. Ivchenko, V. V. Bel'kov, S. A. Tarasenko, M. Sollinger, D. Weiss, W. Wegscheider, and W. Prettl. Spin-galvanic effect. *Nature*, 417(6885):153–156, (2002).

[37] V. M. Edelstein. Spin polarization of conduction electrons induced by electric current in two-dimensional asymmetric electron systems. *Solid State Commun.*, 73(3):233–235, (1990).

[38] A. G. Aronov and Yu. B. Lyanda-Geller. Nuclear electric resonance and orientation of carrier spins by an electric field. *JETP Lett.*, 50:398, (1989).

[39] M. I. D'yakonov and V. I. Perel'. Current-induced spin orientation of electrons in semiconductors. *Phys. Lett. A*, 35(6):459–460, (1971).

[40] Y. K. Kato, R. C. Myers, A. C. Gossard, and D. D. Awschalom. Current-induced spin polarization in strained semiconductors. *Phys. Rev. Lett.*, 93(17):176601, (2004).

[41] D. C. Vaz, P. Noël, A. Johansson, B. Göbel, F. Y. Bruno, G. Singh, S. McKeown-Walker, F. Trier, L. M. Vicente-Arche, A. Sander, S. Valencia, P. Bruneel, M. Vivek, M. Gabay, N. Bergeal, F. Baumberger, H. Okuno, A. Barthélémy, A. Fert, L. Vila, I. Mertig, J.-P. Attané, and M. Bibes. Mapping spin-charge conversion to the band structure in a topological oxide two-dimensional electron gas - Nature Materials. *Nat. Mater.*, 18(11):1187–1193, (2019).

[42] J. Sinova, S. O. Valenzuela, J. Wunderlich, C. H. Back, and T. Jungwirth. Spin Hall effects. *Rev. Mod. Phys.*, 87(4):1213–1260, (2015).

[43] H. J. Zhang, S. Yamamoto, B. Gu, H. Li, M. Maekawa, Y. Fukaya, and A. Kawasuso. Charge-to-spin conversion and spin diffusion in Bi/Ag bilayers observed by spin-polarized positron beam. *Phys. Rev. Lett.*, 114(16):166602, (2015).

[44] P. Li, W. Wu, Y. Wen, C. Zhang, J. Zhang, S. Zhang, Z. Yu, S. A. Yang, A. Manchon, and X. Zhang. Spin-momentum locking and spin-orbit torques in magnetic nano-heterojunctions composed of Weyl semimetal WTe2. *Nat. Commun.*, 9(3990):1–10, (2018).

[45] S. Zhang and A. Fert. Conversion between spin and charge currents with topological insulators. *Phys. Rev. B*, 94(18):184423, (2016).

[46] K. Kondou, R. Yoshimi, A. Tsukazaki, Y. Fukuma, J. Matsuno, K. S. Takahashi, M. Kawasaki, Y. Tokura, and Y. Otani. Fermi-level-dependent charge-to-spin current conversion by Dirac surface states of topological insulators. *Nat. Phys.*, 12(11):1027–1031, (2016).

[47] A. Dyrdał and J. Barnaś. Current-induced spin polarization and spin-orbit torque in graphene. *Phys. Rev. B*, 92(16):165404, (2015).

[48] J. Ryu, S. Lee, K.-J. Lee, and B.-G. Park. Current-induced spin-orbit torques for spintronic applications. *Adv. Mater.*, 32(35):1907148, (2020).

[49] A. Karsenty. A comprehensive review of integrated Hall effects in macro-, micro-, nanoscales, and quantum devices. *Sensors*, 20(15):4163, (2020).

[50] N. Nagaosa, J. Sinova, S. Onoda, A. H. MacDonald, and N. P. Ong. Anomalous Hall effect. *Rev. Mod. Phys.*, 82(2):1539–1592, (2010).

[51] E. H. Hall. On a new action of the magnet on electric currents. *American Journal of Mathematics*, 2(3):287–292, (1879).

[52] G. S. Leadstone. The discovery of the Hall effect. *Phys. Educ.*, 14(6):374, (1979).

[53] J. A. Gaj. Semimagnetic semiconductors. In *Comprehensive Semiconductor Science and Technology*, volume 2, pages 95–124. Elsevier, (2011).

[54] S. Zhang, R. Wang, X. Wang, B. Wei, B. Chen, H. Wang, G. Shi, F. Wang, B. Jia, Y. Ouyang, F. Xie, F. Fei, M. Zhang, X. Wang, D. Wu, X. Wan, F. Song, H. Zhang, and B. Wang. Experimental observation of the gate-controlled reversal of the anomalous Hall effect in the intrinsic magnetic topological insulator $MnBi_2Te_4$ Device. *Nano Lett.*, 20(1):709–714, (2020).

[55] M. Mogi, T. Nakajima, V. Ukleev, A. Tsukazaki, R. Yoshimi, M. Kawamura, K. S. Takahashi, T. Hanashima, K. Kakurai, T. Arima, M. Kawasaki, and Y. Tokura. Large anomalous Hall effect in topological insulators with proximitized ferromagnetic insulators. *Phys. Rev. Lett.*, 123(1):016804, (2019).

[56] H.-D. Song, P.-F. Zhu, J. Fang, Z. Zhou, H. Yang, K. Wang, J. Li, D. Yu, Z. Wei, and Z.-M. Liao. Anomalous Hall effect in graphene coupled to a layered magnetic semiconductor. *Phys. Rev. B*, 103(12):125304, (2021).

[57] R. Karplus and J. M. Luttinger. Hall effect in ferromagnetics. *Phys. Rev.*, 95(5):1154–1160, (1954).

[58] T. S. Nunner, N. A. Sinitsyn, M. F. Borunda, V. K. Dugaev, A. A. Kovalev, Ar. Abanov, C. Timm, T. Jungwirth, J. Inoue, A. H. MacDonald, and J. Sinova. Anomalous Hall effect in a two-dimensional electron gas. *Phys. Rev. B*, 76(23):235312, (2007).

[59] J. Smit. The spontaneous Hall effect in ferromagnetics I. *Physica*, 21(6):877–887, (1955).

[60] L. Berger. Side-jump mechanism for the Hall effect of ferromagnets. *Phys. Rev. B*, 2(11):4559–4566, (1970).

[61] Á. Gutiérrez-Rubio, L. Chirolli, L. Martín-Moreno, F. J. García-Vidal, and F. Guinea. Polariton anomalous Hall effect in transition-metal dichalcogenides. *Phys. Rev. Lett.*, 121(13):137402, (2018).

[62] Y. Pu, D. Chiba, F. Matsukura, H. Ohno, and J. Shi. Mott relation for anomalous Hall and Nernst effects in $\mathrm{Ga}_{1-x}\mathrm{Mn}_x\mathrm{As}$ ferromagnetic semiconductors. *Phys. Rev. Lett.*, 101(11):117208, (2008).

[63] H. J. Trodahl, F. Natali, B. J. Ruck, and W. R. L. Lambrecht. Carrier-controlled anomalous Hall effect in an intrinsic ferromagnetic semiconductor. *Phys. Rev. B*, 96(11):115309, (2017).

[64] A. Husmann and L. J. Singh. Temperature dependence of the anomalous Hall conductivity in the Heusler alloy $\mathrm{Co_2CrAl}$. *Phys. Rev. B*, 73(17):172417, (2006).

[65] S. Roy, R. Singha, A. Ghosh, A. Pariari, and P. Mandal. Anomalous Hall effect in the half-metallic Heusler compound $\mathrm{Co_2Ti}X$ ($X = \mathrm{Si}$, Ge). *Phys. Rev. B*, 102(8):085147, (2020).

[66] Y. Omori, E. Sagasta, Y. Niimi, M. Gradhand, L. E. Hueso, F. Casanova, and Y. Otani. Relation between spin Hall effect and anomalous Hall effect in $3d$ ferromagnetic metals. *Phys. Rev. B*, 99(1):014403, (2019).

[67] N. A. Sinitsyn. Semiclassical theories of the anomalous Hall effect. *J. Phys.: Condens. Matter*, 20(2):023201, (2007).

[68] M. I. D'yakonov and V. I. Perel'. Possibility of orienting electron spins with current. *JETP Lett.*, 13:467, (1971).

[69] J. E. Hirsch. Spin Hall effect. *Phys. Rev. Lett.*, 83(9):1834–1837, (1999).

[70] H.-A. Engel, E. I. Rashba, and B. I. Halperin. Theory of spin Hall effects in semiconductors. In *Handbook of Magnetism and Advanced Magnetic Materials*. John Wiley & Sons, Ltd, (2007).

[71] G. Vignale. Ten years of spin Hall effect. *J. Supercond. Novel Magn.*, 23(1):3–10, (2010).

[72] A. Dyrdał, V. K. Dugaev, and J. Barnaś. Spin Hall effect in a system of Dirac fermions in the honeycomb lattice with intrinsic and Rashba spin-orbit interaction. *Phys. Rev. B*, 80(15):155444, (2009).

[73] C. Sun, J. Deng, S. M. Rafi-Ul-Islam, G. Liang, H. Yang, and M. B. A. Jalil. Field-free switching of perpendicular magnetization through spin Hall and anomalous Hall effects in ferromagnet–heavy-metal–ferromagnet structures. *Phys. Rev. Appl.*, 12(3):034022, (2019).

[74] P. Seifert, K. Vaklinova, S. Ganichev, K. Kern, M. Burghard, and A. W. Holleitner. Spin Hall photoconductance in a three-dimensional topological insulator at room temperature. *Nat. Commun.*, 9(331):1–7, (2018).

[75] P. N. Hai. Spin Hall effect in topological insulators. *J. Magn. Soc. Jpn.*, 44(6):137–144, (2020).

[76] A. Dyrdał and J. Barnaś. Spin Hall effect in graphene due to random Rashba field. *Phys. Rev. B*, 86(16):161401, (2012).

[77] C. K. Safeer, J. Ingla-Aynés, F. Herling, J. H. Garcia, M. Vila, N. Ontoso, M. R. Calvo, S. Roche, L. E. Hueso, and F. Casanova. Room-temperature spin Hall effect in graphene/MoS2 van der Waals heterostructures. *Nano Lett.*, 19(2):1074–1082, (2019).

[78] Y. K. Kato, R. C. Myers, A. C. Gossard, and D. D. Awschalom. Observation of the spin Hall effect in semiconductors. *Science*, 306(5703):1910–1913, (2004).

[79] A. A. Bakun, B. P. Zakharchenya, A. A. Rogachev, M. N. Tkachuk, and V. G. Fleisher. Observation of a surface photocurrent caused by optical orientation of electrons in a semiconductor. *JETP Lett.*, 40:464, (1984).

[80] E. Saitoh, M. Ueda, H. Miyajima, and G. Tatara. Conversion of spin current into charge current at room temperature: Inverse spin-Hall effect. *Appl. Phys. Lett.*, 88(18), (2006).

[81] C.-Z. Chang and M. Li. Quantum anomalous Hall effect in time-reversal-symmetry breaking topological insulators. *J. Phys.: Condens. Matter*, 28(12):123002, (2016).

[82] K. von Klitzing, G. Dorda, and M. Pepper. New method for high-accuracy determination of the fine-structure constant based on quantized Hall resistance. *Phys. Rev. Lett.*, 45(6):494–497, (1980).

[83] K. von Klitzing, T. Chakraborty, P. Kim, V. Madhavan, X. Dai, J. McIver, Y. Tokura, L. Savary, D. Smirnova, A. M. Rey, C. Felser, J. Gooth, and X. Qi. 40 years of the quantum Hall effect. *Nat. Rev. Phys.*, 2(8):397–401, (2020).

[84] J. Maciejko, T. L. Hughes, and S.-C. Zhang. The quantum spin Hall effect. *Annu. Rev. Condens. Matter Phys.*, 2:31–53, (2011).

[85] F. D. M. Haldane. Model for a quantum Hall effect without Landau levels: Condensed-matter realization of the "parity anomaly". *Phys. Rev. Lett.*, 61(18):2015–2018, (1988).

[86] C.-Z. Chang, J. Zhang, X. Feng, J. Shen, Z. Zhang, M. Guo, K. Li, Y. Ou, P. Wei, L.-L. Wang, Z.-Q. Ji, Y. Feng, S. Ji, X. Chen, J. Jia, X. Dai, Z. Fang, S.-C. Zhang, K. He, Y. Wang, L. Lu, X.-C. Ma, and Q.-K. Xue. Experimental observation of the quantum anomalous Hall effect in a magnetic topological insulator. *Science*, 340(6129):167–170, (2013).

[87] C.-Z. Chang, C.-X. Liu, and A. H. MacDonald. Colloquium: Quantum anomalous Hall effect. *Rev. Mod. Phys.*, 95(1):011002, (2023).

[88] Z. Qiao, H. Jiang, X. Li, Y. Yao, and Q. Niu. Microscopic theory of quantum anomalous Hall effect in graphene. *Phys. Rev. B*, 85(11):115439, (2012).

[89] S.-Q. Shen. Quantum anomalous Hall effect and quantum spin Hall effect. In *Topological insulators: Dirac equation in condensed matter*, chapter 6, pages 91–123. Springer, (2017).

[90] R. Niu and W. K. Zhu. Materials and possible mechanisms of extremely large magnetoresistance: a review. *J. Phys.: Condens. Matter*, 34(11):113001, (2021).

[91] Y. Hishiyama, Y. Kaburagi, and M. Inagaki. Magnetoresistance. In *Materials Science and Engineering of Carbon*, pages 173–204. Butterworth-Heinemann, (2016).

[92] N. J. Lee, H. Jang, E. Park, K.-S. Lee, S. Jeong, S. Lee, B.-G. Park, C.-Y. You, K.-W. Kim, and S. Kim. Quantitative analysis of magnon characteristics with unidirectional magnetoresistance. *Phys. Rev. Appl.*, 20(6):064006, (2023).

[93] K. Yasuda, A. Tsukazaki, R. Yoshimi, K. S. Takahashi, M. Kawasaki, and Y. Tokura. Large unidirectional magnetoresistance in a magnetic topological insulator. *Phys. Rev. Lett.*, 117(12):127202, (2016).

[94] C. O. Avci, K. Garello, A. Ghosh, M. Gabureac, S. F. Alvarado, and P. Gambardella. Unidirectional spin Hall magnetoresistance in ferromagnet/normal metal bilayers. *Nat. Phys.*, 11(7):570–575, (2015).

[95] S. S.-L. Zhang and G. Vignale. Theory of unidirectional spin Hall magnetoresistance in heavy-metal/ferromagnetic-metal bilayers. *Phys. Rev. B*, 94(14):140411, (2016).

[96] T. Shinjo. *Nanomagnetism and Spintronics*. Elsevier, (2014).

[97] T. Nie, J. Tang, X. Kou, F. Xiu, and K. L. Wang. Nanoscale engineering of Ge-based diluted magnetic semiconductors for room-temperature spintronics application. In *Molecular Beam Epitaxy (Second Edition)*, pages 403–419. Elsevier, (2018).

[98] M. Eto and H. Kamimura. Impurity bands in group-IV semiconductors. In *Comprehensive Semiconductor Science and Technology*, volume 1, pages 77–112. Elsevier, (2011).

[99] J. K. Hyun and S. Zhang. Growth of nanowire heterostructures and their optoelectronic and spintronic applications. In *Magnetic Nano- and Microwires*, pages 125–146. Woodhead Publishing, (2015).

[100] I. Shibasaki and N. Kuze. Mass production of sensors grown by MBE. In *Molecular Beam Epitaxy*, pages 697–720. Elsevier, (2013).

[101] T. William. XIX. On the electro-dynamic qualities of metals:—Effects of magnetization on the electric conductivity of nickel and of iron. *Proc. R. Soc. Lond.*, 8:546–550, (1857).

[102] G. Beck, C. Korte, J. Janek, F. Gruhl, and M. Kreutzbruck. The magnetoresistance of homogeneous and heterogeneous silver-rich silver selenide. *J. Appl. Phys.*, 96(10):5619–5624, (2004).

[103] G. Beck and J. Janek. Positive and negative magnetoresistance in the system silver–selenium. *Physica B*, 308-310:1086–1089, (2001).

[104] A. Jander, C. Smith, and R. Schneider. Magnetoresistive sensors for nondestructive evaluation. In *Proceedings Volume 5770, Advanced Sensor Technologies for Nondestructive Evaluation and Structural Health Monitoring*, volume 5770, pages 1–13. SPIE, (2005).

[105] M. Doms and R. Slatter. Magnetoresistive sensors for angle, position, and electrical current measurement in demanding environments. In *Proceedings Volume 9113, Sensors for Extreme Harsh Environments*, volume 9113, pages 143–153. SPIE, (2014).

[106] J.-P. Jan. Galvamomagnetic and thermomagnetic effects in metals. In *Solid State Physics*, volume 5, pages 1–96. Academic Press, (1957).

[107] Y. Liu, R. Yang, H. Yang, D. Wang, Q. Zhan, G. Zhang, Y. Xie, B. Chen, and R.-W. Li. Anomalous anisotropic magnetoresistance effects in graphene. *AIP Adv.*, 4(9), (2014).

[108] J. Nickel. *Magnetoresistance overview*. HPL, (1995).

[109] C.-J. Zhao, L. Ding, J.-S. HuangFu, J.-Y. Zhang, and G.-H. Yu. Research progress in anisotropic magnetoresistance. *Rare Met.*, 32(3):213–224, (2013).

[110] T. McGuire and R. Potter. Anisotropic magnetoresistance in ferromagnetic 3d alloys. *IEEE Trans. Magn.*, 11(4):1018–1038, (1975).

[111] S. Kokado and M. Tsunoda. Theoretical study on anisotropic magnetoresistance effects of arbitrary directions of current and magnetization for ferromagnets: Application to transverse anisotropic magnetoresistance effect. *J. Phys. Soc. Jpn.*, 91(4):044701, (2022).

[112] J. Meng, H. Xue, M. Liu, W. Jiang, Z. Zhang, J. Ling, L. He, R. Dou, C. Xiong, and J. Nie. Planar Hall effect induced by anisotropic orbital magnetoresistance in type-II Dirac semimetal $PdTe_2$. *J. Phys.: Condens. Matter*, 32(1):015702, (2019).

[113] S. Nandy, G. Sharma, A. Taraphder, and S. Tewari. Chiral anomaly as the origin of the planar Hall effect in Weyl semimetals. *Phys. Rev. Lett.*, 119(17):176804, (2017).

[114] T. Sato, S. Kokado, H. Shinya, M. Tsujikawa, A. Miura, S. Kosaka, T. Ogawa, M. Shirai, and M. Tsunoda. Compositional dependence of anisotropic magnetoresistance effects in Weyl semimetal Co_2MnAl Heusler alloy epitaxial thin films. *J. Appl. Phys.*, 132(22), (2022).

[115] M. Rataj and J. Barnaś. Large anisotropic magnetoresistance in graphene-based junctions. *Phys. Status Solidi RRL*, 7(11):997–1000, (2013).

[116] T. Chiba, S. Takahashi, and G. E. W. Bauer. Magnetic-proximity-induced magnetoresistance on topological insulators. *Phys. Rev. B*, 95(9):094428, (2017).

[117] S. J. Kim, Y. H. Park, C. Jang, A. Hruban, and H. C. Koo. Anisotropic magnetoresistance in a $Ni_{81}Fe_{19}/SiO_2$/Ca-Bi_2Se_3 hybrid structure. *Thin Solid Films*, 676:87–91, (2019).

[118] B. Xia, P. Ren, A. Sulaev, Z. P. Li, P. Liu, Z. L. Dong, and L. Wang. Anisotropic magnetoresistance in topological insulator $Bi_{1.5}Sb_{0.5}Te_{1.8}Se_{1.2}$/CoFe heterostructures. *AIP Adv.*, 2(4), (2012).

[119] H. Huang, J. Gu, P. Ji, Q. Wang, X. Hu, Y. Qin, J. Wang, and C. Zhang. Giant anisotropic magnetoresistance and planar Hall effect in $Sr_{0.06}Bi_2Se_3$. *Appl. Phys. Lett.*, 113(22), (2018).

[120] R. C. Budhani, J. S. Higgins, D. McAlmont, and Johnpierre Paglione. Planar Hall effect in c-axis textured films of $Bi_{85}Sb_{15}$ topological insulator. *AIP Adv.*, 11(5):055020, (2021).

[121] D. Rakhmilevich, F. Wang, W. Zhao, M. H. W. Chan, J. S. Moodera, C. Liu, and C.-Z. Chang. Unconventional planar Hall effect in exchange-coupled topological insulator–ferromagnetic insulator heterostructures. *Phys. Rev. B*, 98(9):094404, (2018).

[122] B. Wu, X.-C. Pan, W. Wu, F. Fei, B. Chen, Q. Liu, H. Bu, L. Cao, F. Song, and B. Wang. Oscillating planar Hall response in bulk crystal of topological insulator Sn doped $Bi_{1.1}Sb_{0.9}Te_2S$. *Appl. Phys. Lett.*, 113(1):011902, (2018).

[123] A. Bhardwaj, S. Prasad P., K. V. Raman, and D.T Suri. Observation of planar Hall effect in topological insulator–Bi_2Te_3. *Appl. Phys. Lett.*, 118(24):241901, (2021).

[124] T. Li, L. Zhang, and X. Hong. Anisotropic magnetoresistance and planar Hall effect in correlated and topological materials. *J. Vac. Sci. Technol., A*, 40(1), (2022).

[125] S. Wiedmann, A. Jost, B. Fauqué, J. van Dijk, M. J. Meijer, T. Khouri, S. Pezzini, S. Grauer, S. Schreyeck, C. Brüne, H. Buhmann, L. W. Molenkamp, and N. E. Hussey. Anisotropic and strong negative magnetoresistance in the three-dimensional topological insulator Bi_2Se_3. *Phys. Rev. B*, 94(8):081302, (2016).

[126] A. G. Moghaddam, A. Qaiumzadeh, A. Dyrdał, and J. Berakdar. Highly tunable spin-orbit torque and anisotropic magnetoresistance in a topological insulator thin film attached to ferromagnetic fayer. *Phys. Rev. Lett.*, 125(19):196801, (2020).

[127] A. Yamada and Y. Fuseya. Angular dependence of magnetoresistance and planar Hall effect in semimetals in strong magnetic fields. *Phys. Rev. B*, 103(12):125148, (2021).

[128] J. Sklenar, Y. Zhang, M. B. Jungfleisch, Y. Kim, Y. Xiao, G. J. MacDougall, M. J. Gilbert, A. Hoffmann, P. Schiffer, and N. Mason. Proximity-induced anisotropic magnetoresistance in magnetized topological insulators. *Appl. Phys. Lett.*, 118(23), (2021).

[129] A. N. Zarezad and J. Abouie. Transport in magnetically doped topological insulators: Effects of magnetic clusters. *Phys. Rev. B*, 98(15):155413, (2018).

[130] A. Ahmad and G. Sharma. Longitudinal magnetoconductance and the planar Hall effect in a lattice model of tilted Weyl fermions. *Phys. Rev. B*, 103(11):115146, (2021).

[131] P. Wang, T. Hou, F. Tang, P. Wang, Y. Han, Y. Ren, H. Zeng, L. Zhang, and Z. Qiao. Temperature dependent in-plane anisotropic magnetoresistance in $HfTe_5$ thin layers. *Chin. Phys. Lett.*, 38(1):17201, (2021).

[132] X. C. Yang, X. Luo, J. J. Gao, Z. Z. Jiang, W. Wang, T. Y. Wang, J. G. Si, C. Y. Xi, W. H. Song, and Y. P. Sun. Planar Hall effect in the quasi-one-dimensional topological superconductor $TaSe_3$. *Phys. Rev. B*, 104(15):155106, (2021).

[133] W. Rao, Y.-L. Zhou, Y. Wu, H.-J. Duan, M.-X. Deng, and R.-Q. Wang. Theory for linear and nonlinear planar Hall effect in topological insulator thin films. *Phys. Rev. B*, 103(15):155415, (2021).

[134] A. Sulaev, M. Zeng, S.-Q. Shen, S. K. Cho, W. G. Zhu, Y. P. Feng, S. V. Eremeev, Y. Kawazoe, L. Shen, and L. Wang. Electrically tunable in-plane anisotropic magnetoresistance in topological insulator $BiSbTeSe_2$ Nanodevices. *Nano Lett.*, 15(3):2061–2066, (2015).

[135] A. Kandala, A. Richardella, S. Kempinger, C.-X. Liu, and N. Samarth. Giant anisotropic magnetoresistance in a quantum anomalous Hall insulator. *Nat. Commun.*, 6(7434):1–6, (2015).

[136] J. Strunz, J. Wiedenmann, C. Fleckenstein, L. Lunczer, W. Beugeling, V. L. Müller, P. Shekhar, N. T. Ziani, S. Shamim, J. Kleinlein, H. Buhmann, B. Trauzettel, and L. W. Molenkamp. Interacting topological edge channels. *Nat. Phys.*, 16(1):83–88, (2020).

[137] J. Yang, W. L. Zhen, D. D. Liang, Y. J. Wang, X. Yan, S. R. Weng, J. R. Wang, W. Tong, L. Pi, W. K. Zhu, and C. J. Zhang. Current jetting distorted planar Hall effect in a Weyl semimetal with ultrahigh mobility. *Phys. Rev. Mater.*, 3(1):014201, (2019).

[138] K. Kang, S. Jiang, H. Berger, K. Watanabe, T. Taniguchi, L. Forró, J. Shan, and K. F Mak. Giant anisotropic magnetoresistance in Ising superconductor-magnetic insulator tunnel junctions. *arXiv*, (2021).

[139] J. Liu, L. J. Cornelissen, J. Shan, T. Kuschel, and B. J. van Wees. Magnon planar Hall effect and anisotropic magnetoresistance in a magnetic insulator. *Phys. Rev. B*, 95(14):140402, (2017).

[140] C. Safranski, E. A. Montoya, and I. N. Krivorotov. Spin-orbit torque driven by a planar Hall current. *Nat. Nanotechnol.*, 14(1):27–30, (2019).

[141] M.-W. Lu, L.-D. Zhang, and X.-H. Yan. Spin polarization of electrons tunneling through magnetic-barrier nanostructures. *Phys. Rev. B*, 66(22):224412, (2002).

[142] T. Jungwirth, J. Wunderlich, and K. Olejník. Spin Hall effect devices. *Nat. Mater.*, 11(5):382–390, (2012).

[143] J.-C. Rojas-Sánchez, S. Oyarzún, Y. Fu, A. Marty, C. Vergnaud, S. Gambarelli, L. Vila, M. Jamet, Y. Ohtsubo, A. Taleb-Ibrahimi, P. Le Fèvre, F. Bertran, N. Reyren, J.-M. George, and A. Fert. Spin to charge conversion at room temperature by spin pumping into a new type of topological insulator: α-Sn films. *Phys. Rev. Lett.*, 116(9):096602, (2016).

[144] H. Itoh and J. Inoue. Theory of tunnel magnetoresistance. *J. Magn. Soc. Jpn.*, 30(1):1–37, (2006).

[145] E. Dagotto. *Nanoscale phase separation and colossal magnetoresistance*. Springer, (2003).

[146] M. N. Baibich, J. M. Broto, A. Fert, F. Nguyen Van Dau, F. Petroff, P. Etienne, G. Creuzet, A. Friederich, and J. Chazelas. Giant magnetoresistance of (001)Fe/(001)Cr magnetic superlattices. *Phys. Rev. Lett.*, 61(21):2472–2475, (1988).

[147] G. Binasch, P. Grünberg, F. Saurenbach, and W. Zinn. Enhanced magnetoresistance in layered magnetic structures with antiferromagnetic interlayer exchange. *Phys. Rev. B*, 39(7):4828–4830(R), (1989).

[148] L. Šmejkal, A. B. Hellenes, R. González-Hernández, J. Sinova, and T. Jungwirth. Giant and tunneling magnetoresistance in unconventional collinear antiferromagnets with nonrelativistic spin-momentum coupling. *Phys. Rev. X*, 12(1):011028, (2022).

[149] J. Zhang, M. Moldovan, D. P. Young, and E. J. Podlaha. Electrochemical inspection of electrodeposited giant magnetoresistance CoNiCu/Cu multilayer films. *J. Electrochem. Soc.*, 152(9):C626, (2005).

[150] D. M. Davis, M. Moldovan, D. P. Young, M. Henk, X. Xie, and E. J. Podlaha. Magnetoresistance in electrodeposited CoNiFe/Cu multilayered nanotubes. *Electrochem. Solid-State Lett.*, 9(9):C153, (2006).

[151] D. Davis, M. Zamanpour, M. Moldovan, D. Young, and E. J. Podlaha. Electrodeposited, GMR CoNiFeCu nanowires and nanotubes from electrolytes maintained at different temperatures. *J. Electrochem. Soc.*, 157(6):D317, (2010).

[152] Z. Guo, H. T. Hahn, H. Lin, A. B. Karki, and D. P. Young. Magnetic and magnetoresistance behaviors of particulate iron/vinyl ester resin nanocomposites. *J. Appl. Phys.*, 104(1), (2008).

[153] D. Zhang, R. Chung, A. B. Karki, F. Li, D. P. Young, and Z. Guo. Magnetic and magnetoresistance behaviors of solvent extracted particulate iron/polyacrylonitrile nanocomposites. *J. Phys. Chem. C*, 114(1):212–219, (2010).

[154] Q. H. Huo, R. Z. Wang, and H. Yan. Giant magnetoresistance effect in graphene with asymmetrical magnetic superlattices. *Appl. Phys. Lett.*, 101(15), (2012).

[155] K. Gopinadhan, Y. J. Shin, I. Yudhistira, J. Niu, and H. Yang. Giant magnetoresistance in single-layer graphene flakes with a gate-voltage-tunable weak antilocalization. *Phys. Rev. B*, 88(19):195429, (2013).

[156] Y. Sheng, T. D. Nguyen, G. Veeraraghavan, Ö. Mermer, and M. Wohlgenannt. Effect of spin-orbit coupling on magnetoresistance in organic semiconductors. *Phys. Rev. B*, 75(3):035202, (2007).

[157] H. Fukuzawa, H. Yuasa, S. Hashimoto, H. Iwasaki, and Y. Tanaka. Large magnetoresistance ratio of 10% by $Fe_{50}Co_{50}$ layers for current-confined-path current-perpendicular-to-plane giant magnetoresistance spin-valve films. *Appl. Phys. Lett.*, 87(8), (2005).

[158] I. Ennen, D. Kappe, T. Rempel, C. Glenske, and A. Hütten. Giant magnetoresistance: Basic concepts, microstructure, magnetic interactions and applications. *Sensors*, 16(6), (2016).

[159] C. Reig, S. Cardoso, and S. C. Mukhopadhyay. *Giant magnetoresistance (GMR) sensors*. Springer, (2013).

[160] D. Karnaushenko, D. Makarov, C. Yan, R. Streubel, and O. G. Schmidt. Printable giant magnetoresistive devices. *Adv. Mater.*, 24(33):4518–4522, (2012).

[161] M. Pannetier-Lecoeur, L. Parkkonen, N. Sergeeva-Chollet, H. Polovy, C. Fermon, and C. Fowley. Magnetocardiography with sensors based on giant magnetoresistance. *Appl. Phys. Lett.*, 98(15), (2011).

[162] B. Eickenberg, J. Meyer, L. Helmich, D. Kappe, A. Auge, A. Weddemann, F. Wittbracht, and A. Hütten. Lab-on-a-chip magneto-immunoassays: How to ensure contact between superparamagnetic beads and the sensor surface. *Biosensors*, 3(3):327–340, (2013).

[163] C. Chappert, A. Fert, and F. N. Van Dau. The emergence of spin electronics in data storage. *Nat. Mater.*, 6(11):813–823, (2007).

[164] F. Muñoz-Rojas, J. Fernández-Rossier, and J. J. Palacios. Giant magnetoresistance in ultrasmall graphene based devices. *Phys. Rev. Lett.*, 102(13):136810, (2009).

[165] Y.-T. Zhang, H. Jiang, Q. Sun, and X. C. Xie. Spin polarization and giant magnetoresistance effect induced by magnetization in zigzag graphene nanoribbons. *Phys. Rev. B*, 81(16):165404, (2010).

[166] S. Manipatruni, D. E. Nikonov, C.-C. Lin, T. A. Gosavi, H. Liu, B. Prasad, Y.-L. Huang, E. Bonturim, R. Ramesh, and I. A. Young. Scalable energy-efficient magnetoelectric spin-orbit logic. *Nature*, 565(7737):35–42, (2019).

[167] H. A. Ferreira, D. L. Graham, P. P. Freitas, and J. M. S. Cabral. Biodetection using magnetically labeled biomolecules and arrays of spin valve sensors (invited). *J. Appl. Phys.*, 93(10):7281–7286, (2003).

[168] C. Heiliger, P. Zahn, and I. Mertig. Microscopic origin of magnetoresistance. *Mater. Today*, 9(11):46–54, (2006).

[169] M. Julliere. Tunneling between ferromagnetic films. *Phys. Lett. A*, 54(3):225–226, (1975).

[170] S. S. P. Parkin, C. Kaiser, A. Panchula, P. M. Rice, B. Hughes, M. Samant, and S.-H. Yang. Giant tunnelling magnetoresistance at room temperature with MgO (100) tunnel barriers. *Nat. Mater.*, 3(12):862–867, (2004).

[171] M. Bowen, V. Cros, F. Petroff, A. Fert, C. Martı'nez Boubeta, J. L. Costa-Krämer, J. V. Anguita, A. Cebollada, F. Briones, J. M. de Teresa, L. Morellón, M. R. Ibarra, F. Güell, F. Peiró, and A. Cornet. Large magnetoresistance in Fe/MgO/FeCo(001) epitaxial tunnel junctions on GaAs(001). *Appl. Phys. Lett.*, 79(11):1655–1657, (2001).

[172] H. Mehrez, Jeremy Taylor, Hong Guo, Jian Wang, and Christopher Roland. Carbon nanotube based magnetic tunnel junctions. *Phys. Rev. Lett.*, 84(12):2682–2685, (2000).

[173] T. S. Santos, J. S. Lee, P. Migdal, I. C. Lekshmi, B. Satpati, and J. S. Moodera. Room-temperature tunnel magnetoresistance and spin-polarized tunneling through an organic semiconductor barrier. *Phys. Rev. Lett.*, 98(1):016601, (2007).

[174] S. Ikeda, K. Miura, H. Yamamoto, K. Mizunuma, H. D. Gan, M. Endo, S. Kanai, J. Hayakawa, F. Matsukura, and H. Ohno. A perpendicular-anisotropy CoFeB-MgO magnetic tunnel junction. *Nat. Mater.*, 9(9):721–724, (2010).

[175] Y. Zhang and F. Zhai. Tunneling magnetoresistance on the surface of a topological insulator with periodic magnetic modulations. *Appl. Phys. Lett.*, 96(17), (2010).

[176] M. Götte, To. Paananen, G. Reiss, and T. Dahm. Tunneling magnetoresistance devices based on topological insulators: Ferromagnet–insulator–topological-insulator junctions employing Bi_2Se_3. *Phys. Rev. Appl.*, 2(5):054010, (2014).

[177] R. Vali and M. Vali. Tunneling conductance and magnetoresistance in topological insulator Fi/I/Fi/d-wave superconductor junctions. *J. Appl. Phys.*, 112(10), (2012).

[178] S. Meena and S. Choudhary. Tuning the tunneling magnetoresistance by using fluorinated graphene in graphene based magnetic junctions. *AIP Adv.*, 7(12), (2017).

[179] W. Qiu, J. Peng, M. Pan, Y. Hu, Mi. Ji, J. Hu, W. Tian, D. Chen, Q. Zhang, and P. Li. Spin-dependent resonant tunneling and magnetoresistance in Ni/graphene/h-BN/graphene/Ni van der Waals heterostructures. *J. Magn. Magn. Mater.*, 476:622–627, (2019).

[180] K. Garello, F. Yasin, and G. S. Kar. Spin-orbit torque MRAM for ultrafast embedded memories: from fundamentals to large scale technology integration. In *2019 IEEE 11th International Memory Workshop (IMW)*, pages 12–15. IEEE, (2019).

[181] D. C. Worledge. Spin-transfer-torque MRAM: The next revolution in memory. In *2022 IEEE International Memory Workshop (IMW)*, pages 15–18. IEEE, (2022).

[182] H. Wu, A. Chen, P. Zhang, H. He, J. Nance, C. Guo, J. Sasaki, T. Shirokura, P. N. Hai, B. Fang, S. A. Razavi, K. Wong, Y. Wen, Y. Ma, G. Yu, G. P. Carman, X. Han, X. Zhang, and K. L. Wang. Magnetic memory driven by topological insulators. *Nat. Commun.*, 12(6251):1–7, (2021).

[183] T. Nakano, M. Oogane, T. Furuichi, and Y. Ando. Magnetic tunnel junctions using perpendicularly magnetized synthetic antiferromagnetic reference layer for wide-dynamic-range magnetic sensors. *Appl. Phys. Lett.*, 110(1), (2017).

[184] S. Yan, Z. Zhou, Y. Yang, Q. Leng, and W. Zhao. Developments and applications of tunneling magnetoresistance sensors. *Tsinghua Sci. Technol.*, 27(3):443–454, (2021).

[185] E. E. Fullerton and J. R. Childress. Spintronics, magnetoresistive heads, and the emergence of the digital world. *Proc. IEEE*, 104(10):1787–1795, (2016).

[186] R. Bläsing, A. A. Khan, P. Ch. Filippou, C. Garg, F. Hameed, J. Castrillon, and S. S. P. Parkin. Magnetic racetrack memory: from physics to the cusp of applications within a decade. *Proc. IEEE*, 108(8):1303–1321, (2020).

[187] Y. Yao, H. Cheng, B. Zhang, J. Yin, D. Zhu, W. Cai, S. Li, and W. Zhao. Tunneling magnetoresistance materials and devices for neuromorphic computing. *Mater. Futures*, 2(3):032302, (2023).

[188] E. Dagotto, T. Hotta, and A. Moreo. Colossal magnetoresistance materials: the key role of phase separation. *Phys. Rep.*, 344(1):1–153, (2001).

[189] A. P. Ramirez. Colossal magnetoresistance. *J. Phys.: Condens. Matter*, 9(39):8171, (1997).

[190] N. Shirato. Colossal Magnetoresistance. PhySH, (2010).

[191] R. Singha, K. J. Dalgaard, D. Marchenko, M. Krivenkov, E. D. L. Rienks, M. Jovanovic, S. M. L. Teicher, J. Hu, T. H. Salters, J. Lin, A. Varykhalov, N. P. Ong, and L. M. Schoop. Colossal magnetoresistance in the multiple wave vector charge density wave regime of an antiferromagnetic Dirac semimetal. *Sci. Adv.*, 9(41), (2023).

[192] M. Baldini, T. Muramatsu, M. Sherafati, H. Mao, L. Malavasi, P. Postorino, S. Satpathy, and V. V. Struzhkin. Origin of colossal magnetoresistance in $LaMnO_3$ manganite. *Proc. Natl. Acad. Sci. U.S.A.*, 112(35):10869–10872, (2015).

[193] S. Jin, T. H. Tiefel, M. McCormack, R. A. Fastnacht, R. Ramesh, and L. H. Chen. Thousandfold change in resistivity in magnetoresistive La-Ca-Mn-O films. *Science*, 264(5157):413–415, (1994).

[194] E. J. Wildman, J. M. S. Skakle, N. Emery, and A. C. Mclaughlin. Colossal magnetoresistance in Mn^{2+} oxypnictides $NdMnAsO_{1-x}F_x$. *J. Am. Chem. Soc.*, 134(21):8766–8769, (2012).

[195] C. Christides. Magnetotransport properties of ultrathin metallic multilayers: microstructural modifications leading to sensor applications. In *Handbook of Surfaces and Interfaces of Materials*, volume 4, pages 65–130. Academic Press, (2001).

[196] M. Weiler, M. Althammer, F. D. Czeschka, H. Huebl, M. S. Wagner, M. Opel, I.-M. Imort, G. Reiss, A. Thomas, R. Gross, and S. T. B. Goennenwein. Local charge and spin currents in magnetothermal landscapes. *Phys. Rev. Lett.*, 108(10):106602, (2012).

[197] Y.-Ti. Chen, S. Takahashi, H. Nakayama, M. Althammer, S. T. B. Goennenwein, E. Saitoh, and G. E. W. Bauer. Theory of spin Hall magnetoresistance. *Phys. Rev. B*, 87(14):144411, (2013).

[198] H. Nakayama, M. Althammer, Y.-T. Chen, K. Uchida, Y. Kajiwara, D. Kikuchi, T. Ohtani, S. Geprägs, M. Opel, S. Takahashi, R. Gross, G. E. W. Bauer, S. T. B. Goennenwein, and E. Saitoh. Spin Hall magnetoresistance induced by a nonequilibrium proximity effect. *Phys. Rev. Lett.*, 110(20):206601, (2013).

[199] S. D. Ganichev, E. L. Ivchenko, S. N. Danilov, J. Eroms, W. Wegscheider, D. Weiss, and W. Prettl. Conversion of spin into directed electric current in quantum wells. *Phys. Rev. Lett.*, 86(19):4358–4361, (2001).

[200] N. H. Duy Khang and P. N. Hai. Giant unidirectional spin Hall magnetoresistance in topological insulator-ferromagnetic semiconductor heterostructures. *J. Appl. Phys.*, 126(23), (2019).

[201] Y.-T. Chen, S. Takahashi, H. Nakayama, M. Althammer, S. T. B. Goennenwein, E. Saitoh, and G. E. W. Bauer. Theory of spin Hall magnetoresistance (SMR) and related phenomena. *J. Phys.: Condens. Matter*, 28(10):103004, (2016).

[202] Yu. V. Pershin, N. A. Sinitsyn, A. Kogan, A. Saxena, and D. L. Smith. Spin polarization control by electric stirring: Proposal for a spintronic device. *Appl. Phys. Lett.*, 95(2), (2009).

[203] Y. Hui, H. Jiang, F. Xie, W. Lin, C. Dong, K. Dong, Q. He, and X. Miao. Maximizing spin Hall magnetoresistance in heavy metal/crystalline metallic ferromagnet multilayers with opposite spin Hall angles. *Nanoscale*, 15(2):820–827, (2023).

[204] S. S.-L. Zhang and G. Vignale. Theory of bilinear magneto-electric resistance from topological-insulator surface states. In *Proceedings, Spintronics XI*, volume 10732, pages 97–107. SPIE, (2018).

[205] T. Ideue, K. Hamamoto, S. Koshikawa, M. Ezawa, S. Shimizu, Y. Kaneko, Y. Tokura, N. Nagaosa, and Y. Iwasa. Bulk rectification effect in a polar semiconductor. *Nat. Phys.*, 13(6):578–583, (2017).

[206] Y. Fu, J. Li, J. Papin, P. Noël, S. Teresi, M. Cosset-Chéneau, C. Grezes, T. Guillet, C. Thomas, Y.-M. Niquet, P. Ballet, T. Meunier, J.-P. Attané, A. Fert, and L. Vila. Bilinear magnetoresistance in HgTe topological insulator: Opposite signs at opposite surfaces demonstrated by gate control. *Nano Lett.*, 22(19):7867–7873, (2022).

[207] Y. Wang, S. V. Mambakkam, Y.-X. Huang, Y. Wang, Y. Ji, C. Xiao, S. A. Yang, S. A. Law, and J. Q. Xiao. Observation of nonlinear planar Hall effect in magnetic-insulator–topological-insulator heterostructures. *Phys. Rev. B*, 106(15):155408, (2022).

[208] Q. H. Wang, K. Kalantar-Zadeh, A. Kis, J. N. Coleman, and M. S. Strano. Electronics and optoelectronics of two-dimensional transition metal dichalcogenides. *Nat. Nanotechnol.*, 7(11):699–712, (2012).

[209] T. Liu, A. Roy, J. Hidding, H. Jafari, D. K. de Wal, J. Sławińska, M. H. D. Guimarães, and B. J. van Wees. Crystallographically dependent bilinear magnetoelectric resistance in a thin WTe_2 layer. *Phys. Rev. B*, 108(16):165407, (2023).

[210] D. C. Vaz, F. Trier, A. Dyrdał, A. Johansson, K. Garcia, A. Barthélémy, I. Mertig, J. Barnaś, A. Fert, and M. Bibes. Determining the Rashba parameter from the bilinear magnetoresistance response in a two-dimensional electron gas. *Phys. Rev. Mater.*, 4:071001, (2020).

[211] Pan He, S. McKeown Walker, Steven S.-L. Zhang, F. Y. Bruno, M. S. Bahramy, Jong Min Lee, Rajagopalan Ramaswamy, Kaiming Cai, Olle Heinonen, Giovanni Vignale, F. Baumberger, and Hyunsoo Yang. Observation of Out-of-Plane Spin Texture in a $\mathrm{SrTiO_3(111)}$ Two-Dimensional Electron Gas. *Phys. Rev. Lett.*, 120(26):266802, (2018).

[212] J. Lindemuth. *Hall effect measurement handbook: A fundamental tool for semiconductor material characterization*. Lake Shore Cryotronics, Incorporated, (2020).

[213] A. Elzwawy, H. Pişkin, N. Akdoğan, M. Volmer, G. Reiss, L. Marnitz, A. Moskaltsova, O. Gurel, and J.-M. Schmalhorst. Current trends in planar Hall effect sensors: evolution, optimization, and applications. *J. Phys. D: Appl. Phys.*, 54(35):353002, (2021).

[214] C. Goldberg and R. E. Davis. New galvanomagnetic effect. *Phys. Rev.*, 94(5):1121–1125, (1954).

[215] L. Li, E. Yi, B. Wang, G. Yu, B. Shen, Z. Yan, and M. Wang. Higher-order oscillatory planar Hall effect in topological kagome metal. *npj Quantum Mater.*, 8(2):1–7, (2023).

[216] M. Wu, D. Tu, Y. Nie, S. Miao, W. Gao, Y. Han, X. Zhu, J. Zhou, W. Ning, and M. Tian. Novel π/2-Periodic planar Hall effect due to orbital magnetic moments in $MnBi_2Te_4$. *Nano Lett.*, 22(1):73–80, (2022).

[217] A. O. Adeyeye, M. T. Win, T. A. Tan, G. S. Chong, V. Ng, and T. S. Low. Planar Hall effect and magnetoresistance in Co/Cu multilayer films. *Sens. Actuators, A*, 116(1):95–102, (2004).

[218] A. Soori. Finite transverse conductance and anisotropic magnetoconductance under an applied in-plane magnetic field in two-dimensional electron gases with strong spin-orbit coupling. *J. Phys.: Condens. Matter*, 33(33):335303, (2021).

[219] Y.-X. Huang, X. Feng, H. Wang, C. Xiao, and S. A. Yang. Intrinsic nonlinear planar Hall effect. *Phys. Rev. Lett.*, 130(12):126303, (2023).

[220] M. Bowen, K.-J. Friedland, J. Herfort, H.-P. Schönherr, and K. H. Ploog. Order-driven contribution to the planar Hall effect in Fe_3Si thin films. *Phys. Rev. B*, 71(17):172401, (2005).

[221] K. M. Seemann, F. Freimuth, H. Zhang, S. Blügel, Y. Mokrousov, D. E. Bürgler, and C. M. Schneider. Origin of the planar Hall effect in nanocrystalline $Co_{60}Fe_{20}B_{20}$. *Phys. Rev. Lett.*, 107(8):086603, (2011).

[222] C. R. Akouala, R. Kumar, S. Punugupati, C. L. Reynolds, J. G. Reynolds, E. J. Mily, J.-P. Maria, J. Narayan, and F. Hunte. Planar Hall effect and anisotropic magnetoresistance in semiconducting and conducting oxide thin films. *Appl. Phys. A*, 125(5):293–12, (2019).

[223] A. A. Burkov. Giant planar Hall effect in topological metals. *Phys. Rev. B*, 96(4):041110, (2017).

[224] P. Li, C. H. Zhang, J. W. Zhang, Y. Wen, and X. X. Zhang. Giant planar Hall effect in the Dirac semimetal $ZrTe_{5-\delta}$. *Phys. Rev. B*, 98(12):121108, (2018).

[225] R. Singha, S. Roy, A. Pariari, B. Satpati, and P Mandal. Planar Hall effect in the type-II Dirac semimetal VAl_3. *Phys. Rev. B*, 98(8):081103, (2018).

[226] N. Kumar, S. N. Guin, C. Felser, and C. Shekhar. Planar Hall effect in the Weyl semimetal GdPtBi. *Phys. Rev. B*, 98(4):041103, (2018).

[227] M.-X. Deng, H.-J. Duan, W. Luo, W. Y. Deng, R.-Q. Wang, and L. Sheng. Quantum oscillation modulated angular dependence of the positive longitudinal magnetoconductivity and planar Hall effect in Weyl semimetals. *Phys. Rev. B*, 99(16):165146, (2019).

[228] S.-H. Zheng, H.-J. Duan, J.-K. Wang, J.-Y. Li, M.-X. Deng, and R.-Q. Wang. Origin of planar Hall effect on the surface of topological insulators: Tilt of Dirac cone by an in-plane magnetic field. *Phys. Rev. B*, 101(4):041408, (2020).

[229] B. Scharf, A. Matos-Abiague, J. E. Han, E. M. Hankiewicz, and I. Žutić. Tunneling planar Hall effect in topological insulators: Spin valves and amplifiers. *Phys. Rev. Lett.*, 117(16):166806, (2016).

[230] D. Suri and A. Soori. Finite transverse conductance in topological insulators under an applied in-plane magnetic field. *J. Phys.: Condens. Matter*, 33(33):335301, (2021).

[231] A. Ghasemi. Ferrite synthesis methods. In *Magnetic ferrites and related nanocomposites*, pages 587–625. Elsevier, Walthm, MA, USA, (2022).

[232] G. Pacchioni. The Hall effect goes nonlinear. *Nat. Rev. Mater.*, 4(8):514, August (2019).

[233] Y. Lv, J. Kally, D. Zhang, J. Sue Lee, M. Jamali, N. Samarth, and J.-P. Wang. Unidirectional spin-Hall and Rashba-Edelstein magnetoresistance in topological insulator-ferromagnet layer heterostructures. *Nat. Commun.*, 9(111):1–7, (2018).

[234] K. Yasuda, A. Tsukazaki, R. Yoshimi, K. Kondou, K. S. Takahashi, Y. Otani, M. Kawasaki, and Y. Tokura. Current-nonlinear Hall effect and spin-orbit torque magnetization switching in a magnetic topological insulator. *Phys. Rev. Lett.*, 119(13):137204, (2017).

[235] V. D. Esin, A. V. Timonina, N. N. Kolesnikov, and E. V. Deviatov. Nonlinear planar Hall effect in chiral topological semimetal CoSi. *J. Exp. Theor. Phys.*, 133(6):792–797, (2021).

[236] S. Nandy, A. Taraphder, and S. Tewari. Berry phase theory of planar Hall effect in topological insulators. *Sci. Rep.*, 8(14983):1–9, (2018).

[237] R. A. Jishi. *Feynman Diagram Techniques in Condensed Matter Physics*. Cambridge University Press, Cambridge, England, UK, (2013).

[238] A. A. Abrikosov, L. P. Gorkov, and I. E. Dzyaloshinski. *Methods of Quantum Field Theory in Statistical Physics*. Courier Corporation, (1963).

[239] H. Bruus and K. Flensberg. *Many-Body Quantum Theory in Condensed Matter Physics*. Oxford University Press, (2004).

[240] G. D. Mahan. *Many-Particle Physics, third ed.* Springer US, (2000).

[241] S. Doniach and E. H. Sondheimer. *Green's functions for solid state physicists*. W. A. Benjamin, (1974).

[242] K. Boboshko, A. Dyrdał, and J. Barnaś. Bilinear magnetoresistance in topological insulators: The role of spin-orbit scattering on impurities. *J. Magn. Magn. Mater.*, 545:168698, (2022).

[243] K. Boboshko and A. Dyrdał. Bilinear magnetoresistance and planar Hall effect in topological insulators: Interplay of scattering on spin-orbital impurities and nonequilibrium spin polarization. *Phys. Rev. B*, 109(15):155420, (2024).

[244] R. Peierls. On the theory of diagmanetism of conduction electrons. *Z. Phys.*, 80(11):763–791, (1933).

[245] R. Y. Díaz-Bonifaz and C. Ramírez. Dots and boxes algorithm for Peierls substitution: Application to multidomain topological insulator. *ArXiv*, (2024).

[246] J. Wu and C. M. Wang. Anisotropic magnetotransport in tilted magnetic topological semimetals. *J. Phys.: Condens. Matter*, 33(16):165701, (2021).

[247] D. E. Parker, T. Morimoto, J. Orenstein, and J. E. Moore. Diagrammatic approach to nonlinear optical response with application to Weyl semimetals. *Phys. Rev. B*, 99(4):045121, (2019).

[248] Z. Z. Du, H.-Z. Lu, and X. C. Xie. Nonlinear Hall effects. *Nat. Rev. Phys.*, 3(11):744–752, (2021).

[249] D. Ma, A. Arora, G. Vignale, and J. C. W. Song. Anomalous skew-scattering nonlinear Hall effect and chiral photocurrents in $\mathcal{PT}$-symmetric antiferromagnets. *Phys. Rev. Lett.*, 131(7):076601, (2023).